

FIELD SCALE PERMEABILITY ESTIMATION BASED ON MICROSEISMIC MONITORING

A Dissertation

Presented to

the Faculty of the Department of Earth and Atmospheric Sciences

University of Houston

In Partial Fulfillment

of the Requirements for the Degree

Doctor of Philosophy

By

Xin Zhang

August 2015

FIELD SCALE PERMEABILITY ESTIMATION BASED ON MICROSEISMIC MONITORING

Xin Zhang

APPROVED:

Dr. Evgeny Chesnokov, Committee Chair
Department of Earth and Atmospheric Sciences

Dr. John Castagna, Committee member
Department of Earth and Atmospheric Sciences

Dr. Gennady Goloshubin, Committee member
Department of Earth and Atmospheric Sciences

Dr. Xin-gong Li, Committee member
Shell Global Solutions

Dean
College of Natural Sciences and Mathematics

Acknowledgements

This dissertation is the result of my studies and research work at the University of Houston. I want to extend thanks for mentoring to Dr. Evgeny Chesnokov, Dr. John Castagna, Dr. Gennady Goloshubin, and Dr. Xin-gong Li. I extend gratitude to Dr. Evgeny Chesnokov for his guidance, encouragement, and for creating a friendly and dynamic research group environment. I am also grateful to Dr. John Castagna and Dr. Gennady Goloshubin for their helpful suggestions. Thanks to Dr. Xin-gong Li for the fruitful discussions on this topic and for his helpful contributions as a member of my committee. I am grateful to my parents for raising me. Also special thanks to Dr. Donald Kouri, Zhao Li, Jie Yao, Xiaoxiang Wang, and all the other members in our research group. It would have been a long and painful road without their help.

FIELD SCALE PERMEABILITY ESTIMATION BASED ON MICROSEISMIC MONITORING

An Abstract of a Dissertation

Presented to

the Faculty of the Department of Earth and Atmospheric Sciences

University of Houston

In Partial Fulfillment

of the Requirements for the Degree of

Doctor of Philosophy

By

Xin Zhang

August 2015

Abstract

The 3-dimension diffusion equation which describes fluid flow during hydraulic fracturing is interpreted in a statistical way. For all diffusing particles in a pumping procedure, the root-mean-square average of diffusing distance, which evaluates the fluctuation of diffusing particles as time evolves, is proportional to the square root of the product of diffusivity and elapsed time. The diffusivity is obtained from the spatial-temporal distribution of located microseismic events as a function of the distance between these events and pumping points, as well as elapsed time from injection inception. The upper-limit diffusivity of the original formation is characterized by the curve which fits the outermost located events on a distance-time plot. Similarly, diffusivity of the formation after hydraulic fracturing is obtained by curve fitting innermost located events induced by fluid flow back after injection stops.

The theoretical expression between the diffusivity tensor and permeability tensor is obtained based on an isothermal condition and assumed incompressible slurry. The diffusivity tensor is found to be equal to the permeability tensor divided by a scalar which is the product of dynamic viscosity, connected formation porosity, and formation compressibility.

Application of these equations to microseismic data acquired in the Barnett Shale Formation yields, with assumed hydraulic fracture geometry, initial permeability of 0.16 to 3.21 milliDarcy in the assumed dominant direction of

fracturing and normal to it, with an increase to 12.1 milliDarcy along the dominant direction of fracturing after hydraulic fracturing.

Numerical simulation results of fluid flow in synthetic media demonstrate:

- (1) If the flow domain size is not much larger than the part influenced by the entrance effect, the variables in Darcy's law are inter-dependent. If so, the obtained permeability, no matter by experiment or simulation, cannot be upscaled, even under homogeneous condition.
- (2) The volume or area influenced by the entrance effect inside the flow domain depends on the geometry of the flow domain, fluid properties, and in-situ parameters. The more viscous fluid flow in a lower rate, the smaller volume or area influenced by entrance effect.
- (3) The flow field is difficult to be fully developed in a periodic domain. The wide throat zones store fluid as reservoirs.

Contents

Acknowledgements.....	iii
Abstract	v
List of Figures	viii
Chapter 1 Introduction.....	1
1.1 Permeability and Darcy’s law.....	2
1.2 Hydraulic fracturing and shale reservoirs.....	4
1.3 Literature review	8
1.4 Methods.....	11
1.5 Dissertation layout.....	13
Chapter 2 Diffusion method	14
2.1 Introduction	14
2.2 Interpretation of diffusion procedure.....	16
2.3 Diffusivity and permeability	19
2.4 Overview of microseismic monitoring.....	21
2.4.1 Microseismic event location.....	22
2.4.2 Moment tensor and seismic magnitude analysis	28
2.5 A case study.....	31
2.5.1 Dollie data acquisition and processing	33
2.5.2 Dollie data interpretation.....	40
2.6 Summary and discussion.....	50
2.6.1 Summary	50
2.6.2 Discussion	51
Chapter 3 Fluid flow simulation.....	58
3.1 Introduction	58
3.2 Numerical methods and the Navier-Stokes equation	59
3.3 Finite difference method and flow simulation in simple geometry domain	62
3.3.1 Finite difference method	62
3.3.2 Flow simulation in simple geometry domain	63
3.4 Finite element method and flow simulation in the periodic domain	75
3.5 Fluid flow simulation in synthetic media	81
3.5.1 Angular dependent permeability of shale sample.....	81
3.5.2 Scale dependent effect.....	89
3.6 Conclusion and discussion	97
Chapter 4 Conclusions and future work	100
4.1 Conclusions	100
4.2 Recommendation for future work	101
Appendix.....	103
References.....	106

List of Figures

Figure 1-1 Hydraulic fracturing. The yellow-color dendritic structures along the horizontal interval of injection well represent fractures induced by pumping.	5
Figure 1-2 Identified shale gas plays in continental United States. (Theresa Andrejack Loux and Archie Filshill, 2013).....	6
Figure 1-3 Three cylinder samples from one Barnett Shale core, along 0, 45, and 90 degrees to the bedding plane. The left picture is the illustration modified from Wang, 2002. The right picture is the phot of one set of our samples (core-B;AS6485).	7
Figure 2-1 The property is transported from high concentration to low concentration. The transported property could be mass, momentum, or energy and is represented by the red dots	15
Figure 2-2 A diffusion procedure at different time: (a) distribution of particles at t_1 and (b) distribution of particles at $t_1 + \Delta t$	18
Figure 2-3 Moment magnitude, moment of microseismic, and equivalent explosive charge (Evgeny Chesnokov, “Microseismics: Integrated, Advanced Geophysics”, class lecture, Microseismic, Natural Sciences and Mathematics, Houston, TX, Aug 27, 2012).	23
Figure 2-4 Light noise contamination and arrival-time picking results (Evgeny Chesnokov, “Microseismics: Integrated, Advanced Geophysics”, class lecture, Microseismic, Natural Sciences and Mathematics, Houston, TX, Aug 27, 2012).	23
Figure 2-5 Moderate noise contamination and arrival-time picking results (Evgeny Chesnokov, “Microseismics: Integrated, Advanced Geophysics”, class lecture, Microseismic, Natural Sciences and Mathematics, Houston, TX, Aug 27, 2012).	24
Figure 2-6 Severe noise contamination and arrival-time picking results (Evgeny Chesnokov, “Microseismics: Integrated, Advanced Geophysics”, class lecture, Microseismic, Natural Sciences and Mathematics, Houston, TX, Aug 27, 2012).	24
Figure 2-7 An example of downhole monitoring. The injection well is on the left. The monitoring well is on the right. The red rectangular points represent geophones (National Research Council, 2012).	25
Figure 2-8 Surface monitoring (National Research Council, 2012).....	25
Figure 2-9 Moment tensors and corresponding beach ball diagrams (Stein and Wysession, 2009)	29
Figure 2-10 Three types of force couples and their corresponding beach ball diagrams	30
Figure 2-11 Fort Worth Basin- Generalized stratigraphy section of the Bend Arch (Montgomery <i>et al.</i> , 2005).	33
Figure 2-12 A typical example of recorded noisy data (Osakwe, 2013)	35
Figure 2-13 Map view of event location results	36
Figure 2-14 Cross-section view of event location results.....	37
Figure 2-15 Stimulated rock volume (SRV) after hydraulic fracturing (Lambordi, 2014)	38
Figure 2-16 Increasing cumulative volume of SRV during injection (Lambordi, 2014).....	38

Figure 2-17 Number of located microseismic events in each 10-minute time interval. The red dash line represents the time of pumping stopped.....	39
Figure 2-18 Whole space r-t plot of all located events.....	41
Figure 2-19 Recorded treating parameters evolve with time. The blue line represents the treating pressure. The green line represents the cumulative slurry volume pumped in...42	
Figure 2-20 Whole space r-t plot. The red line characterizes diffusion after the fracture opening. The blue line starts at 8 hours after injection started and characterized the fluid flow back after injection stopped.	44
Figure 2-21 Map view location result of the sector with (-22.5~22.5) azimuth and (-22.5~22.5) dip.....	46
Figure 2-22 r-t plot corresponds to the same sector as in Figure 2-21	47
Figure 2-23 Map view location result of the sector which has (67.5 °~112.5 °) azimuth, and (-22.5 °~22.5 °) dip	48
Figure 2-24 r-t plot of the sector with (67.5 °~112.5 °) azimuth, and (-22.5 °~22.5 °) dip.....	49
Figure 2-25 Two perfshots taken from Dollie well. The distance between these two perfshots are 40 ft. The time difference between these two perfshots are 71 seconds. The recorded seismograms by the same station have high correlation coefficients values. (Evgeny Chesnokov, “Microseismics: Integrated, Advanced Geophysics”, class lecture, Microseismic, Natural Sciences and Mathematics, Houston, TX, Aug 27, 2012).	56
Figure 2-26 Two Perfshots taken from Dollie well. The distance between these two perfshots are 40 ft. The time difference between these two perfshots are 2 days and 23 hours. The recorded seismograms by the same station have low correlation coefficients values. (Evgeny Chesnokov, “Microseismics: Integrated, Advanced Geophysics”, class lecture, Microseismic, Natural Sciences and Mathematics, Houston, TX, Aug 27, 2012).	57
Figure 3-1 Velocity u is evaluated at points i-1, i-1, i, i+1, i+2.....	65
Figure 3-2 Points of pressure are evaluated in between the evaluated points of velocity, i.e., pressure is evaluated at the red color points.	65
Figure 3-3 Two dimensional staggered grid.....	66
Figure 3-4 Control volume and its four faces.....	67
Figure 3-5 Schematic drawing of a two-dimensional domain with four boundaries.....	69
Figure 3-6 Simulation results of Cases 1, 2, 3, and 4.....	72
Figure 3-7 Simulation results of Case A in a periodic medium with 8mm and 4mm radii throats.	78
Figure 3-8 Simulation results of Case B in a periodic domain with 4mm and 2mm radii throats.	80
Figure 3-9 Blue lines represent the shale bedding planes. Shale plugs have different angles to the bedding planes. Letters “I” and “O” mean the inlet and outlet during measurements.	82
Figure 3-10 A synthetic shale sample diagram. Blue arrow represents the flow direction....	82
Figure 3-11 Velocity and pressure field of sample with 15 °to bedding plane	84
Figure 3-12 Velocity and pressure field of sample with 30 °to bedding plane.....	85
Figure 3-13 Velocity and pressure field of sample with 45 °to bedding plane.....	86

Figure 3-14 Velocity and pressure field of sample with 60 °to bedding plane	87
Figure 3-15 Angular dependent permeability of a lab-scale synthetic shale matrix sample ...	88
Figure 3-16 A diagram of different sizes of samples with a width-constant fracture inside. ..	90
Figure 3-17 velocity field (top) and pressure field (bottom) of 1cm*1cm sample simulation	92
Figure 3-18 velocity field (top) and pressure field (bottom) of 2cm*2cm sample simulation	93
Figure 3-19 velocity field (top) and pressure field (bottom) of 4cm*4cm sample simulation	94
Figure 3-20 velocity field (top) and pressure field (bottom) of 8cm*8cm sample simulation	95
Figure 3-21 Calculated permeability results of samples with different sizes	97
Figure 4-1 The relation between the magnitude and the number of locatable microseismic events.....	101

Chapter 1 Introduction

The objective of this work is to extract field scale permeability information before and after hydraulic fracturing based on microseismic monitoring by the use of the diffusion and fluid flow simulation methods. We used the diffusion method to estimate the microseismic monitoring data called “Dollie”. Dollie data were acquired from a Barnett shale gas reservoir. The microseismic event location algorithm “UHFracDetect” was used for locating the microseismic events during monitoring. Uncertainties of the estimated permeability based on diffusion method definitely exist because of the data quality, monitoring duration, and geometry design. In order to reduce the uncertainties we implemented numerical methods and simulated fluid flow in synthetic media.

In Chapter 1, firstly, we introduce the motivation of this work, the concept of permeability, and Darcy’s law. Secondly, we briefly introduce hydraulic fracturing, shale gas, and gas shale reservoirs. Thirdly, we give literature review and analyze the limitations and problems of previous methods. Fourthly, we give the reasoning and introduce the methods used in this dissertation. These methods solved or partially solved the previous problems. Finally, we introduce the layout of this dissertation.

1.1 Permeability and Darcy's law

Permeability, as a challenging parameter, is attracting more attention from both exploration geophysicists and petroleum engineers. Permeability is closely related to production rate, which is a crucial factor in the oil and gas industry.

Permeability is highly fluctuating due to the heterogeneities in medium. Thus, it is also a scale-dependent parameter. Sample scale permeability could be measured in a laboratory; however, the results are not necessarily appropriate for upscaling. The objective of this work is to extract field scale permeability. Field scale permeability is important because it helps petroleum engineers to decide drilling sites and drilling strategies, and to build reservoir models.

The concept of permeability in fluid flow was experimentally proposed in Darcy's law (Darcy, 1856). The definition of permeability is the ease with which fluid is transmitted through a porous medium by connected pore space. Later Darcy's law was proved by derivations based on the Navier-Stokes equation. The tensor form of Darcy's law is:

$$\mathbf{u} = -\frac{\boldsymbol{\kappa}}{\eta} \nabla P, \quad (1-1)$$

where \mathbf{u} is the vector with three components which represents the specific discharge, i.e., the volume of fluid flow through unit area in unit time; $\boldsymbol{\kappa}$ is the 2nd rank tensor of permeability; scalar P is the pressure; ∇P is the pressure gradient vector; scalar η is the dynamic viscosity.

The SI unit of permeability is m^2 ; however, Darcy, milliDarcy, and microDarcy are more commonly used. Conversion relations are:

$$1 \text{ Darcy} = 9.86923 \times 10^{-13} \text{ m}^2;$$

$$1 \text{ Darcy} = 10^3 \text{ milliDarcy} = 10^6 \text{ microDarcy} = 10^9 \text{ nanoDarcy}$$

The SI units of dynamic viscosity, pressure, and specific discharge are Pascal·second, Pascal, and meter/second, respectively.

Darcy's law gives the permeability calculation equation based on experimental measurements, with known or measurable information of the sample geometry, applied parameters and the fluid properties. In another words, the measured permeability by using Darcy's law depends on geometrical size of the sample, pressure drop, flux, fluid density, and viscosity. Its magnitude is a spatial average of a sample under fluid flow test. Thus, the permeability obtained by measurements based on Darcy's law is also called effective permeability. It is widely accepted as fundamental in permeability or flow-related studies.

However, the structural details inside the sample or material are still enigmas; for example, connected porosity, tortuosity of channels, connectivity, fluid properties, the degree of heterogeneity, and surface roughness of the channel. All of these properties define another term called intrinsic permeability. Intrinsic permeability is a function of medium structure only, i.e., it is independent of fluid properties or applied parameters. From the production point of view, intrinsic permeability is meaningless. This is because while there can be a totally different

production rate for heavy or light oil flow in the same medium under the same in-situ conditions, the permeability is the same. Thus, intrinsic permeability is not the study objective of this dissertation. We are more concerned with the flux or flow rate of a specific type of fluid flowing through a medium.

1.2 Hydraulic fracturing and shale reservoirs

Hydraulic fracturing has been a commonly used technique since the 1970s. Recently, it has become a hot topic again due to the shale gas revolution. Hydraulic fracturing can increase hydrocarbon production rate and total output amount. A large amount of water, sands, and chemicals are pumped into a subsurface formation during a fracturing operation. The role of sands in the slurry is to keep the generated fractures open.

In-situ stress magnitude and distribution decide both the failure pressure threshold of generating a hydraulic fracture and its growth orientation. When the treating pressure is higher than the threshold of the rock's failure point, a fracture is generated. The growth direction of a hydraulic fracture is perpendicular to the direction of minimum principal in-situ stress.

Hydraulic fracturing changes the formation structure in order to free the trapped hydrocarbon by increasing the drainage area, and by creating and connecting fractures. Figure 1-1 shows a diagram of hydraulic fracturing.

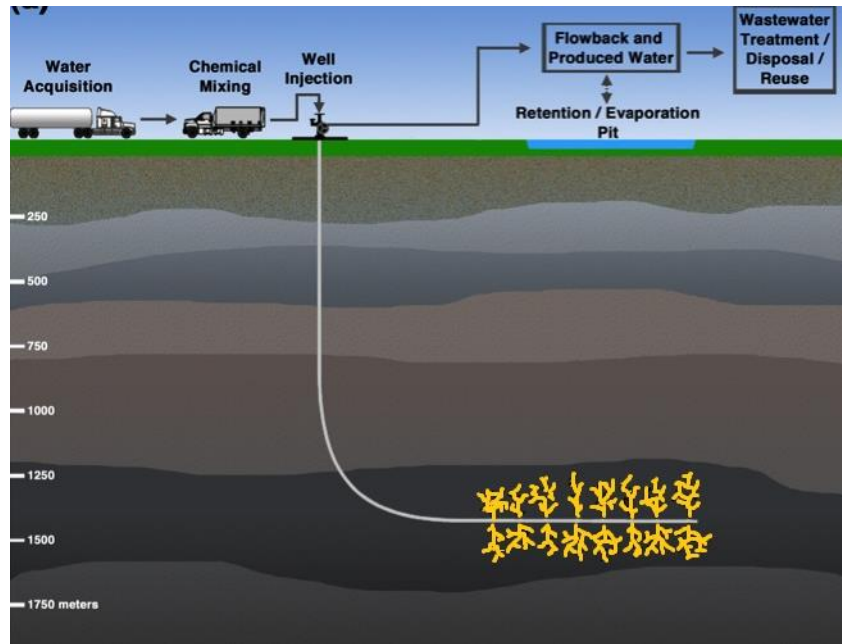


Figure 1-1 Hydraulic fracturing. The yellow-color dendritic structures along the horizontal interval of injection well represent fractures induced by pumping. (Alexi Sara Ernstoff and Brian R. Ellis, 2013)

In addition to shale gas reservoirs, the hydraulic fracturing technique could also be used for improving production of shale oil or tight sand reservoirs. Monitoring and understanding microseismic events induced by hydraulic fracturing could help us better characterize the dynamic change of reservoirs. Since the data we used in this dissertation were acquired from the Barnett gas shale formation, we give a brief introduction about shale gas and gas shale reservoirs.

Shale gas is high-efficiency, clean, and economic energy source. Figure 1-2 shows the identified shale gas plays widely distributed throughout the continental United States. Shale gas could potentially reliance on the pressures of pollution, hydrocarbon transportation, and reliance on imports from overseas.

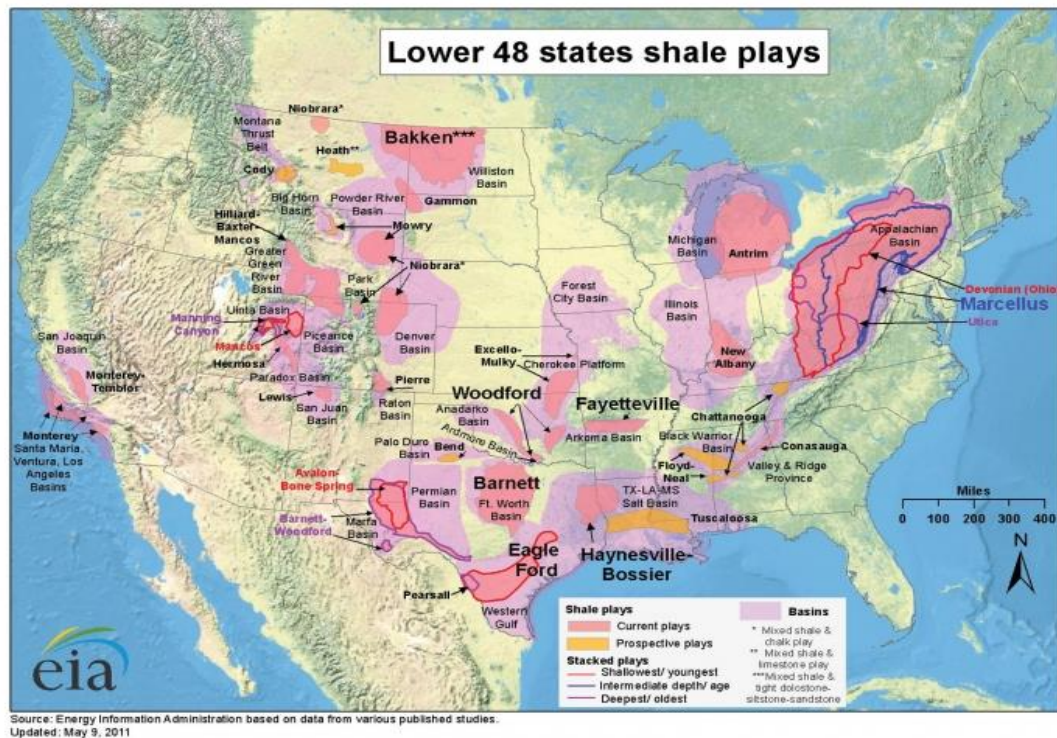


Figure 1-2 Identified shale gas plays in continental United States. (Theresa Andrejack Loux and Archie Filshill, 2013)

Gas shale is mainly composed of organic-rich, clay-sized consolidated particles. With appropriate temperature, pressure, and burial history, kerogen concentrate can be converted to hydrocarbon. For conventional reservoirs, after migrating from source rocks, oil and gas are usually stored in a sandstone formation. For unconventional reservoirs, shale formations generate hydrocarbon and serve as traps themselves. Advances in exploration and production techniques for conventional hydrocarbon reservoirs have been obtained in the last few decades. However, it is becoming more difficult to find economical onshore conventional reservoirs. At the same time, the risk and cost for offshore conventional reservoir exploration and

production are increasing. Thus, unconventional hydrocarbon reservoirs are attracting more attention, for example, shale gas and shale oil reservoirs.

Two characteristics of shale reservoirs are low permeability and anisotropy. Fortunately, for our study, we used core samples from the pumping well at the depth of the target layer. Plugs with different angles to the bedding plane were cut from core samples, as shown in Figure 1-3. Laboratory measurements showed that the permeability along the bedding plane is in the range of milliDarcy to microDarcy; the permeability normal to the bedding plane is around nanoDarcy (Metwally, 2010). This range of permeability is considered to be nonproductive. Thus, hydraulic fracturing is the key to improving production rate from this type of reservoirs and making them economical.



Figure 1-3 Three cylinder samples from one Barnett Shale core, along 0, 45, and 90 degrees to the bedding plane. The left picture is the illustration modified from Wang, 2002. The right picture is the phot of one set of our samples (core-B;AS6485).

1.3 Literature review

The only direct way to determine permeability is by implementing fluid transport measurements in a laboratory. Metwally and Chesnokov (2010) obtained permeability of Barnett shale samples along 0° , 45° , and 90° to bedding plane under in-situ high temperature and pressure conditions by laboratory measurement.

However, problems of laboratory measurement include:

- (1) core samples may not be available;
- (2) there is a high cost for experiments;
- (3) there are upscaling problems;
- (4) coring may destroy sample structures when confining pressure dramatically drops; and
- (5) time-lapse results cannot be given during pumping.

Further, because permeability is a highly-fluctuating parameter due to heterogeneities inside the samples, laboratory measurements could only give rock matrix permeability results assuming a homogenous structure inside. Thus, results obtained by laboratory measurement cannot be extrapolated.

Indirect methods include empirical equations of permeability, and analytical and numerical solutions based on different types of assumptions.

Empirical permeability equations could be established by a large number of sample measurements, or be derived based on a specific type of rock physics model with certain assumptions, for example, pore space is assumed to be connected.

Empirical equations are usually expressed by using rock physics parameters, including porosity, grain size, cementation degree, and specific surface area. This type of method does not take fluid properties, pressure drop, and inflow velocity into account. An example is the Kozeny-Carman equation, which is expressed as

$$\kappa = \frac{\pi R^4}{8A\tau}, \quad (1-2)$$

where A is the area of cross-section, τ is tortuosity, and R is cross-section radius (Carman, 1961). The Kozeny-Carman equation is derived from fluid flowing through a pipe which has a circular cross-section.

Shapiro *et al.* (1997) and Talwani and Acree (1984) used the point source diffusion model and obtained the subsurface hydraulic diffusivity according to the spatial-temporal distribution of microseismic events induced by fluid injection. This method is based on diffusion theory and Biot's theory. This method implicitly assumes all microseismic events are induced by an isotropic diffusion phenomenon.

However, some long-distance events at an early stage, which were induced by the combined effect of brittleness and in-situ stress distribution, would affect observation of events induced by fluid diffusion and permeability estimation. Also, shale formations are anisotropic. In the case of Shapiro *et al.* (1997), the reservoir was composed of sandstone. Besides, the monitoring scale in time and space was large in their case; for example, monitoring lasted for 60 hours and some events induced by fluid diffusion were located 1500m away from the single injection point. With this

time and space scale, the geometrical size of a hydraulic fracture could be negligible. Thus, long-distance events at the early stage do not severely affect the estimated result.

In many cases, however, monitoring scales in time and space are not always as large as that one; for example, monitoring may be stopped immediately when pumping stops. In this way, microseismic events induced by fluid back flow cannot be located.

Further, the relation between diffusivity and permeability is based on the empirical equation in the paper of Shapiro *et al.* (1997). Also, the diffusivity expression is obtained by use of diffusion theory and Biot's theory in their paper. Biot's theory assumes that pore space is all connected; this is a controversy still and not widely accepted for shale formations, especially before hydraulic fracturing.

Grechka *et al.* (2010) proposed another approach, based on inverting the diffusion equation under the assumption of 1-dimensional flow of the injected fluids from the faces of a hydraulic fracture. This accounts for the geometrical effect of the hydraulic fracture. It assumes the incompressible fluid flow into the surrounding formation everywhere along the hydraulic fracture faces, not at a single point source. This method could give the original permeability along the bedding plane only.

Based on diffusion theory, bulk modulus (or reciprocal of compressibility) is always involved when converting diffusivity to permeability, no matter whether using previous empirical equations or the theoretical one we derived. Previously, bulk

modulus was obtained by well logging data for isotropic sandstone reservoirs. This would introduce errors for the bulk modulus of anisotropic shale formations.

1.4 Methods

We started from 3-dimensional diffusion equation and wanted to understand the extensive properties transporting through control volume or control surface macroscopically. The diffusivity could be extracted by spatial-temporal distribution of the whole group of diffusing particles. Our reasoning was the diffusivity could be obtained by the microseismic event distribution in time and space, the theoretical relation between diffusivity and permeability would need to be found in the next step. Then permeability of the medium could be estimated by the spatial-temporal distribution of located microseismic events, as well.

The uncertainties of the permeability estimation results may come from the microseismic event location results, monitoring duration, quality of recorded seismograms, and monitoring design. In order to reduce uncertainties, we estimated permeability along different directional sectors. Meanwhile, we accounted for the geometry effect of hydraulic fracture.

If the moment tensor solution is unavailable or cannot be solved due to poor quality seismograms or monitoring design, for example, in our Dollie data case, the geometry of a hydraulic fracture needs to be calculated approximately with the help of

an assumed hydraulic fracture model and mass conservation of slurry.

Different from conventional sandstone reservoirs, shale is vertical transversely isotropic (VTI). Thus, effective medium theory was used for characterizing the bulk modulus of VTI medium in our study.

It is known that each located microseismic event corresponds to energy released from a specific coordinate, i.e., the medium has been changed at (x, y, z, t) . If we can make full use of each located microseismic event by extracting the geometrical size, orientation, and location of each microseismic event, a hydraulic fracture network could be built. In this way, simulation of fluid flow in fracture network would be helpful for the permeability estimation and reservoir modeling after hydraulic fracturing. Numerical flow simulation could provide time-lapse results of flux together with visual displays of the pressure and velocity fields inside.

Thus, we implemented fluid flow simulation according to in-situ condition parameters. These parameters, such as pressure or flow rate or a combination of these, were used as boundary conditions in the flow simulation. Because the fracture network of Dollie case is not available, we implemented flow simulation for specific flow domains and obtained flow flux results which provided the basis for permeability calculation in complicated flow domains. The specific flow domains used in this work were rectangular and periodic domains because they represented the fracture with both uniformly and non-uniformly distributed proppants.

Also, flow simulations in two types of synthetic media were tested. One

type of medium was composed of shale matrix only; and the other was composed of shale matrix and a width-constant fracture. These gave us angular-dependent and scale-dependent permeability results.

1.5 Dissertation layout

In Chapter 2, firstly, we introduce fluid diffusion theory and interpret diffusion in a statistical way. Secondly, we derive the expression of permeability in terms of diffusivity for incompressible fluid under isothermal condition. Thirdly, we give a brief introduction related to microseismic monitoring techniques, such as microseismic event location methods, moment tensor, and magnitude analysis. After that, we test the Dollie data acquired from a Barnett Shale gas reservoir and obtain permeability results before and after hydraulic fracturing. Finally, we give a summary and discussion about this method.

Chapter 3 presents how numerical methods are used for fluid flow simulation and gives the simulation results of fluid flow in different synthetic media. Firstly, we start from mass and momentum conservation equations to the Navier-Stokes equation, and then we briefly introduce the numerical methods used in this dissertation. After that, we describe how we used the staggered grid method for simple geometry flow simulation and the finite element method for complicated geometry flow simulation. Thirdly, we describe how we simulated fluid flow in a

synthetic medium and tested for angular-dependent and scale-dependent effects.

Chapter 4 includes our conclusions, discussion and recommendation for future work.

Chapter 2 Diffusion method

2.1 Introduction

Diffusion is a type of transport phenomenon existing in nature; for example, momentum, mass, and energy can be transported from high concentration to low concentration. The transport phenomena of momentum, heat, and mass are governed by Newton's law considering fluid viscosity, Fourier's law, and Fick's law, respectively. They have the same mathematical expression form and all obey constitutive and conservation equations.

Figure 2-1 shows the diagram of diffusion phenomena in which diffusing particles travel along the direction of concentration gradient. The general form of diffusion equation is:

$$\frac{\partial c}{\partial t} = D \nabla^2 c, \quad (2-1)$$

where c is a type of the specific property; for example, c could be pressure for mass diffusion, or it could be temperature for thermal conduction. In this study we focus on

fluid diffusion; thus, c , D , and t represent pressure, hydraulic diffusivity, and time, respectively.

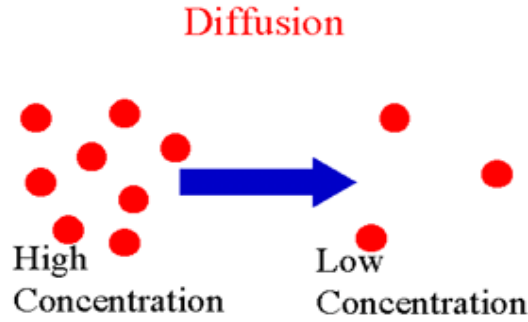


Figure 2-1 The property is transported from high concentration to low concentration. The transported property could be mass, momentum, or energy and is represented by the red dots

Hydraulic diffusion phenomena occur if a group of interacting particles are in an environment in which viscous forces play a major role compared to inertial forces, i.e., there is a low Reynolds number. In fluid mechanics, a “small” Reynolds number means its value is lower than 4000, in general (Munson *et al.*, 1990). The Reynolds number is expressed as

$$R = \frac{\rho v_s L}{\eta},$$

where ρ , v_s , and η represent the density of fluid, average velocity of fluid, and dynamic viscosity of fluid; L characterizes the size of flow domain; for example, the diameter of a pipe.

Field scale permeability information of the hydrocarbon reservoirs cannot

be directly obtained by measurement. Thus, finding an alternative way is necessary. We know that the fluid which is able to flow through a medium must simultaneously satisfy the following three conditions: pressure drop, connected pore space, and appropriate viscosity. Permeability describes the ease of fluid transmitting in the medium. Meanwhile, diffusivity characterizes the flux due to the concentration gradient in the medium. Both diffusivity and permeability evaluate the fluid flow. We try to obtain permeability by diffusion observation.

In this chapter, firstly, we interpret the diffusion procedure from a statistical prospective. We want to extract diffusivity by analyzing the spatial-temporal distribution of diffusing particles as diffusion evolves. Secondly, we theoretically derive the expression between permeability and diffusivity for incompressible fluid under isothermal condition. Thirdly, we give a brief introduction about microseismic techniques, including microseismic acquisition, event location, and moment tensor, because microseismic monitoring is the fundamental tool for our permeability estimation. Fourthly, we test the Dollie data acquired from a Barnett Shale reservoir and obtain permeability before and after hydraulic fracturing. Summary and discussion are given in the end.

2.2 Interpretation of diffusion procedure

The three-dimension diffusion equation could be written as

$$\frac{\partial P}{\partial t} = D \left(\frac{\partial^2 P}{\partial x^2} + \frac{\partial^2 P}{\partial y^2} + \frac{\partial^2 P}{\partial z^2} \right). \quad (2-2)$$

This diffusion equation is linear and separable in a common coordinate system (Hu and Ni, 1989).

It is known that more than one solution exists for a linear differential equation. The general form of solution P due to an initial perturbation, is written as

$$P(\mathbf{x}, t) = \frac{1}{(2\pi)^3} \int e^{-D|\mathbf{k}|^2 t} e^{-i\mathbf{k} \cdot (\mathbf{x} - \mathbf{x}_0)} d\mathbf{k} = \frac{1}{(4\pi Dt)^{3/2}} e^{-\frac{(\mathbf{x} - \mathbf{x}_0)^2}{4Dt}} \quad (\text{Ursell, 2007}) \quad (2-3)$$

where \mathbf{x}_0 represents the coordinates of pumping source; \mathbf{k} is frequency in vector form, i.e., $\mathbf{k} = (k_x, k_y, k_z)$; \mathbf{x} is the coordinate in vector form, i.e., (x, y, z) ; \mathbf{x}_0 is the coordinate of the initial perturbation occurs; D is diffusivity; and t is the time after the perturbation occurs.

Due to uncountable molecules involved in the motion of continuously deforming fluid, we prefer the Eulerian frame of reference to the Lagrangian frame of reference for describing fluid motion. Each diffusing particle still obeys Newton's laws of motion, but we focus more on the distribution of the whole group of diffusing particles during diffusion. A group of diffusing particles evolving can be described as probability density in space. This is from a statistical way to analyze the evolution of a group of diffusing particles.

When the word “statistical” is mentioned, it is natural that different types of average methods come to mind, each of them with its own corresponding physical meaning. The result of simple averaging of diffusing particles distribution for

isotropic diffusion is the same as the initial position and is not related to the diffusion rate. However, we need to find a measure for diffusing particle distribution evolving with time. Root-mean-square could describe the fluctuating of diffusing particles' distribution in time and space. Figure 2-2 gives an example of isotropic diffusion for a group of diffusing particles. From time t to $t + \Delta t$ the simple average position of the whole group of particles is the same. But the root-mean-square average could tell us more about the distribution of diffusing particles in space as time evolves. Thus, the root-mean-square average is the one we choose to use.

Distribution of diffusing particles at different time

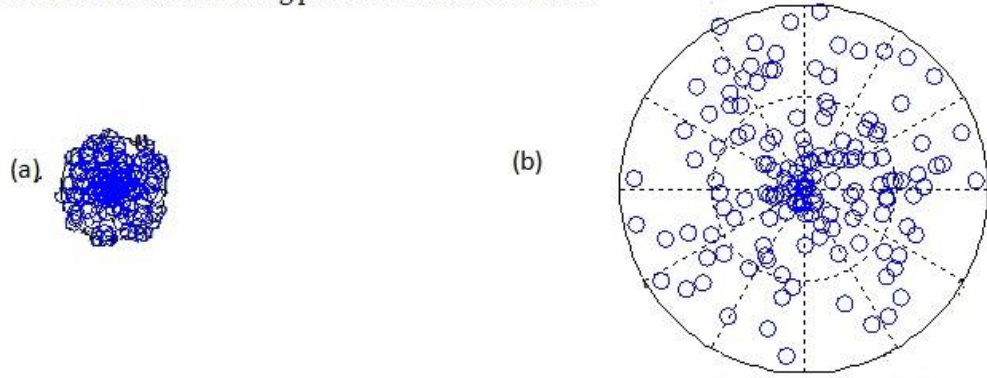


Figure 2-2 A diffusion procedure at different time: (a) distribution of particles at t_1 and (b) distribution of particles at $t_1 + \Delta t$

According to Equation 2-3, the root-mean-square average and its expression is

$$\langle \mathbf{x}^2 \rangle(t) = \int |\mathbf{x}_0|^2 + 6Dt . \quad (2-4)$$

This tells us the root-mean-square average diffusing distance of all particles obeying

$r_{RMS} = \sqrt{6Dt}$. This expression contains root-mean-square distance r , diffusing time t , and diffusivity D simultaneously. The root-mean-square average gives the fluctuation of the variable, specifically, diffusing distance.

The root-mean-square average of the diffusing distance could help us analyze diffusivity according to observations of the microseismic event location. The purpose of this study is to extract field scale permeability with the help of microseismic monitoring. Thus, our next step is to find the relation between diffusivity and permeability.

2.3 Diffusivity and permeability

In this section, we give the derivation between permeability and diffusivity based on mass conservation and Darcy's law; this differs from the empirical expression.

We assume the proppants and liquid are incompressible. This is reasonable because liquid is practically considered as incompressible and proppants are made of high hardness material. Also, we assume the isothermal condition while pumping. We obtain the expression of mass conservation as

$$\nabla \cdot (\rho \mathbf{u}) = \frac{\partial(\rho \phi)}{\partial t}, \quad (2-5)$$

where ρ is the density of fluid, ϕ is the connected porosity of the formation, and \mathbf{u} is the vector form of specific discharge or volumetric flux (unit in m/s).

The tensor form of Darcy's law is written as Equation 1-1

$$\mathbf{u} = \frac{\mathbf{\kappa}}{\eta} \nabla P,$$

where \mathbf{u} is specific discharge (unit in m/s).

By substituting Equation 1-1 back to Equation 2-5, we obtain

$$\nabla \cdot (\rho \nabla P) = \mathbf{\kappa}^{-1} \eta \frac{\partial(\rho \phi)}{\partial t}. \quad (2-6)$$

The right-hand side of Equation 2-6 can be rewritten as $\mathbf{\kappa}^{-1} \eta (\rho \frac{\partial \phi}{\partial t} + \phi \frac{\partial \rho}{\partial t})$.

Under isothermal condition, the expressions of fluid compressibility and rock matrix compressibility according to their definition are

$$C_f = \frac{1}{\rho} \left(\frac{\partial \rho}{\partial P} \right)_T \quad (2-7)$$

$$\text{and } C_r = \frac{1}{\phi} \left(\frac{\partial \phi}{\partial P} \right)_T. \quad (2-8)$$

Combining with the chain rule, the part in the bracket of the right-hand side from Equation 2-6 can be written as

$$\rho \frac{\partial \phi}{\partial t} + \phi \frac{\partial \rho}{\partial t} = \rho \phi C_r \frac{\partial P}{\partial t} + \phi C_f \rho \frac{\partial P}{\partial t} = \rho \phi (C_r + C_f) \frac{\partial P}{\partial t}.$$

For simplicity, we only consider the component along the x-axis, and we obtain

$$\frac{\partial}{\partial x} (\rho \nabla P) = \frac{\eta}{\kappa_x} \rho \phi (C_r + C_f) \frac{\partial P}{\partial t}. \quad (2-9)$$

We expand the spatial derivative and obtain

$$\rho \frac{\partial^2 P}{\partial x^2} + \frac{\partial P}{\partial x} \frac{\partial \rho}{\partial x} = \frac{\phi \eta (C_f + C_r)}{\kappa_x} \rho \frac{\partial P}{\partial t}. \quad (2-10)$$

Again, by use of the chain rule and the expression of fluid compressibility,

the second term on the left-hand side of Equation 2-10 can be written as,

$$\frac{\partial P}{\partial x} \frac{\partial \rho}{\partial x} = \frac{\partial P}{\partial x} \frac{\partial \rho}{\partial P} \frac{\partial P}{\partial x} = \frac{\partial \rho}{\partial P} \left(\frac{\partial P}{\partial x} \right)^2 = C_f \left(\frac{\partial P}{\partial x} \right)^2, \quad (2-11)$$

is too small and negligible because the liquid is practically considered as incompressible.

Then we obtain

$$\frac{\partial^2 P}{\partial x^2} = \frac{\phi \eta (C_f + C_r)}{\kappa_x} \frac{\partial P}{\partial t}. \quad (2-12)$$

Compared with classical diffusion equation, as shown in Equation 2-2, we obtain

$$D_x = \frac{\kappa_x}{\phi \eta (c_f + c_r)}. \quad (2-13)$$

Similarly, the expressions are obtained for y- and z-components in a similar way. Then we find the tensor form expression between permeability and diffusivity is

$$\mathbf{D} = \frac{\mathbf{\kappa}}{\phi \eta (c_f + c_r)}, \quad (2-14)$$

where \mathbf{D} and $\mathbf{\kappa}$ represent diffusivity and the permeability tensor, respectively.

2.4 Overview of microseismic monitoring

In order to better understand the dynamic change of reservoirs induced by hydraulic fracturing, the microseismic monitoring technique is used as the first choice

in the oil and gas industry. Compared with other tools, such as temperature logging and tiltmeter surveys, microseismic monitoring can potentially give the information about fractures, such as length, height and preferred growing orientation in real time.

Microseismic monitoring is important for engineers to understand the dynamic change of reservoirs and help them make further-step decisions; for example, ascertaining the direction of the fracture growth, changing pumping strategies, and avoiding to contaminate drinking water zones or activating fault zones. Microseismic monitoring could provide microseismic event locations, moment tensor solutions, and the geometrical size of fractures.

2.4.1 Microseismic event location

The purpose of microseismic event location is to find the onset times and the coordinates of microseismicities. The principle is similar to that used in global earthquake location. Seismograms, which contain the propagation information of seismic waves, were recorded by geophones. Traditionally, after picking the arrival times of different types of waves from seismograms, we could obtain the event location with the help of a velocity model. The main challenge of locating microseismic events is that weak signals can be contaminated by noise. Figure 2-3 shows the microseismic magnitude and corresponding information, such as recording range, moment, slip and area, and equivalent explosive charge.

Moment Mag	Comments	Recording Range (feet)	Moment (MNm)	Slip and Area	Equivalent Explosive Charge
-4	Smallest we can record	<100	001	10 μm / 0.003 m^2	1 mg
-3	-	~1500	0.04	40 μm / 0.03 m^2	30 mg
-2	Big for Barnett	~2500	1	0.1 mm / 0.3 m^2	1 g (blasting cap)
-1	Biggest in Barnett	~5000	40	0.4 mm / 3 m^2	30 mg
0	Limit of "microseismic" Biggest at Ekofisk	>10000	1,000	1 mm / 30 m^2	1 kg stick of explosive
1	Largest event Habanero geothermal	-	40,000	4 mm / 300 m^2	30 kg
2	-	-	1,000,000	1 cm / 3,000 m^2	1 ton
3	Felt earthquake	-	40,000,000	4 cm / 0.03 km^2	30 ton

Figure 2-3 Moment magnitude, moment of microseismic, and equivalent explosive charge (Evgeny Chesnokov, "Microseismics: Integrated, Advanced Geophysics", class lecture, Microseismic, Natural Sciences and Mathematics, Houston, TX, Aug 27, 2012).

Figures 2-4, 2-5, and 2-6 show seismograms with different noise levels; note that signal-noise ratios of all three are higher than 1. As the signal-noise ratio decreases, accurately picking the arrivals of waves is becoming difficult.

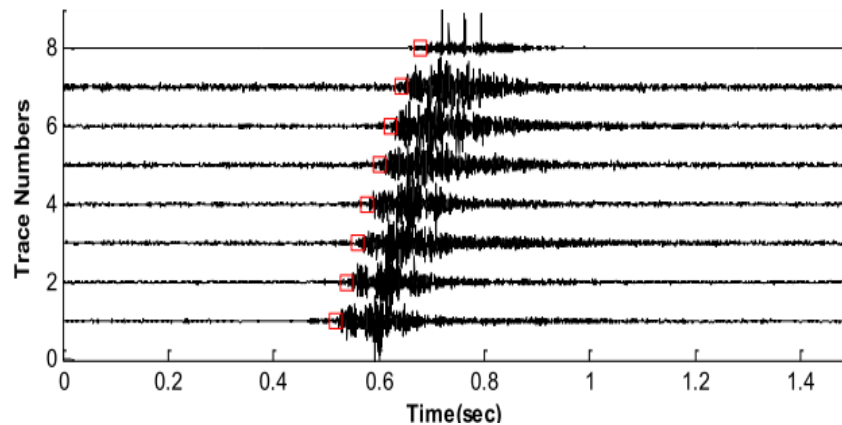


Figure 2-4 Light noise contamination and arrival-time picking results (Evgeny Chesnokov, "Microseismics: Integrated, Advanced Geophysics", class lecture, Microseismic, Natural Sciences and Mathematics, Houston, TX, Aug 27, 2012).

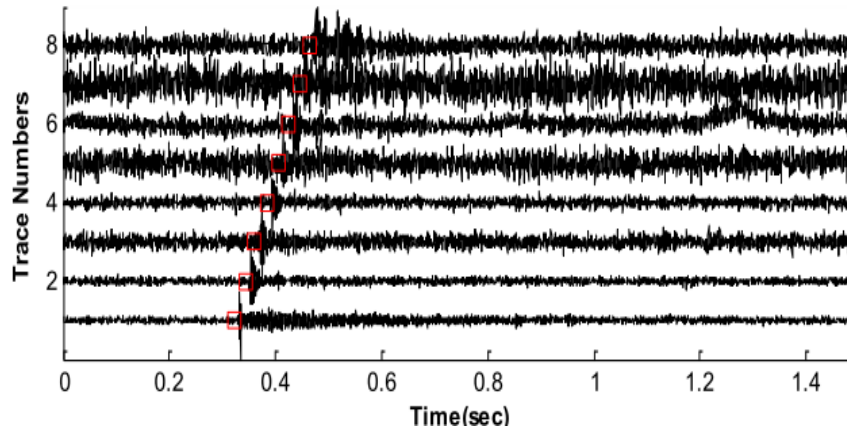


Figure 2-5 Moderate noise contamination and arrival-time picking results (Evgeny Chesnokov, “Microseismics: Integrated, Advanced Geophysics”, class lecture, Microseismic, Natural Sciences and Mathematics, Houston, TX, Aug 27, 2012).

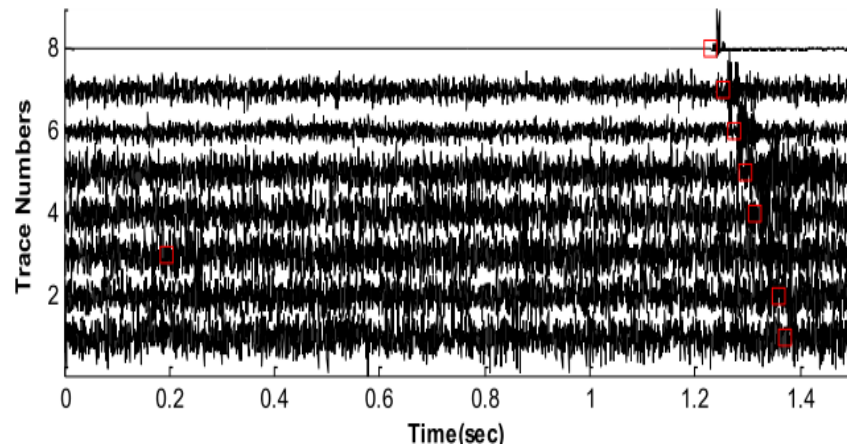


Figure 2-6 Severe noise contamination and arrival-time picking results (Evgeny Chesnokov, “Microseismics: Integrated, Advanced Geophysics”, class lecture, Microseismic, Natural Sciences and Mathematics, Houston, TX, Aug 27, 2012).

From the acquisition point of view, microseismic monitoring falls into two main categories.

The traditional one is downhole monitoring, which is typically a downhole geophone array deployed in a monitoring well as shown in Figure 2-7. Sometimes, two or more monitoring wells are used.

The other is surface monitoring, which is geophones deployed on the ground

surface or at a shallow depth, as shown in Figure 2-8.

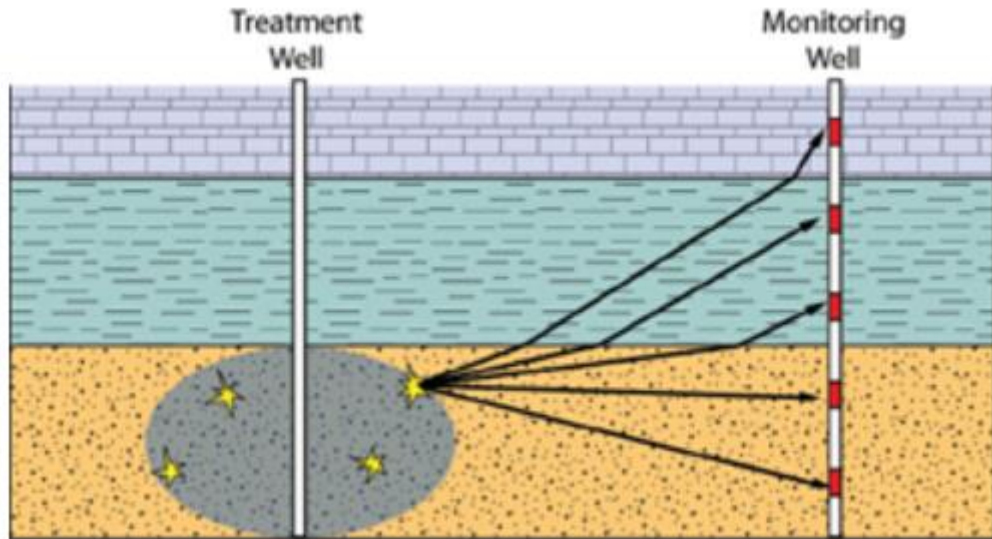


Figure 2-7 An example of downhole monitoring. The injection well is on the left. The monitoring well is on the right. The red rectangular points represent geophones (National Research Council, 2012).

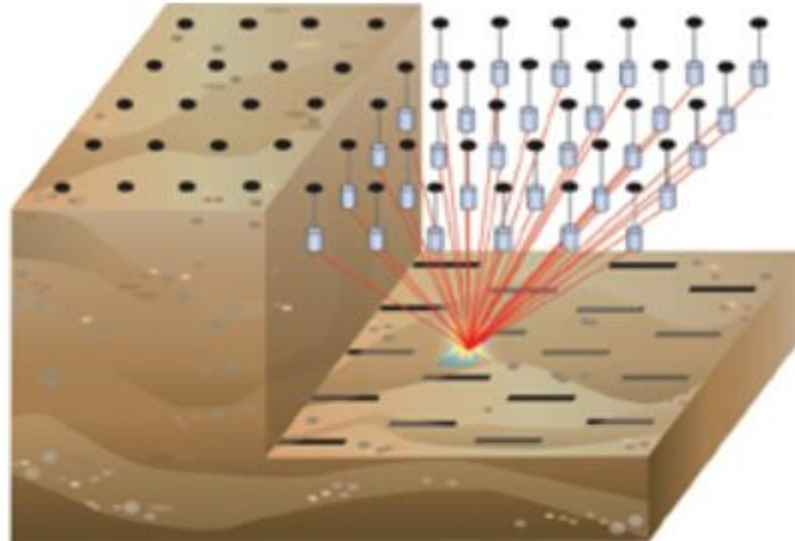


Figure 2-8 Surface monitoring (National Research Council, 2012).

Generally, downhole monitoring records good quality data because the geophones are closer to the microseismic sources in space; recorded seismograms

contain weak interference from human activities. In most cases, algorithms based on downhole monitoring belong to arrival-picking methods. This type of method requires accurately picking P- and/or S-wave arrival times and subsurface velocity model. Its principle is the same as that used for locating the hypocenter of a global earthquake; the theoretical travel times from the source to each geophone are calculated by use of the velocity model, and the hypocenter is located by optimizing a misfit function between the measured travel times and theoretically calculated ones (Aki and Richards, 2002). Arrival-picking methods are usually computationally inexpensive. The disadvantage of downhole monitoring is that solid angle coverage is limited because a single-monitoring well is commonly used.

In order to reduce the uncertainty of arrival-time picking, especially for weak events, relative location methods are used. By applying waveform cross-correlations between a master event and weak ones, the arrival time differences compared to the master event are obtained (Schaff *et al.*, 2004; Schaff and Waldhauser, 2005; Schaff, 2008).

Manual picking of P- and S-wave arrivals could achieve high picking accuracy, but it is time-consuming, due to the thousands of microseismic events induced during a hydraulic fracturing operation. A lot of effort has been made to develop automatic picking algorithms, including short-term-average and long-term average (Earle and Shearer, 1994), supper-Gaussian method (Liao *et al.* 2011), energy analysis (Earle and Shearer, 1994), and polarization analysis (Vidale, 1986).

The second main type of microseismic event location methods is migration-based, and it is mainly used for surface-monitoring. These methods locate microseismic events by using full wavefields. This type of method also requires an accurate velocity model and the wide-bandwidth frequency components of recorded signals. The advantage of migration-based methods is that they locate weak events without requiring accurately picked seismic wave-arrivals. Instead, the principle is focusing energy at the hypocenter by use of time-reversal (Baysal *et al.*, 1983; Gajewski and Tessmer, 2005). These methods can locate microseismic events from poor quality data, such as those with signal-noise ratio lower than 1 (Gajewski and Tessmer, 2005). The disadvantage of migration-based methods is their high computational cost.

In general, any microseismic event location algorithm cannot claim that its error is less than a certain distance because we do not know the true source coordinate (Chesnokov, personal communication). The only reliable way to test a location algorithm is to locate a source with known coordinates in a physical model and then compare with the true coordinates. The location algorithm, UHFracDetect, used in this work has been tested on physical models, for example, on a multi-layered model with vertical transversely isotropic layers.

2.4.2 Moment tensor and seismic magnitude analysis

The moment tensor is a simplified mathematical description of a focal mechanism in global seismology. Recorded seismograms can help us obtain a 2nd order moment tensor which contains the mechanism of failures. The moment tensor

can be expressed as $M = M_0 \begin{bmatrix} M_{11} & M_{12} & M_{13} \\ M_{21} & M_{22} & M_{23} \\ M_{31} & M_{32} & M_{33} \end{bmatrix}$,

(Lay and Wallace, 1995), where M_0 is the seismic moment, and M_{ij} represents a force couple composed of opposing unit forces. M is real and symmetric; thus, only six independent components exist (Jost and Herrmann, 1989). The moment tensor also can be represented geometrically, by a beach ball diagram, which is a lower hemisphere stereographic projection, as shown in Figure 2-9. Conventionally, the black quadrants represent the first recorded P-wave as a compressive wave and the white quadrants represent the first recorded P-wave as a tensional wave. The real fault plane is one of the nodal planes. However, the fault plane cannot be determined by use of the beach ball diagram only.


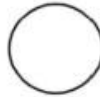










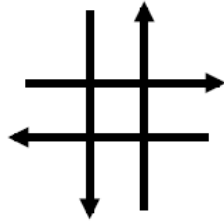
Moment tensor	Beachball	Moment tensor	Beachball
$\frac{1}{\sqrt{3}} \begin{pmatrix} 1 & 0 & 0 \\ 0 & 1 & 0 \\ 0 & 0 & 1 \end{pmatrix}$		$-\frac{1}{\sqrt{3}} \begin{pmatrix} 1 & 0 & 0 \\ 0 & 1 & 0 \\ 0 & 0 & 1 \end{pmatrix}$	
$-\frac{1}{\sqrt{2}} \begin{pmatrix} 0 & 1 & 0 \\ 1 & 0 & 0 \\ 0 & 0 & 0 \end{pmatrix}$		$\frac{1}{\sqrt{2}} \begin{pmatrix} 1 & 0 & 0 \\ 0 & -1 & 0 \\ 0 & 0 & 0 \end{pmatrix}$	
$\frac{1}{\sqrt{2}} \begin{pmatrix} 0 & 0 & -1 \\ 0 & 0 & 0 \\ -1 & 0 & 0 \end{pmatrix}$		$\frac{1}{\sqrt{2}} \begin{pmatrix} 0 & 0 & 0 \\ 0 & 0 & -1 \\ 0 & -1 & 0 \end{pmatrix}$	
$\frac{1}{\sqrt{2}} \begin{pmatrix} -1 & 0 & 0 \\ 0 & 0 & 0 \\ 0 & 0 & 1 \end{pmatrix}$		$\frac{1}{\sqrt{2}} \begin{pmatrix} 0 & 0 & 0 \\ 0 & -1 & 0 \\ 0 & 0 & 1 \end{pmatrix}$	
$\frac{1}{\sqrt{6}} \begin{pmatrix} 1 & 0 & 0 \\ 0 & -2 & 0 \\ 0 & 0 & 1 \end{pmatrix}$		$\frac{1}{\sqrt{6}} \begin{pmatrix} -2 & 0 & 0 \\ 0 & 1 & 0 \\ 0 & 0 & 1 \end{pmatrix}$	
$\frac{1}{\sqrt{6}} \begin{pmatrix} 1 & 0 & 0 \\ 0 & 1 & 0 \\ 0 & 0 & -2 \end{pmatrix}$		$-\frac{1}{\sqrt{6}} \begin{pmatrix} 1 & 0 & 0 \\ 0 & 1 & 0 \\ 0 & 0 & -2 \end{pmatrix}$	

Figure 2-9 Moment tensors and corresponding beach ball diagrams (Stein and Wysession, 2009)

Three basic types of seismic mechanisms are isotropic, double-couple, and the compensated linear vector dipole (CLVD). A real seismic source can be equivalently represented by any of these, or a certain percentage combination of two or all three. Figure 2-10 shows the three basic types of sources.

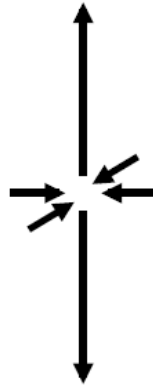
Force couples



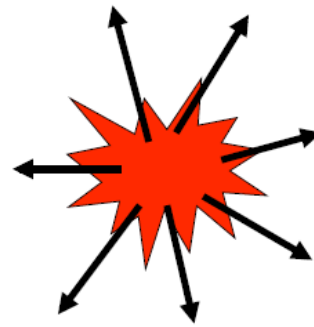
Beach balls



double couple



compensated linear
vector dipole



isotropic

Figure 2-10 Three types of force couples and their corresponding beach ball diagrams

The source mechanism of a microseismic event can be determined according to the eigenvectors and eigenvalues of its corresponding moment tensor (Jost and Herrmann, 1989).

Generally, large solid angle coverage by geophones surrounding the source location and high quality seismograms are favorable factors to solve moment tensor (Baig and Urbancic, 2010). In real situations, the commonly-used monitoring design is a single array of geophones deployed in a monitoring well.

A single array of downhole geophones cannot solve the full moment tensor solution (Eaton, 2009; Vavryčuk, 2007). It might even give unstable inversion solutions. Recently, Song and Toksoz (2011) proposed that full waveforms could help

solve the full moment tensor if the microseismic event location is close to the single-monitoring well, i.e., less than five times the dominant S-wave wavelength. However, the locations of all events would widely and be randomly distributed in space, so not every event could satisfy this requirement.

The purpose of solving the moment tensor solution of each microseismic event is to understand the failure mechanism and to find the fault plane orientation. The purpose of microseismic magnitude analysis is to obtain source radius according to radiated energy in an empirical way. The radius of a fault plane is assumed to be proportional to the P-wave or S-wave velocity divided by the corner frequency (Abercrombie, 1995; Brune, 1970; Brune, 1979). This method could be applied for global earthquakes as well as in microseismicity.

Microseismic source location combines with source orientation and radius are the basis for building the fracture network which is the prerequisite for reservoir fluid flow simulation.

2.5 A case study

The relation between diffusivity and permeability has been derived. Diffusivity is characterized by using the root-mean-square average of the diffusing particles distribution in time and space. However, there is an implicit assumption between particles' diffusing and microseismic events.

The assumption is that the state of stress in the crust is close to a failure equilibrium. An increase of pore pressure caused by fluid injection and pressure relaxation changes the effective normal stress and friction coefficients of the rock mass and induces microseismicity (Shapiro *et al.*, 1997; Talwani *et al.*, 1984), i.e., all events are diffusion-induced.

In real cases, however, rock failure under in-situ conditions is a complicated problem. For example, microseismic events could be induced by pore pressure relaxation. They also could be induced by effects of rock brittleness and in-situ stress distribution combined. Interpreting moment tensor could be helpful. However, the moment tensor solution may be unavailable or not fully solved due to monitoring design.

Also, the point source model should be modified because the purpose of hydraulic fracturing is to change the medium by generating or connecting fractures. Another challenge is that even if the microseismic events which are really induced by fluid diffusion originating from the source with geometrical size, it is difficult to decide which part of the source is the origin of diffusion. This effect could be negligible only if the size of the source were small compared with the monitoring scale in time and space. If not, we could only obtain permeability parallel and perpendicular to the dominant fracturing direction.

Next, we try to extract permeability before and after hydraulic fracturing from a real study.

2.5.1 Dollie data acquisition and processing

A microseismic survey was performed during the hydraulic fracturing stimulation of a Barnett Shale gas reservoir. The Barnett Shale is located in the Bend Arch-Fort Worth Basin. The sedimentary rocks were formed in the Mississippian period, and consist of organic-rich shale and limestone. The formation includes three layers, a lower shale, a middle limestone, and an upper shale, as shown in Figure 2-11.

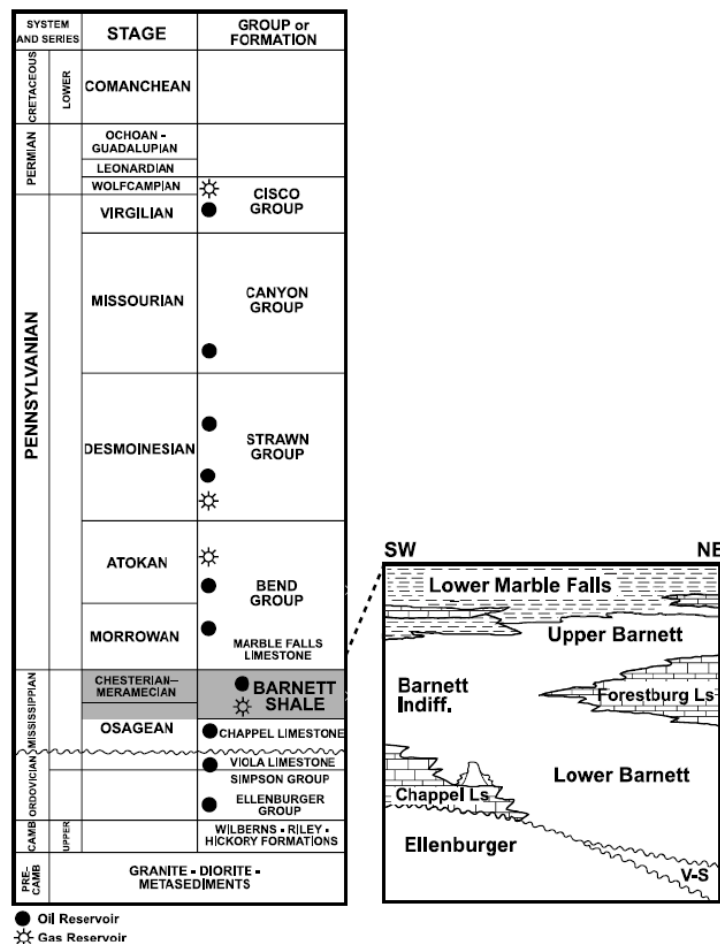


Figure 2-11 Fort Worth Basin- Generalized stratigraphy section of the Bend Arch (Montgomery *et al.*, 2005).

In this case, the vertical injection well, Dollie, was approximately 275m away from the vertical single monitoring well. Both wells had cemented casings. Further, the injection well was installed with two perforation guns. A twelve level 3-C geophone array was deployed in the monitoring well at a depth range from 2139m to 2271m; we refer the shallowest as 1 and the deepest as 12. The spacing between geophones was 12.192m. The orientations of geophones at each level were unknown at the beginning. Their orientations were determined by use of signals from casing perforation shots. Shot signals were also used for building and checking the velocity model. We set the top of the monitoring well as the origin of the coordinate system. There were two pumping points. One was at the depth of 2239m and the other at the depth of 2270m.

The proppants in the slurry were sieved before pumped into the subsurface formation, and their grain size were narrowly distributed around the 4mm range with sphericity higher than 9/10.

The hydraulic stimulation was designed as follows: a total of 3700m³ slurry, composed of 1.17 specific-gravity brine, HCL acid, slickwater, and proppant, was pumped into the target layer; pumping pressure was around 3000 psi. The dynamic viscosity of slurry equalled to $3 \times 10^{-5} Pa \cdot s$. The perforation section had 4.5 inch production casing which was cemented with acid-soluble cement. The perforation was designed to have a N45 °E/ N135 °E azimuths. The injection lasted for approximately 8 hours and the monitoring for 18.6 hours.

During hydraulic fracturing, the UHFracDetect software recorded, processed, and located microseismic events in real time. Theoretically, the ambient noise level of downhole monitoring is lower than that of surface monitoring. But some signals were still contaminated by severe noise, for example, typical noisy data are shown in Figure 2-12.



Figure 2-12 A typical example of recorded noisy data (Osakwe, 2013)

The UHFracDetect software filtered the data first, and then identified events by use of a detection algorithm and by removing poor quality detections. Finally, the selected events were located by grid searching within a 3-D domain. The total number of located microseismic events was 1425.

The UHFracDetect software is based on the arrival picking method. The signal-to-noise ratio of a locatable threshold is 1.3. For arrival picking-based methods, the velocity model is a crucial factor for good location results. In this case, the initial

velocity model was built according to sonic logs. Then, it was modified in order to minimize the differences between the calculated locations of the perforation shots and their known positions. This location result yielded 3-D treatment images and information for further analysis. Figures 2-13 and 2-14 show the map view and cross-section view of microseismic event location results. The red point or line represents the monitoring well. The black point or line represents the injection well. Each small point inside represents a microseismic event, and its color and size represent the onset time since injection started and magnitude of microseismic activity, respectively.

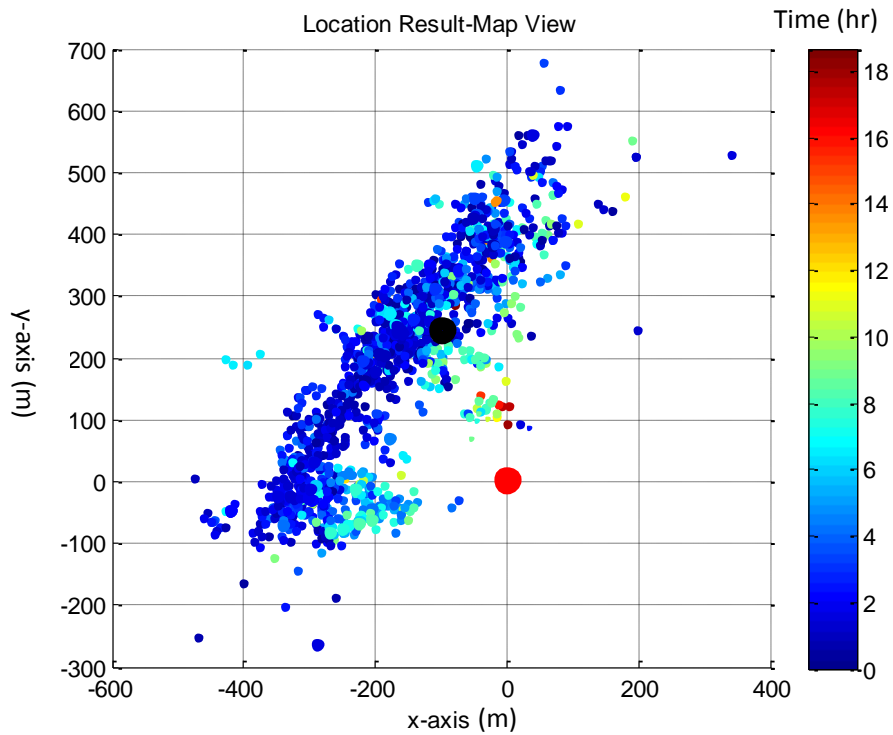


Figure 2-13 Map view of event location results

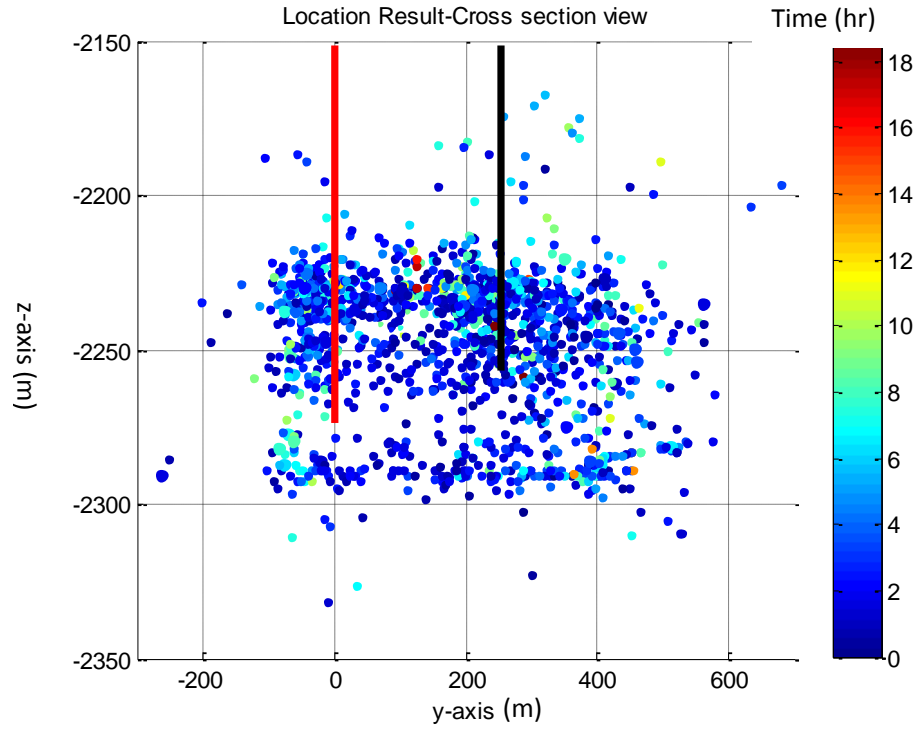


Figure 2-14 Cross-section view of event location results

The stimulated rock volume (SRV) of the Dollie data equaled $2.97 \times 10^7 \text{ m}^3$ (Lambordi, 2014), as shown in Figures 2-15 and 2-16. The so-called “field scale” is defined by the SRV.

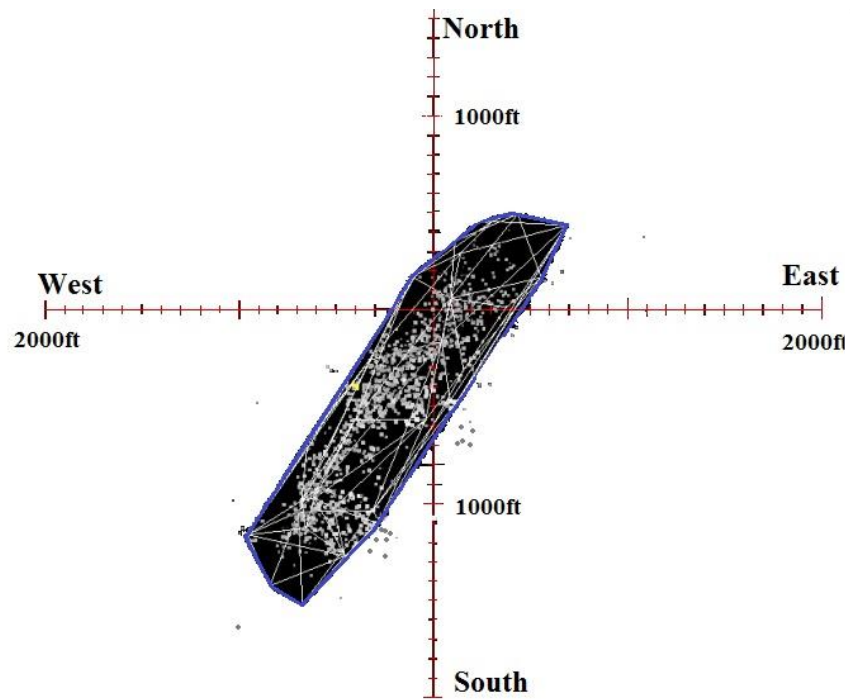


Figure 2-15 Stimulated rock volume (SRV) after hydraulic fracturing (Lambordi, 2014)

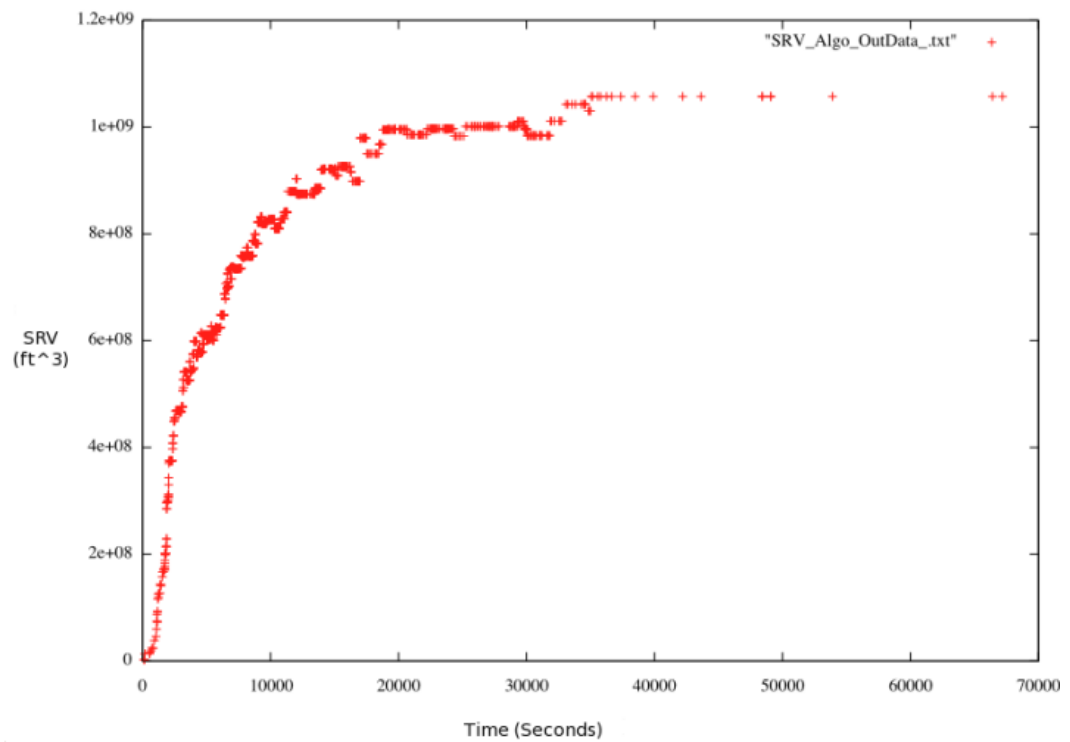


Figure 2-16 Increasing cumulative volume of SRV during injection (Lambordi, 2014)

Figure 2-17 shows the number of microseismic events in each 10-minute interval. Most events were induced at the beginning of the pumping stage. Injection lasted for eight hours. Then, the downhole pressure gradient reversed and fluid started to flow back. The number of located events increased immediately at eight hours.

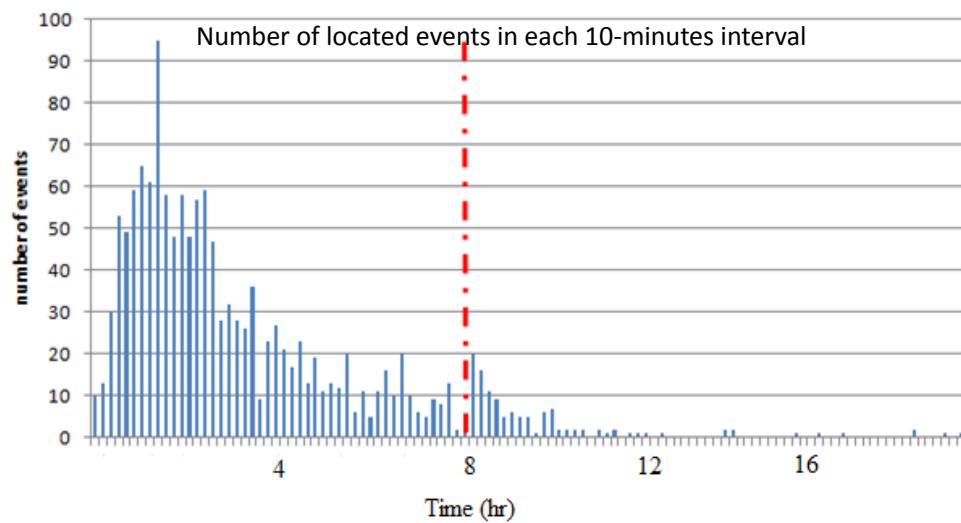


Figure 2-17 Number of located microseismic events in each 10-minute time interval. The red dash line represents the time of pumping stopped.

Further, according to well logging data, the target layer before hydraulic fracturing was 6%. The density of this shale formation is 2.55g/cm^3 . By use of the effective medium theory (Chesnokov and Bayuk, 2010), we extracted the stiffness tensor of this shale formation (VTI) from five standard logs as:

$$C_{pq} = \begin{pmatrix} 37.75 & 6.97 & 8.2 & 0 & 0 & 0 \\ & 37.75 & 8.2 & 0 & 0 & 0 \\ & & 33.22 & 0 & 0 & 0 \\ & & & 13.20 & 0 & 0 \\ & & & & 13.20 & 0 \\ & & & & & 15.39 \end{pmatrix} \quad (\text{units in GPa})$$

Based on the solved stiffness tensor, the corresponding effective bulk modulus of this VTI medium was calculated and its value equalled 0.028 GPa. This calculated effective bulk modulus was used for calculating permeability based on diffusivity.

2.5.2 Dollie data interpretation

With the event location results, we were able to plot the distribution of all these events, as shown in Figure 2-18. “r” represents the distance between each microseismic event and the injection point. “t” represents the time of each microseismicity occurred since injection started.

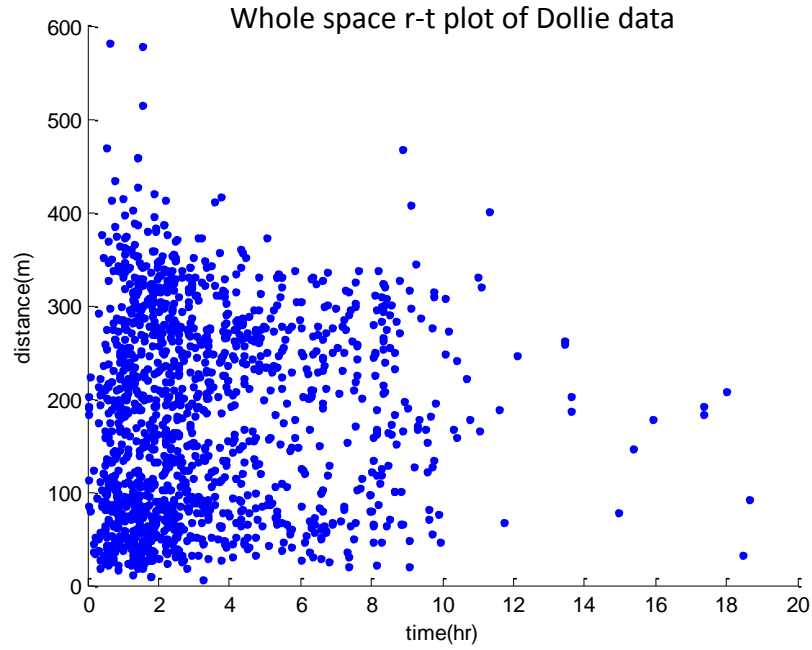


Figure 2-18 Whole space r-t plot of all located events.

However, this is quite different from the ideal point source diffusion model proposed by Shapiro *et al* (1997). In this case, we found some microseismic events were located far from the injection point in the early pumping stage; these results are shown in Figures 2-13, 2-14 and 2-18. We cannot tell the mechanism of these events only based on the result of microseismic event location. They may have been caused by the effect of high brittleness combining with in-situ stress distribution, or slurry fast diffusing along pre-existing fracture. The hypothesis we proposed for this effect is caused by the geometry of hydraulic fracture. We need to test it by using treating parameters, hydraulic fracture model, and mass conservation.

The treating pressure and cumulative slurry volume, are shown in Figure 2-19. The treating pressure and cumulative slurry volume during the fracturing

operation can be seen in the blue and green curve, respectively. Figure 2-19 shows treating pressure dropped dramatically 20 minutes after injection started which indicates a hydraulic fracture was generated (Gregory, 2011). Around 30 minutes after injection started, treating pressure increased back to around 3000 psi and kept at that level, which means the newly-generated space was filled with slurry and then fluid diffusion started to play a major role. We found the cumulative injected slurry volume to be around 231m^3 when treating pressure increased back to 3000psi.

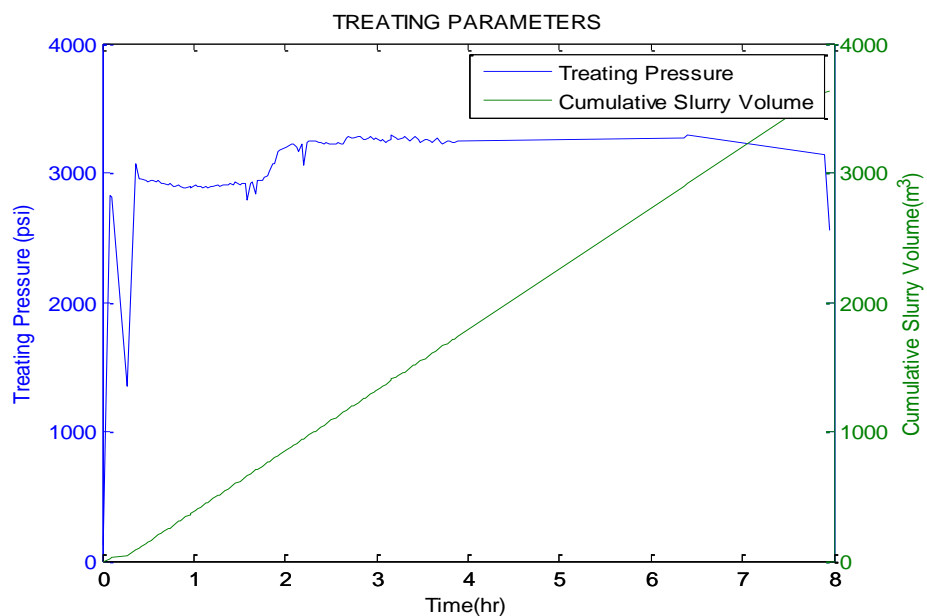


Figure 2-19 Recorded treating parameters evolve with time. The blue line represents the treating pressure. The green line represents the cumulative slurry volume pumped in.

Now we consider the geometry of hydraulic fracture and mass conservation. Because of low porosity and permeability, a shale formation is not good at storing or transporting fluid in its matrix. At the early stage of pumping, the slurry played a

major role in opening new fractures and diffusion phenomena were assumed to be negligible. Thus, we assume the volume of slurry equals the volume of generated fracture space during the early stage.

The height of the hydraulic fracture was around 75m, according to the cross-section view of location result, as shown in Figure 2-14. The width of the hydraulic fracture was around 4mm, which is close to the grain size of proppant. Figure 2-19 shows the cumulative slurry volume was 231m^3 . According to the volume conservation of incompressible fluid, the calculated one-wing length of the hydraulic fracture was around 350m. This result is consistent with the map view location result, as shown in Figure 2-13.

Also, this hypothesis was tested after we divide the whole space into directional sectors. If these early long-distance events were induced by fracture opening, they should also show up in the sector which extends along the assumed predominant fracturing direction.

Now we could estimate diffusivity according to the whole space spatial-temporal distribution of located microseismic events as well as permeability before and after hydraulic fracturing. The plot is shown in Figure 2-20. The red curve starts at 30 minutes and 350m from the r-t plot and covers 95% of the events during injection. The diffusivity corresponding to the red curve was $1.2 \times 10^{-3} \text{m}^2/\text{s}$. The corresponding diffusivity after hydraulic fracturing equalled $3.75 \times 10^{-2} \text{m}^2/\text{s}$, which is characterized by the blue curve.

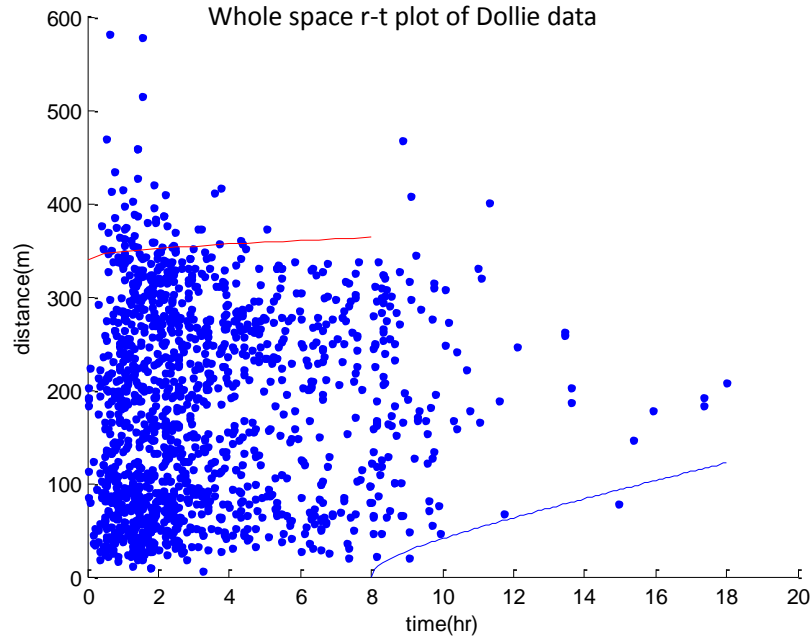


Figure 2-20 Whole space r-t plot. The red line characterizes diffusion after the fracture opening. The blue line starts at 8 hours after injection started and characterized the fluid flow back after injection stopped.

In the paper of Shapiro *et al.* (1997), the point source model is acceptable and the geometry of the hydraulic fracture is negligible because the geometrical size of the hydraulic fracture compared with the monitoring scale in space is small enough. However, the monitoring duration of the microseismic survey we conducted only lasted for 21 hours and the long-distance events located at the early stage were induced by a fracture opening. In order to this uncertainty, we considered the geometrical size of hydraulic fracture and calculated the length of the hydraulic fracture.

The end of the hydraulic fracture wing was considered as the diffusion

starting point after the hydraulic fracture was generated. By use of formation porosity, dynamic viscosity, and diffusivity values, we were able to calculate permeability before and after hydraulic fracturing according to the permeability expression as shown in Equation 2-14. In this case, the permeabilities before and after hydraulic fracturing were 7.7×10^{-5} and 4.02×10^{-3} Darcy, respectively.

Though we considered the geometry effect of the hydraulic fracture, the whole space r-t plot shown in Figure 2-20 still introduces uncertainties. First, distance is scalar in the r-t plot and it does not contain direction information. Thus, adjacent points in the r-t plot could be far away from each other in real 3-D space. Besides, for a point source model, if the diffusion is anisotropic, the events induced along the preferred diffusion orientation would overwhelm the events induced in other directions. That is why Figure 2-20 only characterizes the diffusivity along the preferred diffusion orientation.

It is necessary to calculate directional diffusivity to reduce uncertainty. The tensor form of the diffusivity expression is

$$r = \sqrt{\frac{4\pi t}{\mathbf{n}^T \mathbf{D}^{-1} \mathbf{n}}} \quad (\text{Shapiro } et al., 1999);$$

this works also for a single point diffusion model. Our study differs in two ways. First, in our case, we have two injection points. Second, the monitoring scale is not large enough in space and time, thus the geometrical size of the hydraulic fracture affect the permeability estimation. These two reasons made permeability tensor estimation

impossible by using single-point source diffusion method. However, we could extract permeability components along and perpendicular to the dominant fracturing direction.

We set the injection point as the origin and divided the whole stimulated rock volume into directional sectors according to azimuth and dip angles. The azimuth and the dip angles were defined to be between 0° and 360° and between -90° and 90° , respectively. We defined the direction along the N45 E as 0° azimuth. The half space above the injection point had a positive dip angle. We examined two sectors in detail; one is along the dominant fracturing direction, the other is perpendicular to it.

Figure 2-21 shows the map view of the sector corresponding to the dominant fracturing direction. Both azimuth and dip angles are in the range of -22.5° to 22.5° .

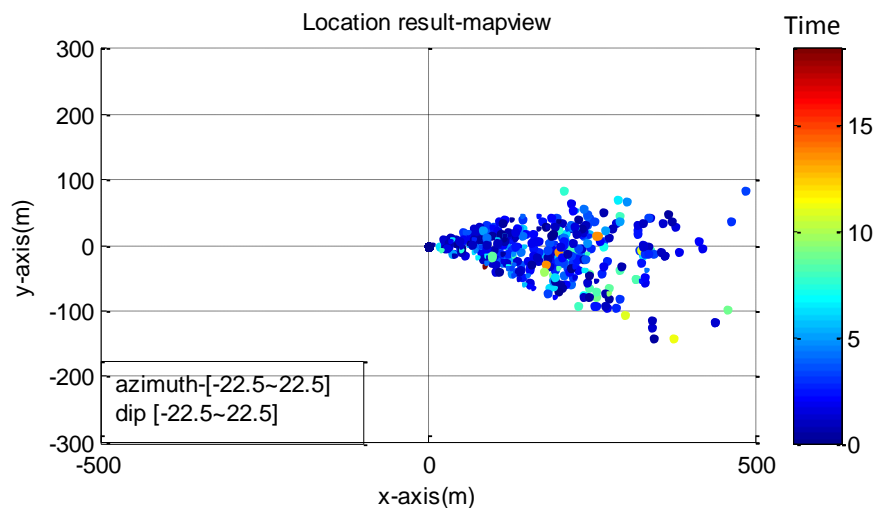


Figure 2-21 Map view location result of the sector with $(-22.5 \sim 22.5)$ azimuth and $(-22.5 \sim 22.5)$ dip

In this sector, we could see the early long-distance events. This is consistent with our hypothesis. By using our hydraulic fracture model and mass conservation, the diffusion procedure was considered to start at the end of the hydraulic fracture, which was 350m from the injection point. The curves which characterize the diffusivities before and after hydraulic fracturing are shown in the r-t plot in Figure 2-22; their values are $2.48 \times 10^{-3} m^2 / s$ and $0.188 m^2 / s$. The corresponding permeability values before and after hydraulic fracturing in this sector were 0.16 milliDarcy and 12.1 milliDarcy.

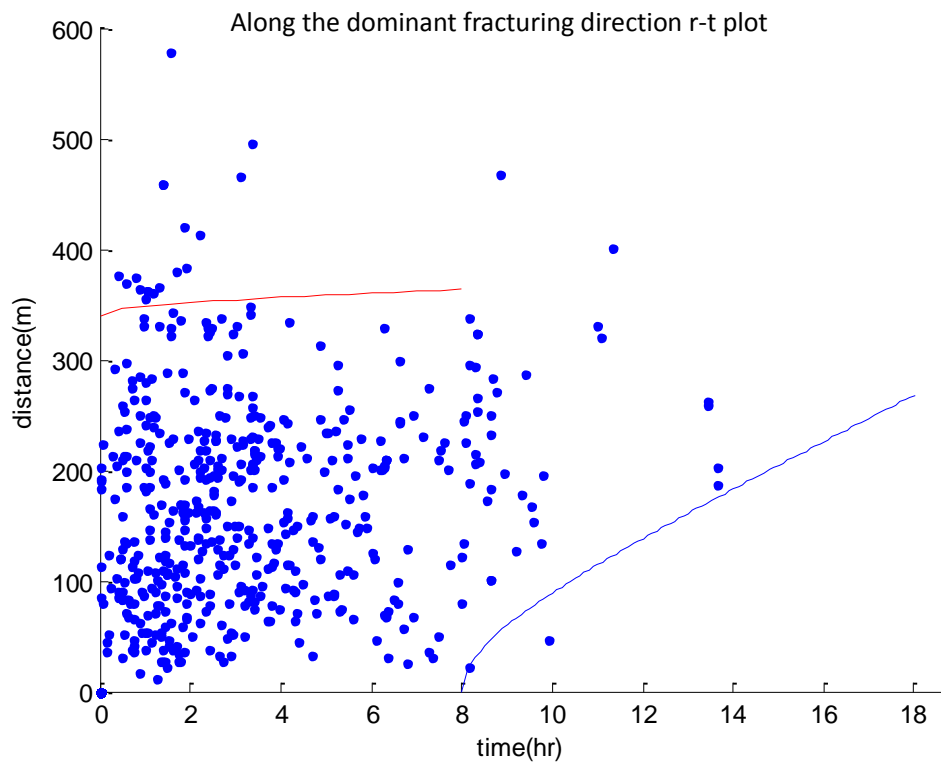


Figure 2-22 r-t plot corresponds to the same sector as in Figure 2-21

The second sector which is perpendicular to the dominant fracturing direction that we selected has azimuth ranges from 67.5° to 112.5° , and dip ranges from -22.5° to 22.5° . Figure 2-23 shows the map view location result of this sector. In this sector, the diffusion procedure was considered to start at the injection point. This is because the structure normal to the dominant fracturing direction was not changed very much according to hydraulic fracture model.

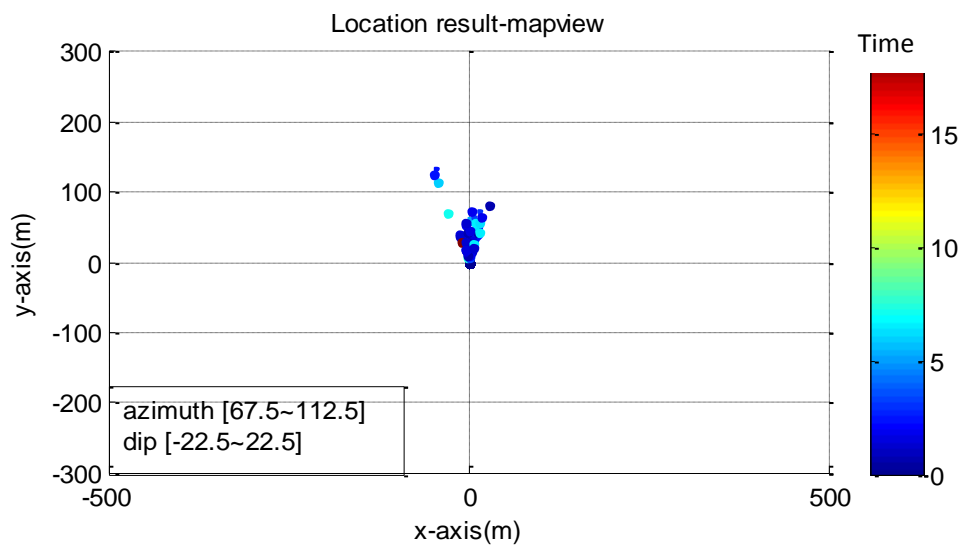


Figure 2-23 Map view location result of the sector which has (67.5° ~ 112.5°) azimuth, and (-22.5° ~ 22.5°) dip

The corresponding r-t plot of the sector normal to the dominant fracturing direction is shown in Figure 2-24.

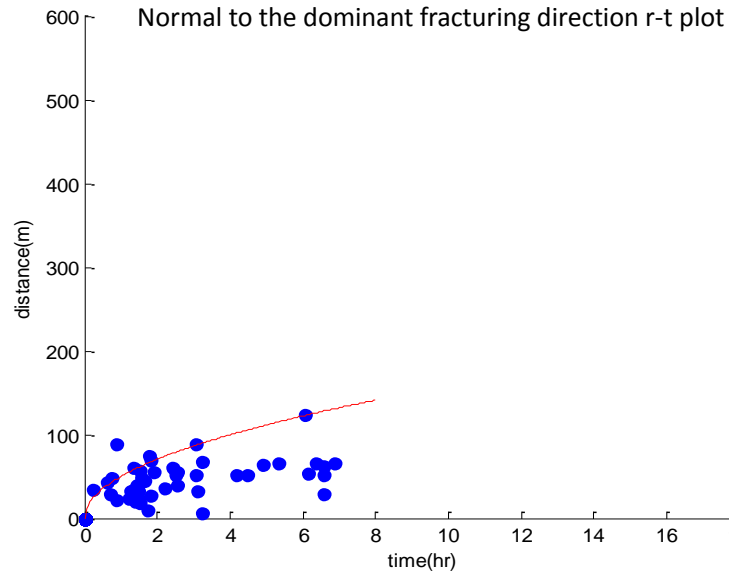


Figure 2-24 r-t plot of the sector with (67.5 °~112.5 °) azimuth, and (-22.5 °~22.5 °) dip

For this sector, the diffusivity and permeability before hydraulic fracturing were $0.05\text{m}^2/\text{s}$ and $3.21 \times 10^{-3}\text{Darcy}$. However, the diffusivity or permeability after hydraulic fracturing could not be obtained in this directional sector, for two reasons. First, according to our observations, there was only one located event after pumping. The uncertainty of estimated diffusivity result would be huge. Second, this direction was normal to the preferred fracture growth orientation, i.e., the formation along this direction was not changed before and after fracturing operation.

2.6 Summary and discussion

2.6.1 Summary

In this chapter, the 3-D diffusion equation has been interpreted from a probability perspective. Diffusivity, which carries the physical meaning of diffusion, has been interpreted as the probability density of a perturbation distributed in time and space. For a group of hydraulic diffusing particles, the root-mean-square average diffusing distance describes the fluctuation of diffusing particles in time and space, expressed as $r_{rms} = \sqrt{6Dt}$. In all, diffusing distance equals the square root of the product of diffusivity multiply, elapsed time, and a constant. With different criteria, the constant could be modified. For example, the curve fit the outermost events in r-t plots and gave the upper-limit diffusivity of the original formation. Its expression is $D = r^2 / 4\pi t$. Similarly, diffusivity of the formation after hydraulic fracturing was obtained by the curve fitting innermost located events induced by fluid flow after injection stopped.

For incompressible fluid, the diffusivity tensor was found to be equal to the permeability tensor divided by a scalar which was the product of dynamic viscosity, connected porosity, and formation compressibility under an isothermal condition.

Microseismic data acquired in the Barnett Shale Formation yielded, with assumed hydraulic geometry, an initial permeability of 0.16 and 3.21 milliDarcy in the assumed dominant of fracturing and normal to it, with an increase to 12.1

milliDarcy along the dominant direction of fracturing after the hydraulic fracturing, i.e., an increase the permeability along the assumed dominant fracturing direction by two orders of magnitude. The determination of permeability before hydraulic fracturing using the Dollie data is consistent with core sample measurement results done in the laboratory.

2.6.2 Discussion

Outermost diffusion-induced microseismic events in spatial-temporal distribution were used for estimating the diffusivity of the original formation because the medium had not been changed by earlier located events. Similarly, the diffusivity after hydraulic fracturing was able to be extracted by using innermost diffusion-induced events in spatial-temporal distribution. The diffusivities determined in this way were the upper-limit values. High diffusivity means fluid can transport at a high rate, and vice versa.

The uncertainties of permeability estimation based on the diffusion method may have come from the following:

(1) Accuracy of microseismic event location results

Accuracy of event locations is difficult to verify, because we do not know the exact coordinates of each event, except at perforation points. Besides, only a small portion of microseismic events in the time-space plot was used for

estimating the permeability of the medium before and after hydraulic fracturing. Thus, the accuracy of the permeability estimation results depends highly on the location results of those events. Very few microseismic events were located after pumping, which also introduces uncertainty for the permeability estimation of the medium after hydraulic fracturing. Reducing the locatable threshold of the microseismic events location method would be helpful for permeability estimation.

(2) Time and space scale of monitoring

Permeability tensor estimation based on the diffusion method worked for the single point source model. For the hydraulic fracturing case, it is approximately valid if the time and space scale of monitoring is large enough compared with the geometry of the hydraulic fracture.

(3) Assumed hydraulic fracture geometry

The end of the hydraulic fracture wing was considered as the point source for diffusion along a dominant fracturing direction. An inaccurate length for the hydraulic fracture could induce errors up to one order of magnitude for permeability estimations of the original medium along the dominant fracturing direction. This is because, compared to the permeability values of shale formation, a several-meter difference in diffusing distance would make a huge difference for the estimated permeability.

(4) Unclear mechanism of microseismic events and assumed diffusion-induced

events

A located microseismic event only means the medium has been changed at those coordinates, i.e., (x, y, z, t) . However, it does not necessarily mean the fluid reached this point. It may have been induced by the effect of in-situ stress distribution and the brittleness of the medium combined. On the other hand, fluid flow would not necessarily be inducing microseismic events; for example, water could flow quietly in a pipe or pre-existing fractures. A hydraulic fracture model is important to reduce the uncertainty that comes from the ambiguous relationship between ‘fracture’ and ‘flow’, especially when the time and space scale of monitoring is limited.

The permeability tensor could not be fully extracted from the Dollie data case. The first reason is that two pumping points along the vertical well made the diffusion-induced events overlap. Second, because the monitoring scale in time and space was not large enough, hydraulic fracture geometry had to be taken into account. However, we were unable to accurately determine the origins of diffusion-induced events which were located not normal to the dominant direction of fracturing.

Accurately locating microseismic events was our first priority. With the location results we could give the spatial-temporal distribution of microseismic and calculate the SRV. However, we did not have 100% accuracy answer about the real coordinates of each microseismic event in real situations.

Here I list several aspects that may have introduced errors and uncertainties to microseismic event location results and some recommendations for future work.

Generally, the accuracy of location depends on (Abaseyev, *et.al*, 2009):

- (1) Geometry of observation;
- (2) Velocity model;
- (3) Types of the waves used for interpret data;
- (4) Accuracy of P- and S-wave time arrival determination;
- (5) geophone component orientations.

Among these, the velocity model is important for both arrival picking-based methods and migration-based methods. The velocity model changes dynamically because the purpose of hydraulic fracturing is to change the subsurface structure, which definitely changes transport and elastic properties as well. Figures 2-25 and 2-26 present seismograms recorded by the same station responding to different perfs. The first example in Figure 2-25 shows that the correlation of recorded seismograms was high because these two perfs are close in time. The second example in Figure 2-26 shows that the correlation of recorded seismogram was low due to the long time gap. These imply the velocity model was changing dramatically during hydraulic fracturing.

Further, not all detectable microseismic events can be located, i.e., each algorithm has a locatable threshold. For the UHFracDetect, it can locate microseismic events with a signal-noise ratio higher than 1.3. This means that some weak events,

for example, back flow induced events, cannot be located. Recently, migration-based location methods were able to locate microseismic events with a signal-noise ratio as low as 0.5 (Gajewski and Tessmer, 2005). Due to its high computational cost, this type of method is still less popular in the oil and gas industry. Thus, in the future it is necessary to reduce the threshold of location and the computational cost.

Diffusion methods estimate the upper-limit diffusivity of the original formation by using outermost events in r - t plots, and estimate upper-limit formation diffusivity after hydraulic fracturing by using innermost events in r - t plots. In this way, uncertainties definitely depend on the accuracy of outermost and innermost events in r - t plots. However, located events between these did change the formation structure but did not contribute to the diffusivity estimation. Even worse, we may not have located events induced by flow back if monitoring stopped immediately when pumping stop. Thus, in the next chapter we consider a way to make use of all located events during pumping and simulate the fluid flow in the fracture system.

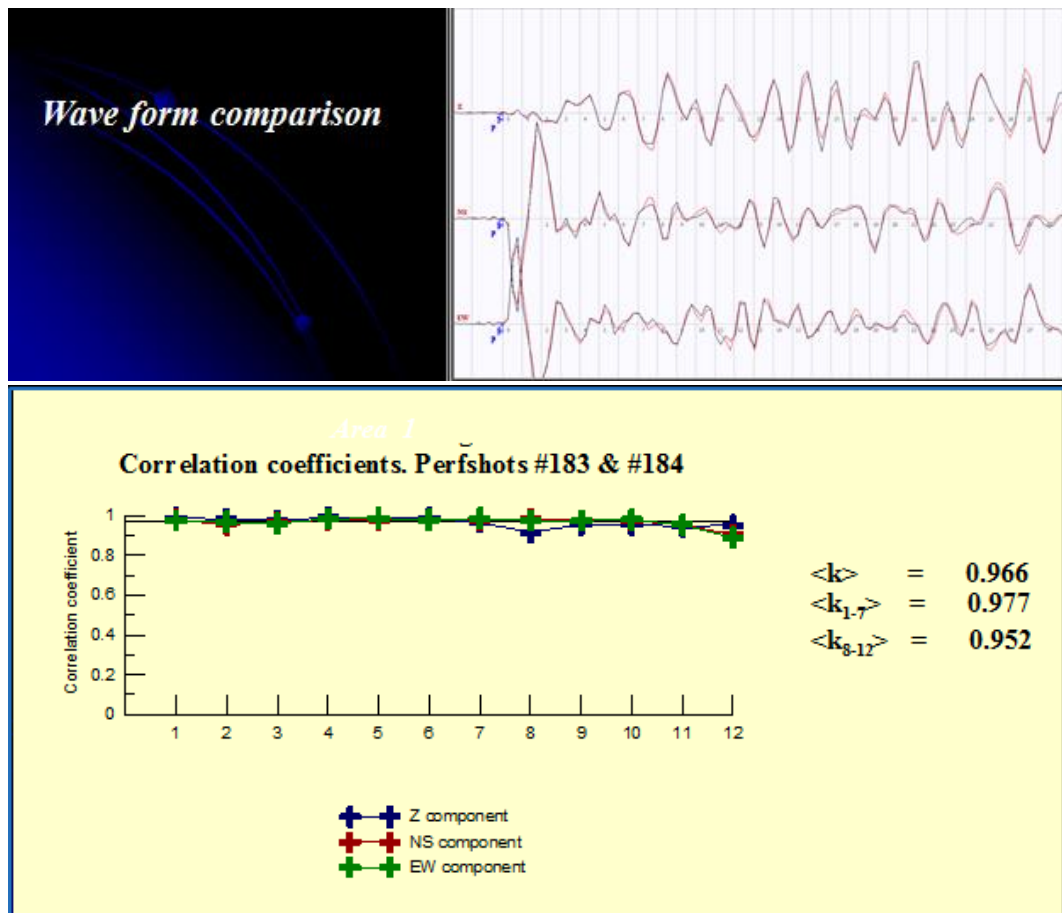


Figure 2-25 Two perfshots taken from Dollie well. The distance between these two perfshots is 40 ft. The time difference between these two perfshots is 71 seconds. The recorded seismograms by the same station have high correlation coefficients values. (Evgeny Chesnokov, “Microseismics: Integrated, Advanced Geophysics”, class lecture, Microseismic, Natural Sciences and Mathematics, Houston, TX, Aug 27, 2012).

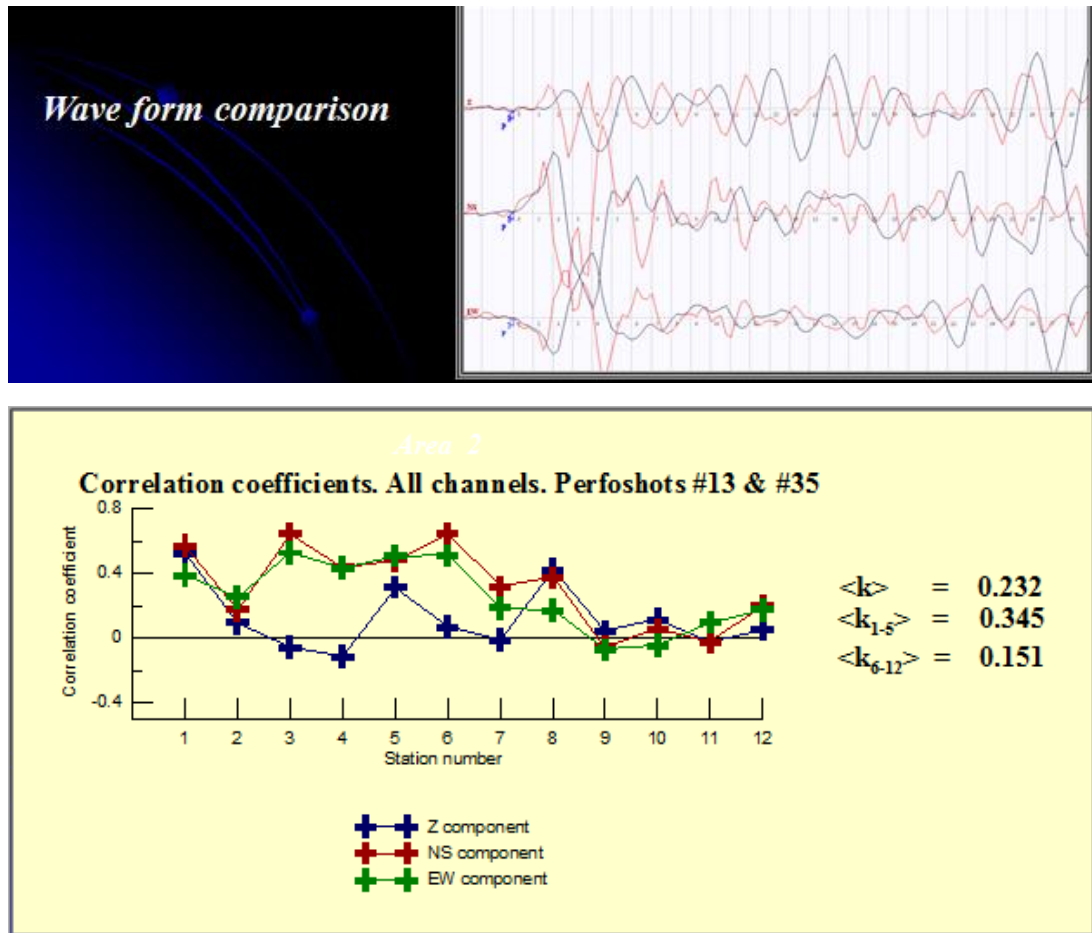


Figure 2-26 Two Perfshots taken from Dollie well. The distance between these two perfshots is 40 ft. The time difference between these two perfshots is 2 days and 23 hours. The recorded seismograms by the same station have low correlation coefficients values. (Evgeny Chesnokov, "Microseismics: Integrated, Advanced Geophysics", class lecture, Microseismic, Natural Sciences and Mathematics, Houston, TX, Aug 27, 2012).

Chapter 3 Fluid flow simulation

3.1 Introduction

The moment tensor solution and analysis of microseismic magnitude could provide the orientation and geometrical size of each fracture. Combining the locations of microseismic events, the fracture networks could theoretically be built. With the help of operating parameters such as pumping pressure, and slurry viscosity, fluid flow in the fracture networks could be simulated based on the Navier-Stokes equation. Flow flux and permeability could also be calculated.

Different from diffusion methods, permeability can be only obtained by fluid flow simulation for known flow domains using numerical methods. Fluid flow simulation is considered to be an extension of microseismic monitoring techniques; thus it was able to help us calculate the production rate or permeability using the following:

- (1) Flow domain information; for example, length, width, and shape of flow domain;
- (2) Fluid information; for example, viscosity, density;
- (3) In-situ parameters; for example, pressure gradient or inlet velocity.

We also wanted to investigate angular-dependent and scale-dependent effects on synthetic media by our implementing fluid flow simulation.

In this chapter, we first briefly introduce the basic theory of fluid dynamics and numerical methods. After that, we simulate the fluid flow in a rectangular channel

using the finite difference method. We also simulate fluid flow in a periodic geometry channel using the finite element method. Rectangular and periodic flow domains are selected for simulation because they represent the shapes of hydraulic fractures with uniformly (ideal) and non-uniformly (non-ideal) distributed proppants in hydraulic fractures. Rectangular and periodic geometry flow domains can be seen as the basic elements out of which real hydraulic fractures are made. We also simulate fluid flow in synthetic shale core samples which have flow directions of 0° , 15° , 30° , 45° , 60° , and 75° angles to bedding planes. Then, we simulate the fluid flow in the fracture with the same width and orientation but with different sizes of synthetic media. With the help of simulation, we were able to calculate effective permeability of corresponding synthetic media.

3.2 Numerical methods and the Navier-Stokes equation

As in investigating other problems, analytical solutions are best, and have many benefits, such as being continuous, accurate, and fast for computation. However, analytical solutions do not always exist. As a non-linear partial differential equation, no analytical solution exists for the general form of the Navier-Stokes equation. However, numerical solutions exist for almost all cases. Compared with results obtained by experiments, numerical methods are inexpensive, visible, and have controllable computation accuracy. Numerical simulation of fluid flow is widely used in the fields of aerospace, automobile, and biomedical, but it is still new for reservoir

monitoring.

Numerical methods could provide solutions in a discrete form for each grid point. Thus, we needed to discretize the domain, i.e., divide the domain into numbers of discrete sub-domains, where each sub-domain is represented by a discrete set of points. The purpose of discretization is to obtain lower order polynomial functions. Then the continuous governing differential equation was able to be converted into a system of algebraic equations. After that we could obtain values of dependent variables at discrete points.

Newton's laws are inherently suitable for Lagrangian description. We could write an equation of motion and focus on the locations of each particle with the help of Newton's law. In fluid mechanics, it is more convenient to use Eulerian description, which is a way of focusing on specific volume fixed in space. This specific volume is called control volume. Fluid can freely flow through its boundaries as time passes. A mass or momentum balance equation can be written for the control volume. The difficulty is the basic equations given by Newton's law of motion are not inherently developed for control volume. Thus, the transformation from Lagrangian to Eulerian description is necessary. Reynolds transport theorem is involved. Details of the Reynolds transport theorem are shown in Appendix.

The momentum balance equation for undeformable and stationary control volume is expressed in Equation 3-1, as

$$\sum F_{cv} = \int_{cv} \frac{\partial}{\partial t} (\rho \vec{v}) dV + \int_{cs} (\rho \vec{v})(\vec{v} \cdot \vec{\eta}) dA, \quad (3-1)$$

where ρ is the density of fluid, \vec{v} is the velocity of fluid, $\vec{\eta}$ is the normal vector of the control surface, and $\sum F_{cv}$ is the effective forces applied to the control volume.

After analyzing the stress-strain relation with the help of viscosity parameters λ and μ , we can obtain the Navier-Stokes equation for homogenous and isotropic Newtonian fluid. The conservative form of the Navier-Stokes equation is

$$\frac{\partial}{\partial t} (\rho u_i) + \frac{\partial}{\partial x_j} (\rho u_i u_j) = -\frac{\partial P}{\partial x_i} + \frac{\partial}{\partial x_j} \left(\mu \frac{\partial u_i}{\partial x_j} \right) + \frac{\partial}{\partial x_i} \left[(\lambda + \mu) \frac{\partial u_k}{\partial x_k} \right] + \rho b_i, \quad (3-2)$$

where i, j , and k represent three axes of Cartesian coordinates, and μ and λ are the viscosity coefficient and 2nd viscosity coefficient, respectively. On the right-hand side of the equation, the first term is interpreted as a pressure gradient term; the second term is a viscous term; the third is a volumetric dilation term, which equals to zero if incompressible fluid; and the last term represents the body force.

For the left-hand side, after expanding the derivative, we obtain

$$\rho \frac{\partial u_i}{\partial t} + u_i \frac{\partial \rho}{\partial t} + u_i \frac{\partial (\rho u_j)}{\partial x_j} + \rho u_j \frac{\partial u_i}{\partial x_j}.$$

The sum of the second and third terms equals to zero according to mass conservation.

Thus, the left-hand side is $\rho \left(\frac{\partial u_i}{\partial t} + u_j \frac{\partial u_i}{\partial x_j} \right) = \rho \frac{Du_i}{Dt}$. If $\rho \frac{Du_i}{Dt}$ or

$\rho \left(\frac{\partial u_i}{\partial t} + u_j \frac{\partial u_i}{\partial x_j} \right)$ is used on the left-hand side of the Equation 3-2, we obtain the

non-conservative Navier-Stokes expression. ρ is not necessary to be a constant even

if it is out of the derivative symbol.

For 3-D cases ($i=1,2,3$), we have three momentum equations. However, there are four unknowns, i.e., u_1 , u_2 , u_3 , and P . That is why the mass conservation equation has to be involved, though the mass conservation equation explicitly does not contain a pressure term. The challenge of fluid flow simulation is to solve equations numerically, where P is unknown, and we do not have an explicit governing equation.

3.3 Finite difference method and flow simulation in simple geometry domain

In this section, we simulate fluid flow in a simple geometry domain, i.e., a rectangular domain. We will briefly introduce the principle of the numerical method, boundary conditions and initial conditions, and then show the simulation results.

3.3.1 Finite difference method

The finite difference method is one of the oldest numerical methods. It was proposed by L.F. Richardson (1911). It expresses the derivatives in terms of suitable algebraic differences using the Taylor series expansion. Usually, we keep the first-order derivative term and truncate higher order terms. If we set the step-length to

be h , the truncation error of the first-order derivative using forward or backward difference is proportional to h ; the truncation error of the first-order derivative using center difference is proportional to h^2 ; the truncation error of the second-order derivative using center difference is also proportional to h^2 . If the value of step length h is small, h^2 is assumed to be insignificant.

According to the Taylor series, however, the forward difference expression is
$$f(x+h) = f(x) + hf'(x) + \frac{h^2}{2} f''(x) \dots \quad (3-3)$$

If we keep the first two terms on the right-hand side of the expression and assume the value of h is small, the truncation error could also be significant because $f''(x)$ is not necessarily small. Thus, we need to evaluate the higher order derivatives and make sure the truncation error is tolerated.

The advantage of the finite difference method is its simplicity for expressing the derivative form of a differential equation by Taylor series expansion. Except for the possible truncation error problem just mentioned, the disadvantage of the finite difference method is that it requires grid lines orientated in a mutually orthogonal manner. Thus, for complicated geometry domains, the finite difference method is not the first choice.

3.3.2 Flow simulation in simple geometry domain

For compressible flow, pressure is linked to density. However, the pumping

slurry is made of sands and liquid solutions, we assume it is incompressible. In this section, we simulate 2-D, incompressible flow in a rectangular domain till it reaches steady state. Steady flow means the properties of the flow are not a function of time, i.e., $\frac{\partial}{\partial t} c = 0$,

where c represents any property of the flow. For incompressible fluid, density is a given property of the fluid itself, not a function of pressure.

The conservative form of the Navier-Stokes equation is

$$\frac{\partial}{\partial t}(\rho u_i) + \frac{\partial}{\partial x_j}(\rho u_i u_j) = -\frac{\partial P}{\partial x_i} + \frac{\partial}{\partial x_j}(\mu \frac{\partial u_i}{\partial x_j}) + \frac{\partial}{\partial x_i}[(\lambda + \mu) \frac{\partial u_k}{\partial x_k}] + \rho b_i. \quad (3-4)$$

Specifically, the x-momentum equation is:

$$\frac{\partial(\rho u)}{\partial t} + \frac{\partial(\rho u^2)}{\partial x} + \frac{\partial(\rho uv)}{\partial y} = -\frac{\partial P}{\partial x} + \frac{\partial}{\partial x}(\lambda \nabla \cdot \vec{V} + 2\mu \frac{\partial u}{\partial x}) + \frac{\partial}{\partial y}[\mu(\frac{\partial v}{\partial x} + \frac{\partial u}{\partial y})] + \rho b_i, \quad (3-5)$$

where u and v are velocity along the x and y directions, respectively; ρ is the density of fluid, λ and μ are viscosity coefficient and 2nd viscosity coefficient, and P is pressure.

Due to incompressible, steady flow simulation, the original Navier-Stokes equation is

$$\rho(\frac{\partial u_i}{\partial t} + u_j \frac{\partial u_i}{\partial x_j}) = -\frac{\partial P}{\partial x_i} + \frac{\partial}{\partial x_j}(\mu \frac{\partial u_i}{\partial x_j}), \quad (3-6)$$

where body force term is cancelled because of buoyance force.

As a variable, pressure appears in gradient form instead of in its absolute sense. When we evaluate a local derivative at a particular point, it will bring us difficulty if pressure gradient and velocity are evaluated at the same point, as shown

in Figure 3-1.

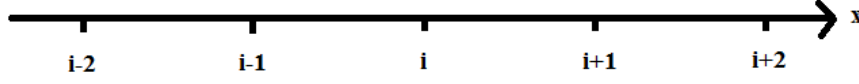


Figure 3-1 Velocity u is evaluated at points $i-1, i, i+1, i+2$

For example, we obtain a simplified momentum equation as

$$\frac{\partial u}{\partial t} = -\frac{\partial P}{\partial x_i}, \quad (3-7)$$

where u represents the velocity and P represents pressure. If we rewrite it in discrete

$$\text{form, we obtain } \frac{u_i^{n+1} - u_i^n}{\Delta t} = -\frac{P_{i+1} - P_{i-1}}{2\Delta x}. \quad (3-8)$$

We can see the pressure at this particular point i does not show up in the momentum equation at point i because of the pressure gradient used. In order to avoid this, pressure and velocity should be evaluated at alternate points, as shown in Figure 3-2. We set up the staggered grid and derived the discretized momentum equation in a simple geometry domain.

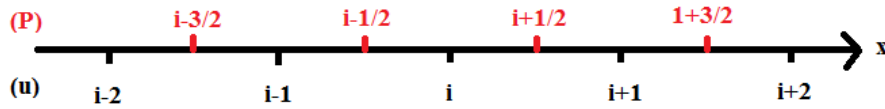


Figure 3-2 Points of pressure are evaluated in between the evaluated points of velocity, i.e., pressure is evaluated at the red color points.

Figure 3-3 presents a 2-D staggered grid as an example.

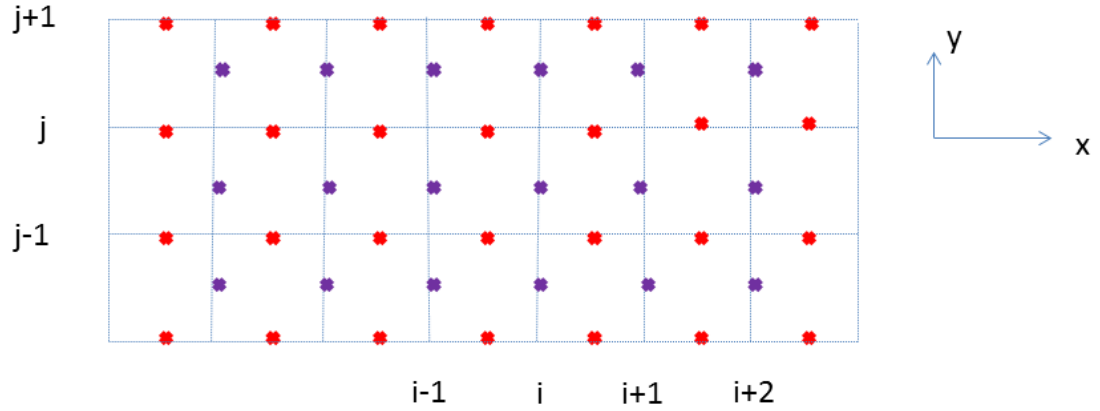


Figure 3-3 Two dimensional staggered grid

Velocity along the x-axis is evaluated at each red point and represented by u ; velocity along the y-axis is evaluated at each purple point and represented by v . Pressure is evaluated at each intersection point of the blue lines. In 2-D cases, three quantities, u , v , and p , are not evaluated at the same point (i, j) , i.e., velocity u with respect to pressure P is evaluated at the same grid along y , but at the half-grid point along the x direction. Similarly, velocity v is evaluated with respect to P at the same x but at the half-grid point along the y direction.

We arbitrarily selected a control volume which is extending one half-grid in each direction, as shown in Figure 3-4. Pressure P is at the center of the control volume. Each control volume has four faces; we defined the east, west, north, and south faces as e , w , n , and s , respectively. We defined the nearest east, west, north, and south grid points as E , W , N , and S , respectively.

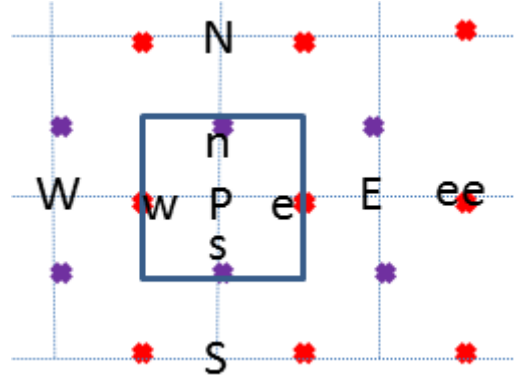


Figure 3-4 Control volume and its four faces

Next, we gave the discretized momentum and continuity equations of two-dimensional, incompressible, steady flow.

The continuity equation in continuous form was expressed as

$$\frac{\partial u}{\partial x} + \frac{\partial v}{\partial y} = 0. \quad (3-9)$$

Its discretized form was expressed as

$$\frac{u_e - u_w}{\Delta x} + \frac{v_n - v_s}{\Delta y} = 0, \quad (3-10)$$

where e, w, n, and s represent east, west, north, and south faces of the control volume.

Due to steady flow, the momentum equation along the x axis in continuous form at face e is

$$\frac{\partial}{\partial x}(u^2) + \frac{\partial}{\partial y}(uv) = -\frac{1}{\rho} \frac{\partial P}{\partial x} + \mu \left(\frac{\partial^2 u}{\partial x^2} + \frac{\partial^2 u}{\partial y^2} \right); \quad (3-11)$$

its discretized form is

$$\frac{u_e^2 - u_w^2}{\Delta x} + \frac{uv_n - uv_s}{\Delta y} = -\frac{1}{\rho} \frac{P_E - P_P}{\Delta x} + \mu \left(\frac{u_{ee} - 2u_e - u_w}{\Delta x^2} \right). \quad (3-12)$$

Similarly, we could obtain momentum equation along the y axis.

In this way, we reorganized the expression and obtained x-momentum in the form of a linearized matrix equation at each point e for the whole domain:

$$A_e u_e + \sum A_{nb} u_{nb} = -\frac{1}{\rho} \frac{P_E - P_P}{\Delta x}; \quad (3-13)$$

and a y-momentum linearized matrix equation at point n for the whole domain:

$$A_n v_n + \sum A_{nb} v_{nb} = -\frac{1}{\rho} \frac{P_N - P_P}{\Delta y}, \quad (3-14)$$

where subscript nb represents contributions from neighboring points.

Now we have three equations (continuity, x-momentum, and y-momentum equations) we need to solve and obtain values of u_e , v_n , and P_P . The principle is we assume pressure at every point first, i.e., assume P_E , P_P , and P_N through the whole domain, and obtain

$$A_e u_e + \sum A_{nb} u_{nb} = -\frac{1}{\rho} \frac{P_E^* - P_P^*}{\Delta x} \text{ and } A_n v_n + \sum A_{nb} v_{nb} = -\frac{1}{\rho} \frac{P_N^* - P_P^*}{\Delta y}, \quad (3-15)$$

where the asterisk means the pressure values are assumed, the first terms on the left-hand side represent velocity variation due to pressure change, and the second terms on the left-hand side represent the contribution from neighboring grids' convective and diffusive flow.

Then we can solve the momentum equations and obtain the velocity fields u^* and v^* according to the assumed pressure field. If the assumed pressure field is correct, the corresponding velocity field would satisfy the continuity equation at every location. If the continuity equation is not satisfied, we need to make a correction to

the pressure field and repeat this procedure till the solved velocity field satisfies the continuity equation. During this procedure, we use the first-order degree approximation that pressure correction will not have significant change from the implicit neighboring contribution.

Now we implement boundary conditions. For second-order differential equations, usually there are three types of boundary conditions. The first one is the essential boundary condition, which is the variable for which variation appears if the boundary term is specified. The second one is the natural boundary condition, which is the coefficient of variation if the boundary term is specified. The last one is the mixed boundary condition.

The flow domain for this procedure is shown in Figure 3-5.

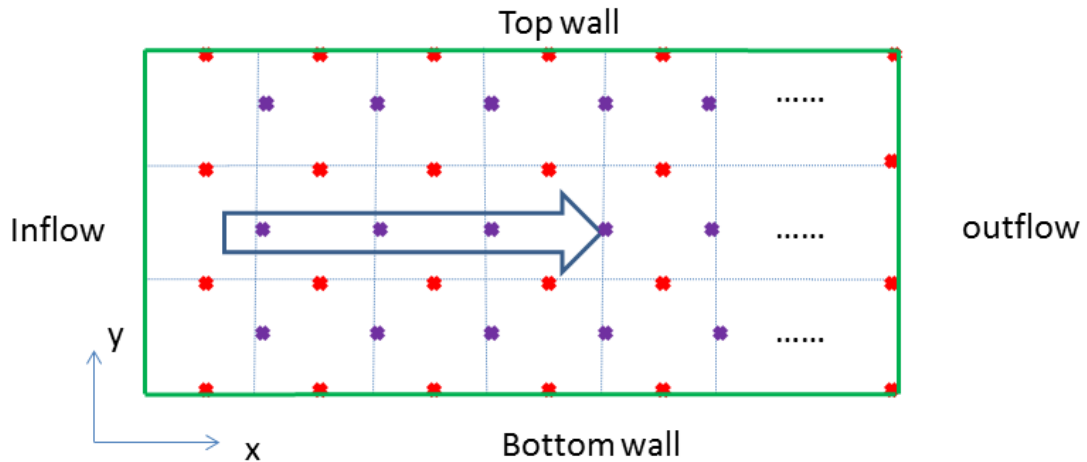


Figure 3-5 Schematic drawing of a two-dimensional domain with four boundaries

We simulated the laminar flow with the boundary conditions of this domain as follows:

We used u , v , and P to represent velocity along the x -axis, y -axis, and pressure, respectively. The boundary conditions of both top and bottom walls are: $dP/dx=0$, $u=v=0$. The boundary conditions of inflow are: $u=\text{constant}$, $v=0$; $dP/dx=0$. The boundary conditions of outflow are: $du/dx=dv/dy=0$, $P=0$.

The whole domain was discretized. Pressure, u -velocity, and v -velocity were evaluated at $m \times n$, $m \times (n-1)$, and $(m-1) \times n$ points, respectively. We implemented the boundary conditions in discretized form and used index i and j , which represent the coordinate of pressure grid points, where $i=1,2,3 \dots m$, $j=1,2,3 \dots n$.

The boundary conditions could be modified according to the different cases we investigate; for example, on the inflow side we could use an essential boundary condition, i.e., a specific pressure value.

The geophysical and computational parameters we used in simulation are shown in Table 1:

Density of fluid	1.5g/cm^3
Viscosity of fluid	$3 \times 10^{-5} \text{ Pa}\cdot\text{s}$
Inlet velocity	0.01m/s
Outlet pressure	0
Length of flow domain	0.02m
Width of flow domain	0.008m
Tolerated residual error for continuity equation	10^{-6}

Table 1 Simulation parameters used for the $0.02 \times 0.008\text{m}$ rectangular domain.

These parameters shown in Table 1 are directly from our Dollie data case, and the simulation based on those parameters is defined as Case 1.

Then we changed the one parameter at a time and observed the difference in each simulation result.

For Case 2: the density of fluid was changed to 1g/cm^3 .

For Case 3: the viscosity of fluid was changed to $3 \times 10^{-6} \text{ Pa}\cdot\text{s}$.

For Case 4: the inlet velocity was changed to 0.03m/s .

Figure 3-6 gives the simulation results for each case. The row number corresponds to the case number. For each case, the figure on the left column shows the horizontal velocity (u) in flow domain. The figure in the middle column shows the vertical velocity (v) in flow domain. The figure on the right column shows the pressure field in flow domain. The color bar gives the magnitude of each field.

Figure 3-6 shows that the velocity and pressure fields of each case when the fluid flow reached the steady state. For different cases, the flow domain size stayed the same, but the area of the zone influenced by the entrance effect was different. “Entrance effect” means the horizontal velocity is a function of the x -coordinate and vertical velocity is a function of the y -coordinate, i.e., the velocity field has not fully developed. Compared with whole flow domain size, the zones influenced by entrance effects cannot be negligible.

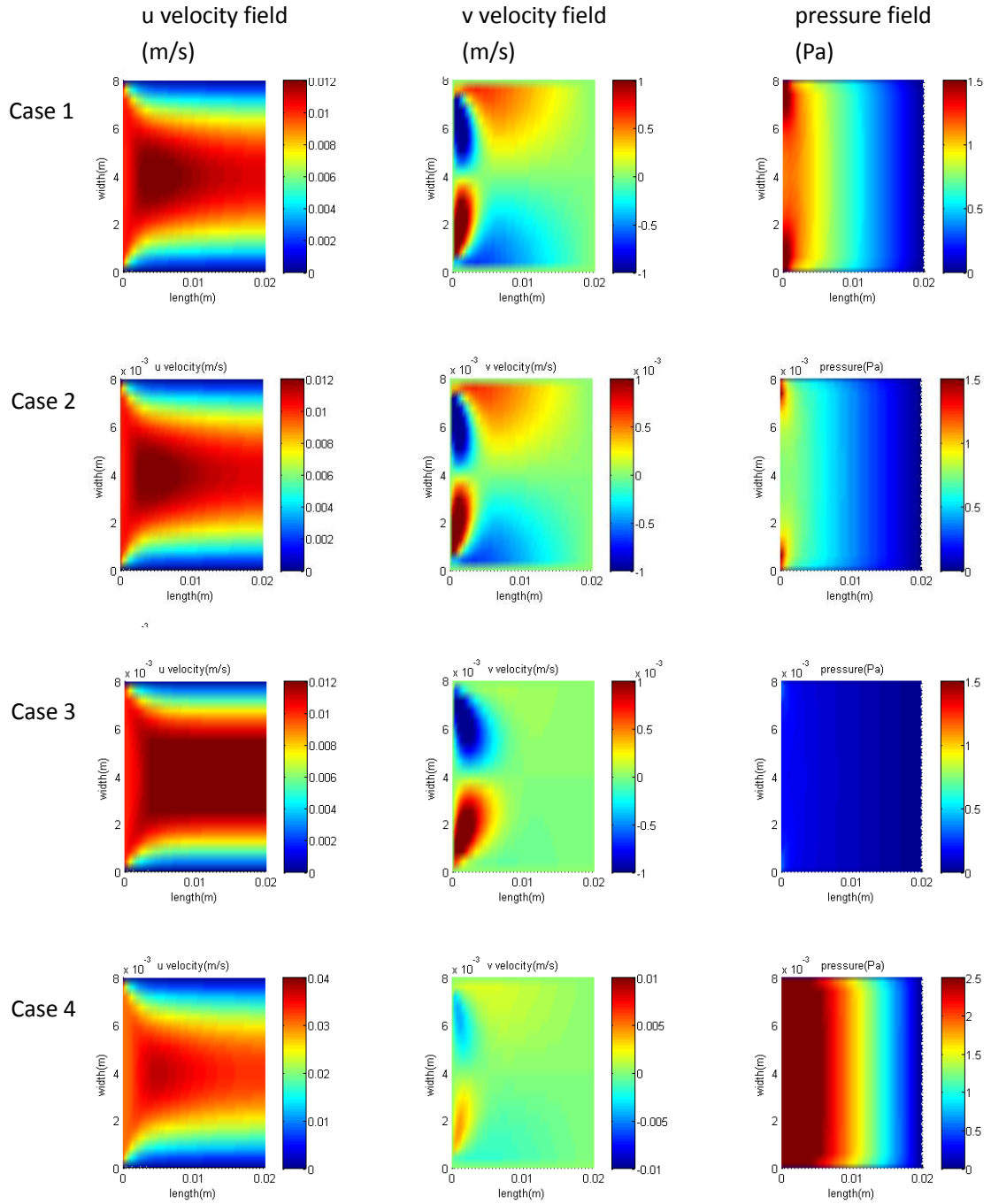


Figure 3-6 Simulation results of Cases 1, 2, 3, and 4

One-dimensional Darcy's law is expressed as

$$Q_x = \frac{A\kappa}{\eta} \frac{dP}{dx}. \quad (3-16)$$

After reorganizing, we obtain

$$\kappa = \frac{Q_x \times \eta}{A \times \nabla P}. \quad (3-17)$$

We were able to calculate permeability using this expression. Because the fluid is incompressible, has the same inlet velocity, same flow domain, and same mass conservation, the flux values are the same for Cases 1, 2, and 3. Their permeability ratio depends on the viscosity divided by pressure drop.

The only different parameter used in the simulation of Case 2 compared with Case 1, is the fluid density. Density was changed from 1.5 g/cm³ to 1 g/cm³. For both Case 1 and Case 2, flux is the same due to the same inlet velocity. Though density is implicit in Darcy's law, simulation results showed us the total pressure drop decreased. From Case 1 to Case 2, permeability increased.

The only different parameter used in the simulation of Case 3 compared with Case 1, is the fluid viscosity. Viscosity was changed from 3×10⁻⁵ Pa·s to 3×10⁻⁶ Pa·s. For both Case 1 and Case 3, the inlet velocity and flux are the same, respectively. Simulation results showed that the total pressure drop decreased dramatically, i.e., the total pressure drop in Case 3 was less than one tenths of the total pressure drop in Case 1. From Case 1 to Case 3, permeability increased.

The only different parameter used in the simulation of Case 4 compared

with Case 1, is the inlet velocity. The inlet velocity was changed from 0.01 m/s to 0.03 m/s. Thus, the flux of Case 4 is three times larger than the flux of Case 1. According to simulation results, the pressure drop increased. The ratio of pressure drop in Case 4 to that in Case 1 was smaller than three. From Case 1 to Case 4, permeability increased.

Based on simulation results, we can make several conclusions. Firstly, for the same flow domain, when the zone under the entrance effect is not negligible, the calculated permeability is a non-linear function of flux, pressure drop, and viscosity. Also, flux and pressure drop are inter-dependent. There is no explicit expression between them, even if the same type of fluid (compare Case 1 with Case 4) was used. The reason behind this phenomenon is that the Navier-Stokes equation is a non-linear partial differential equation and no analytical solution exists.

If we keep the same boundary conditions and change the type of fluid, i.e., density and/or viscosity (compare Case 1 with Case 2; Case 1 with Case 3), the flux does not change due to the boundary conditions; however the total pressure drop and flow field are changed. Similarly, there is no linear relationship between the total pressure drop and independent variables, such as density or viscosity.

When the entrance effect is not negligible, even in the same flow domain as the simulation above, permeability depends on fluid type and the status of flow. Variables, which appear in Darcy's law, are inter-dependent. There is no possibility that calculated permeability would change linearly, as one single variable changes and

others stay the same.

Further, if the flow domain is much larger than the zone influenced by the entrance effect, the pressure gradient is close to a constant value, i.e., pressure linearly decreases along the flow direction. Under this condition, permeability, which is proportional to the ratio of flux to pressure gradient, is considered to be a constant along flow direction for the same type of fluid. Thus, upscaling is applicable when the entrance effect zone is negligible compared with the total flow domain.

The values of flux and pressure drop could always be measured by experiment or numerical simulation. After that, permeability values could be calculated. The advantage of numerical simulation is it gives the details of velocity and pressure fields inside the flow domain. This helped us to evaluate the entrance effect directly.

3.4 Finite element method and flow simulation in the periodic domain

The finite element method (FEM) was first used by Courant (1943). At an early stage, this method was mostly used for analyzing structural mechanical problems. The principle and flowchart of the FEM are as follows:

- (1) Set up the geometry and divide domains into a number of discretized sub-domains. The shape of each sub-domain could be arbitrarily selected;
- (2) Each sub-domain is represented by a number of discrete points;

- (3) Derive the algebraic equations from the governing differential equation and make it valid at each discrete point; and
- (4) Input boundary and initial conditions, and solve the system of algebraic equations to obtain values of dependent variables at discrete points.

The advantages of the FEM include:

- (1) The shape of domains could be complicated; and
- (2) There are only small errors for diffusion-dominated problems (viscous flow), because the method has the characteristic of error minimization.

Compared to the finite difference method, the disadvantage of FEM is its computational cost.

We simulated the fluid flow in a periodic medium with the help of ANSYS version 15.0 using the FEM. The radii of wide and narrow throats for the periodic domain are 8mm and 4mm. Other parameters are the same as Case 1 of the rectangular domain simulation, such as density and viscosity of fluid, length of domain, and inlet and outlet velocities. This simulation is defined as Case A in the periodic flow domain. Figure 3-7 shows the corresponding results of velocity and pressure fields of final steady state flow in the periodic flow domain. The simulation parameters of Case A are shown in Table 2.

Density of fluid	1.5g/cm ³
Viscosity of fluid	3×10 ⁻⁵ Pa·s
Length of domain	0.08m
Wide and narrow radii	0.008m and 0.004m
Inlet velocity	0.01m/s
Outlet pressure	0 Pa

Table 2 Simulation parameters of Case 1 used in a periodic domain

Figure 3-7 shows the velocity and pressure fields when fluid flow reaches the steady state. The velocity field is shown at the top and pressure field is shown at the bottom. The color bar gives the magnitude of the corresponding field. The units of velocity fields and pressure field are m/s and Pa, respectively.

Due to the geometry of this type of flow domain, the flow field is difficult to be fully developed. Thus, the effective permeability had to be calculated case by case and could not be upscaled. The effective permeability was calculated using total pressure drop, flux, and viscosity. Compared with cases of rectangular domain simulation, the velocity field in a periodic domain is highly fluctuating. Wide throat zones store fluid as reservoirs. Thus, if proppant settle-down phenomena exist during hydraulic fracturing, it is disadvantageous to hydrocarbon production.

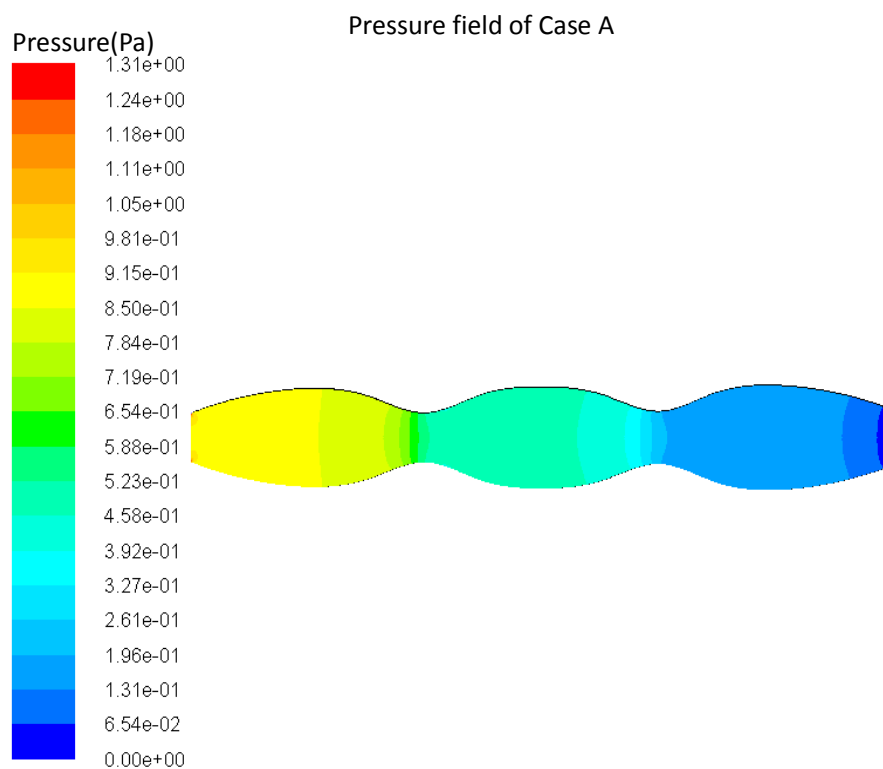
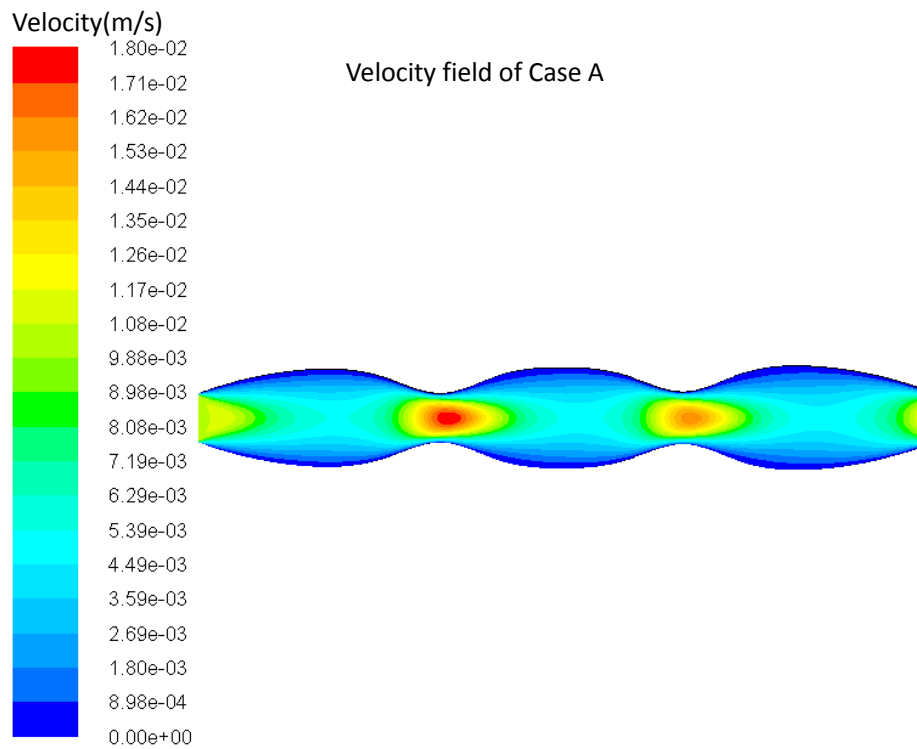


Figure 3-7 Simulation results of Case A in a periodic medium with 8mm and 4mm radii throats.

The only change in the Case B simulation compared with Case A in the periodic domain is that the wide and narrow radii become 0.004m and 0.002m. We kept boundary conditions and other parameters the same. The velocity field (top) and pressure field (bottom) are shown in Figure 3-8.

We found as the flow domain became narrower, the zone influenced by the entrance effect became more obvious. Compared with the result of Case A as shown in Figure 3-7, for example, the magnitude of the velocity field at the third narrow throat was closer to the second throat. Therefore, the flow field was difficult to fully develop. Thus, the ratio between flux and pressure gradient is not a constant. Permeability depends on medium (flow domain), type of fluid (density, viscosity), and in-situ conditions (applied pressure and/or flow velocity). Moreover, if the geometry of a flow domain is complicated, velocity and pressure inside the domain would be fluctuating, which could induce a turbulent effect. This is another reason for the difficulty of upscaling. Generally, favorable conditions for permeability upscaling include:

- (1) high viscosity fluid;
- (2) fluid flowing slowly or low applied pressure drop; and
- (3) simple geometry domain with fully developed flow field.

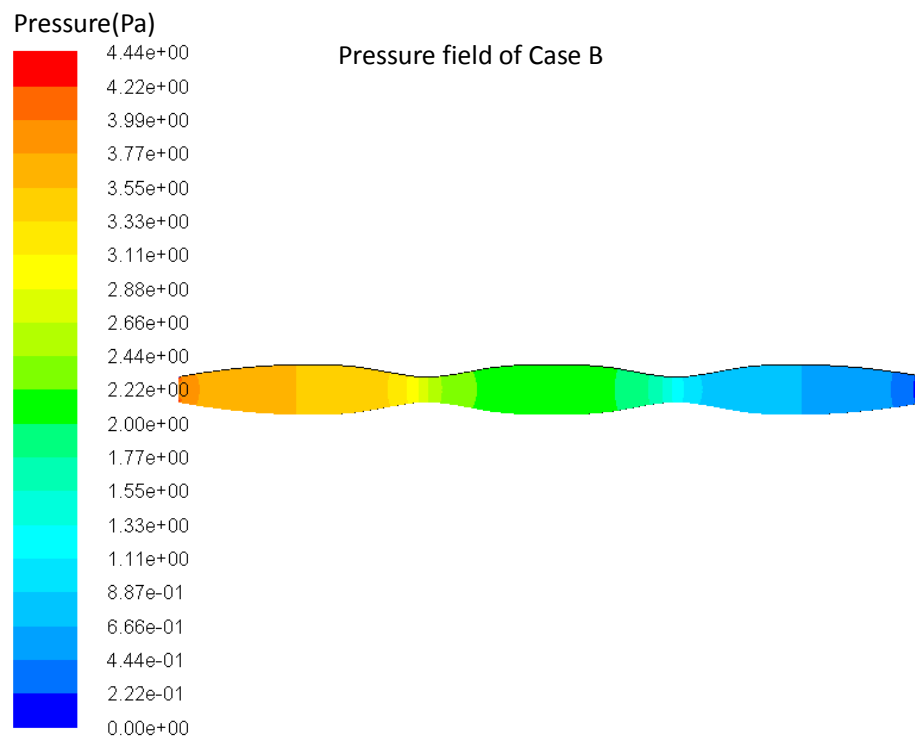
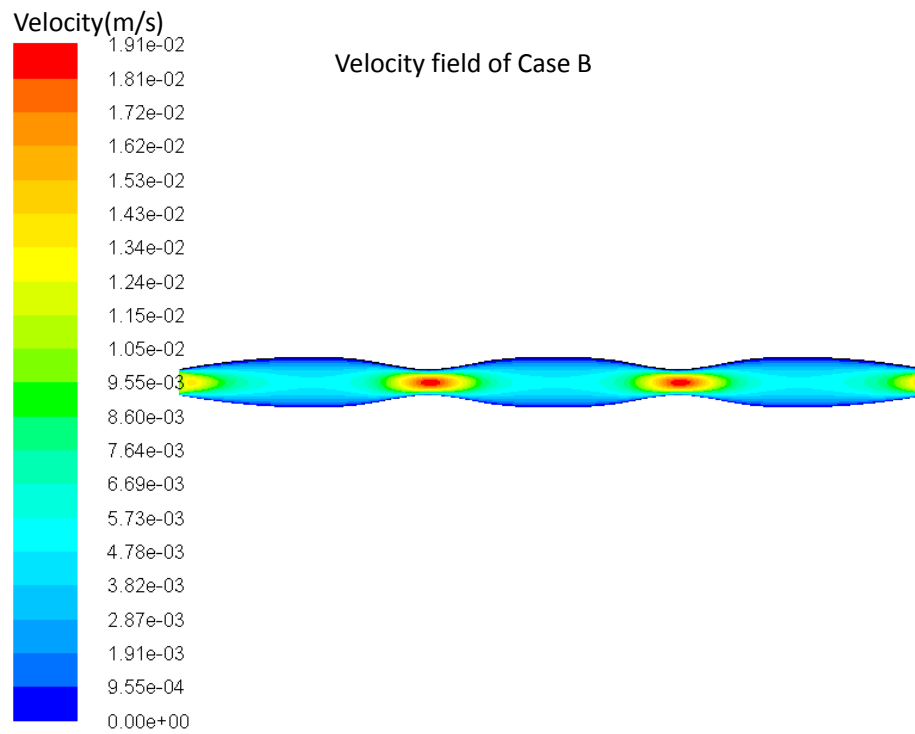


Figure 3-8 Simulation results of Case B in a periodic domain with 4mm and 2mm radii throats.

3.5 Fluid flow simulation in synthetic media

In this section, we simulate fluid flow in synthetic media. We first simulate fluid flow in a shale matrix. The reason for this test is that numerical methods could always give results; however, the simulated results need to be verified by analytical solutions or the results obtained by experiments. The permeabilities at 0 °, 45 °, and 90 ° to the bedding plane have been measured in our laboratory. Numerical simulation could provide the permeability along any angle to the bedding plane. Given no analytical solution, it is important to compare numerical solutions with experimental results, especially for the one with 45 ° to the bedding plane.

Also, we investigated the scale dependent effect. The model was composed of a fracture with a constant width parallel to the bedding plane inside a shale matrix.

3.5.1 Angular dependent permeability of shale sample

We used the same parameters according to laboratory measurements; for example, the radius and length of shale plugs used for measurement were 0.5 inch and 1 inch, respectively. Applied pressure drop on both ends was 300psi. The synthetic samples orient were 0 °, 15 °, 30 °, 45 °, 60 °, 75 °, and 90 ° to bedding plane, as shown in Figure 3-9.

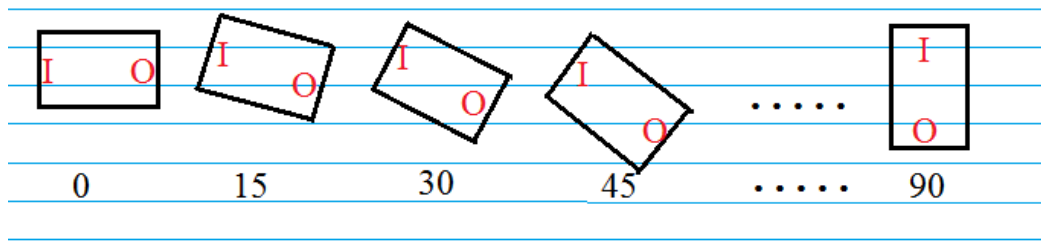


Figure 3-9 Blue lines represent the shale bedding planes. Shale plugs have different angles to the bedding planes. Letters “I” and “O” mean the inlet and outlet during measurements.

Boundary conditions were simulated to exactly match the laboratory measurement conditions as well. Table 3 gives the simulation parameters.

Length and radius of sample	1inch and 1inch
Fluid viscosity	$1.8 \times 10^{-5} \text{Pa}\cdot\text{s}$
Pressure drop	300psi

Table 3 Simulation parameters of fluid flow in a synthetic shale matrix.

In the real measurements, the sample was jacketed and no fluid was allowed to flow along or normal to the side of cylinder. Figure 3-10 gives a diagram the boundary conditions for the synthetic samples. The arrow represents the flow direction.

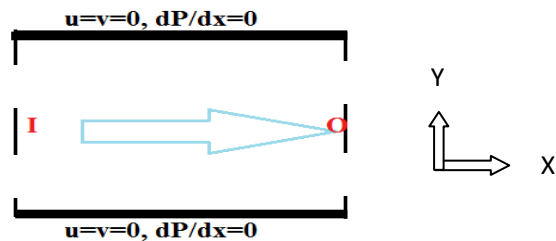


Figure 3-10 A synthetic shale sample diagram. Blue arrow represents the flow direction.

We set 1microDarcy and 1nanoDarcy as the permeabilities parallel and normal to the bedding plane according to the results obtained by measurement. We assume the samples are homogenous and no heterogeneities exist inside the sample. By simulating fluid flow, we were able to obtain the velocity field and pressure fields in the flow domain of each sample. Then angular dependent permeability was calculated. Plugs at 45 ° to the bedding plane were cut and measured in our laboratory. We compared the simulated results with experimental ones.

Results from the sample with 15 ° to the bedding plane velocity field and pressure field are shown in Figure 3-11.

Results from the sample with 30 ° to the bedding plane velocity field and pressure field are shown in Figure 3-12.

Results from the sample with 45 ° to the bedding plane velocity field and pressure field are shown in Figure 3-13.

Results from the sample with 60 ° to the bedding plane velocity field and pressure field are shown in Figure 3-14.

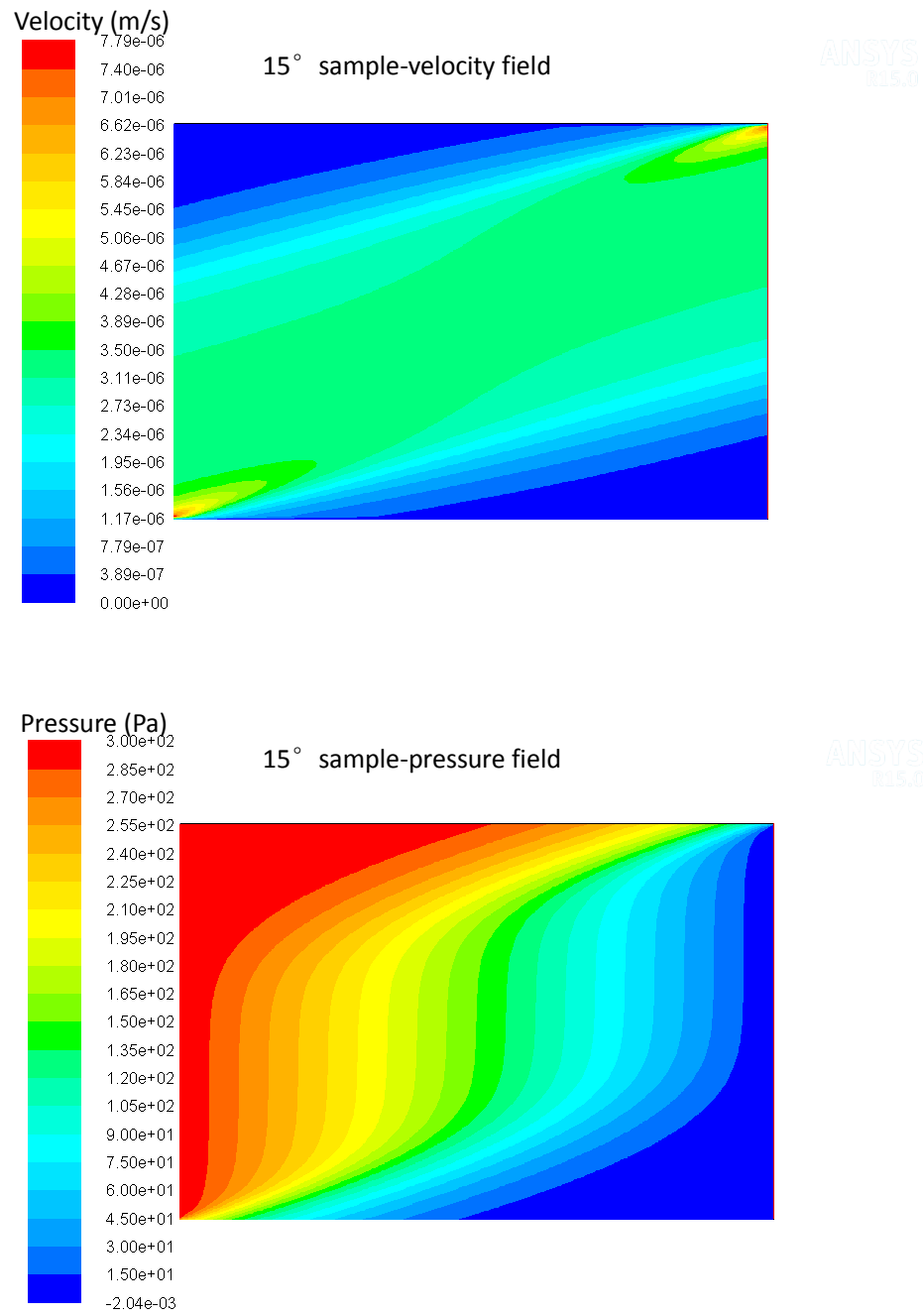


Figure 3-11 Velocity and pressure field of sample with 15 °to bedding plane

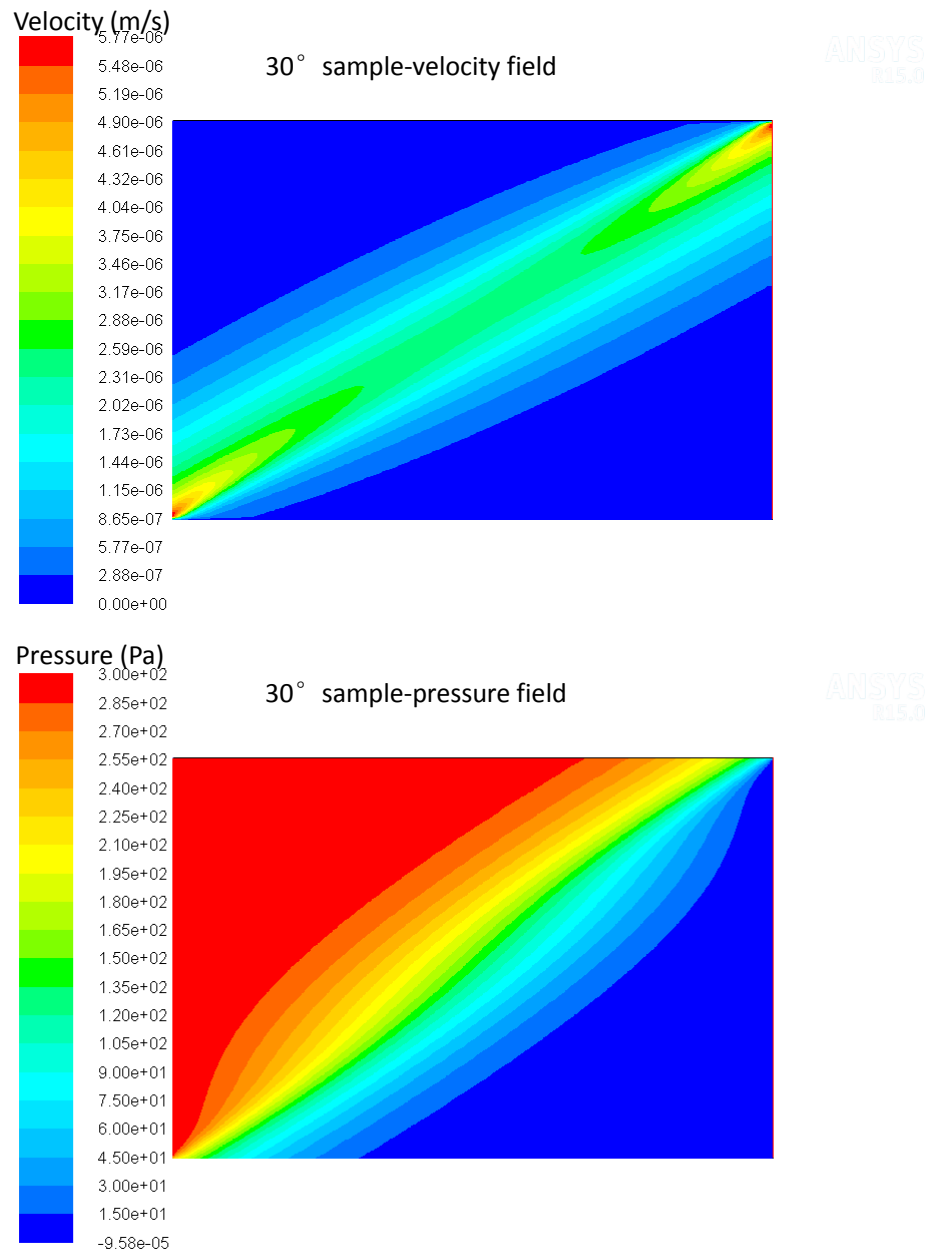


Figure 3-12 Velocity and pressure field of sample with 30 °to bedding plane

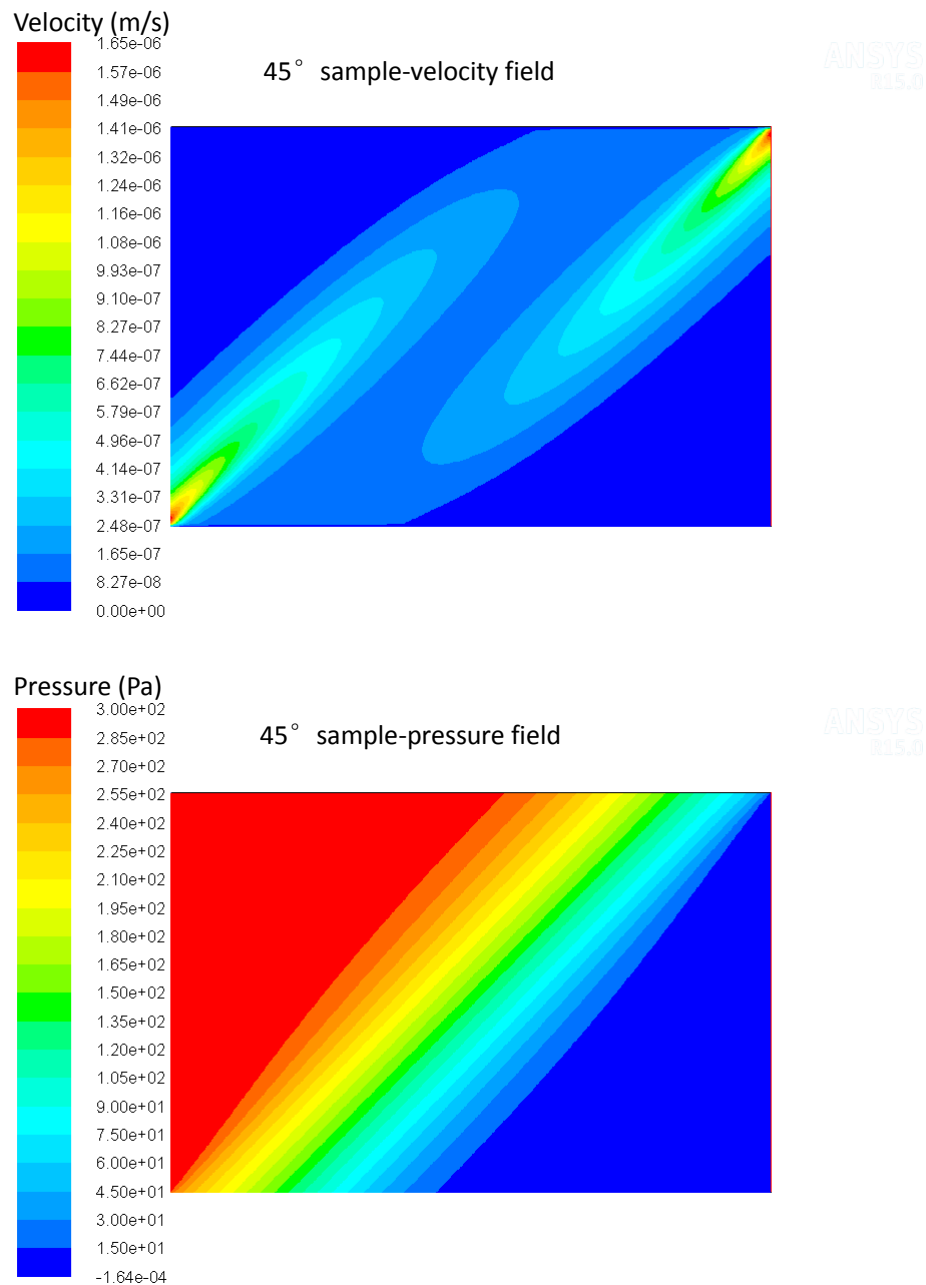


Figure 3-13 Velocity and pressure field of sample with 45 °to bedding plane

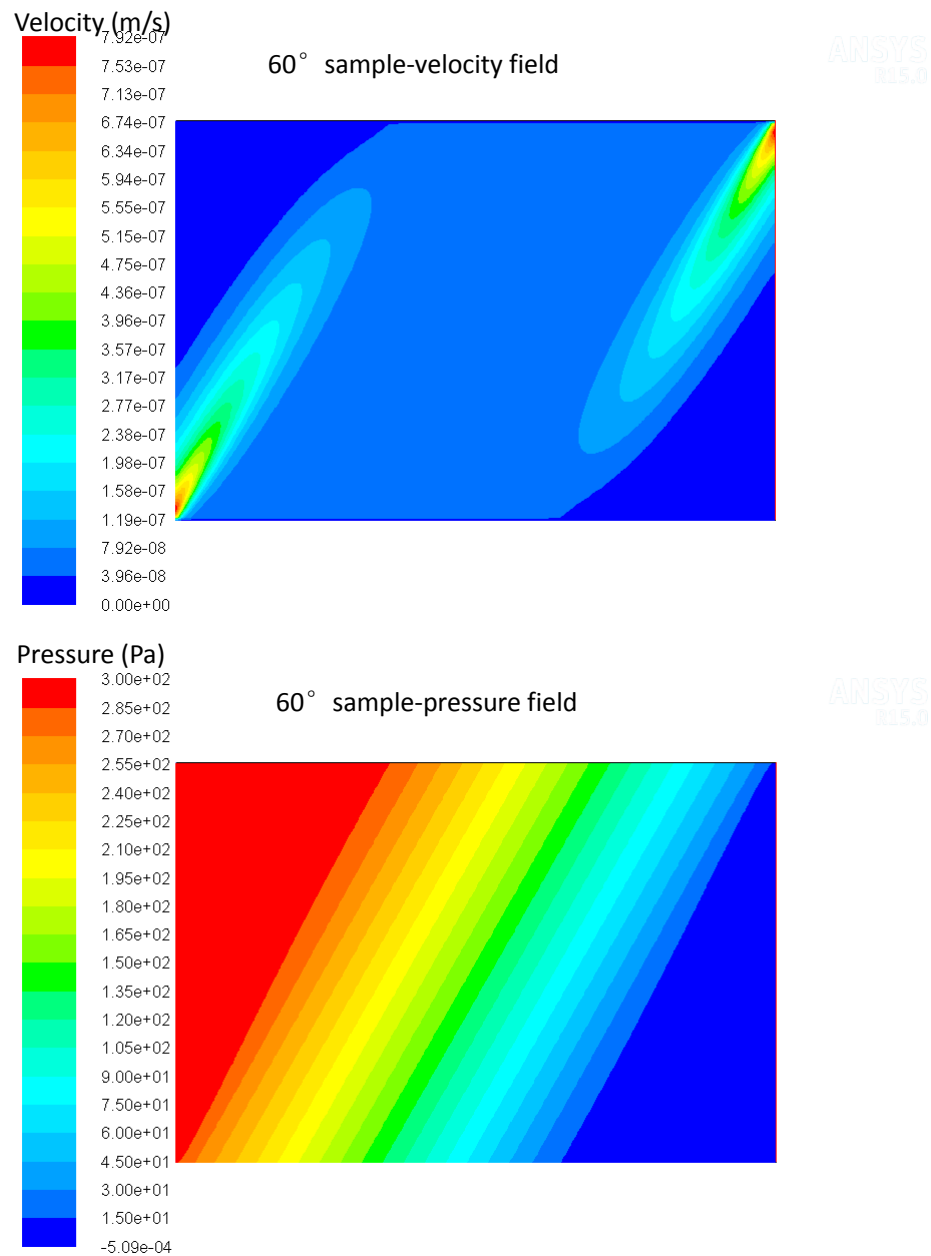


Figure 3-14 Velocity and pressure field of sample with 60 °to bedding plane

Using Darcy's law, we obtained angular-dependent permeability result for this synthetic shale core. The curve represents the permeability of samples with different angles to the bedding plane is shown in Figure 3-15. The simulated results are consistent with the ones obtained by laboratory measurement. This demonstrates the accuracy of the simulation algorithm we used.

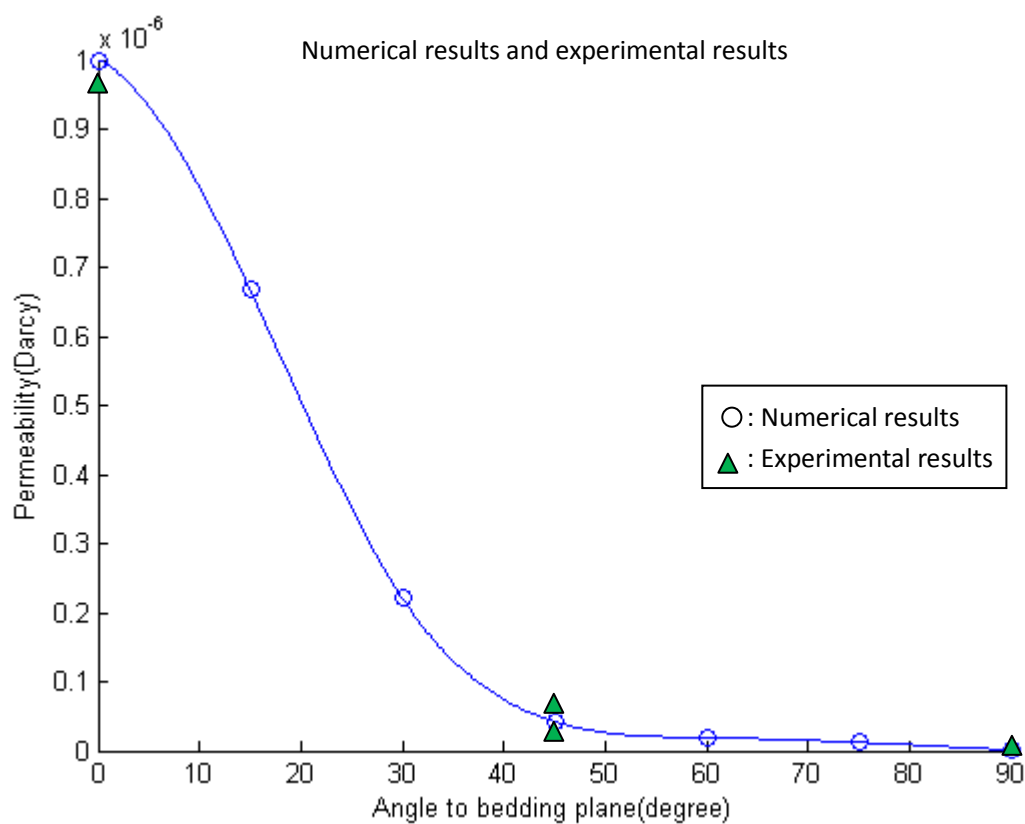


Figure 3-15 Angular dependent permeability of a lab-scale synthetic shale matrix sample

In this simulation, the ratio of radius to length is 1:1, and the pressure drop is 300psi. We observed the velocity field was not fully developed inside the flow

domain. Also, the pressure gradient did not close to a constant. Thus, this result could not be upscaled, even for another series' sample test which has the same ratio of radius to length but twice as big as the current sample size. The reason is the velocity at the boundaries of the cylinder was 0 for laminar flow. If we had tested another set of larger samples with the same ratio of radius to length, and same dP/dx for the whole sample, the surface effect would have been decreased and calculated permeability would have been increased. Because the size of samples was limited, permeability results obtained by laboratory measurement could not be upscaled generally, even for homogenous samples.

Besides, if the ratio of radius to length were changed in our case, the velocity field and pressure field would have been changed as well. Again, in many situations, permeability is a case-by-case problem.

3.5.2 Scale dependent effect

Though permeability is a case-by-case problem in general, we wanted to investigate under what conditions upscaling was possible, i.e., under what conditions flow field is fully developed and the entrance effect is negligible. When the flow field is fully developed, permeability would be linearly changed with flux or viscosity, and pressure gradient. The synthetic medium we used was a shale matrix containing a constant-width fracture. The only variable was the size of media. The sizes of sample

tested included 1cm*1cm, 2cm*2cm, 4cm*4cm, 8cm*8cm, and 16cm*16cm.

Other parameters are shown in Table 4 below.

Pressure drop	2 Pa
Width of fracture	1mm
Density of fluid	1.5g/cm ³
Permeability normal to the bedding plane	1nanoDarcy
Permeability along the bedding plane	1milliDarcy
Viscosity of fluid	3*10 ⁻⁴ Pa.s

Table 4 Simulation parameters for the scale dependent effect

The only variable here is the size of sample. Figure 3-16 gives a diagram of the model. The dashed lines represent the boundaries of different samples. The width of the fracture was kept the same.

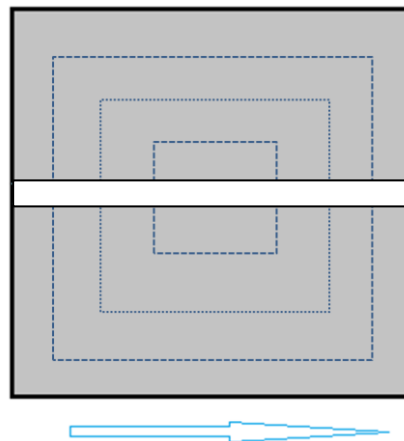


Figure 3-16 A diagram of different sizes of samples with a width-constant fracture inside.

Fluid was able to interchange between the rock matrix and fracture boundaries. Other boundary conditions kept the same boundary conditions as the ones in previous angular dependent simulations.

Pressure field and velocity field results obtained by the 1cm*1cm sample simulation are shown in Figure 3-17. According to the velocity field, we found the flow field was obviously not fully developed. The fracture domain influenced by the entrance effect was around 60%. The shale matrix contributed very little to the effective permeability of the sample.

Pressure field and velocity field results obtained by our 2cm*2cm sample simulation are shown in Figure 3-18. Compared with the whole domain, the zone under the entrance effect was much smaller.

Pressure field and velocity field results obtained by 4cm*4cm sample simulation are shown in Figure 3-19.

Pressure field and velocity field results obtained by 8cm*8cm sample simulation are shown in Figure 3-20.

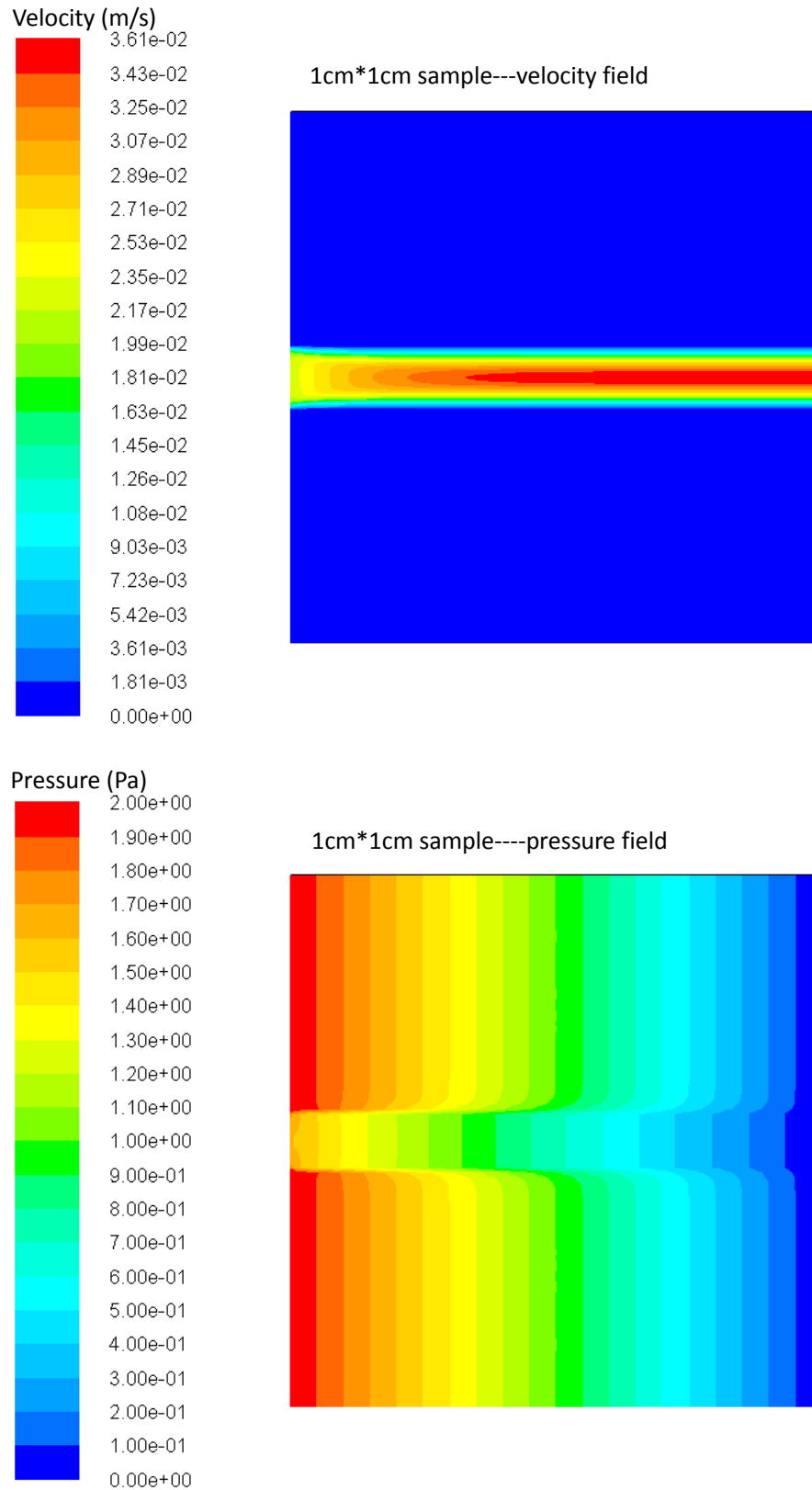


Figure 3-17 velocity field (top) and pressure field (bottom) of 1cm*1cm sample simulation

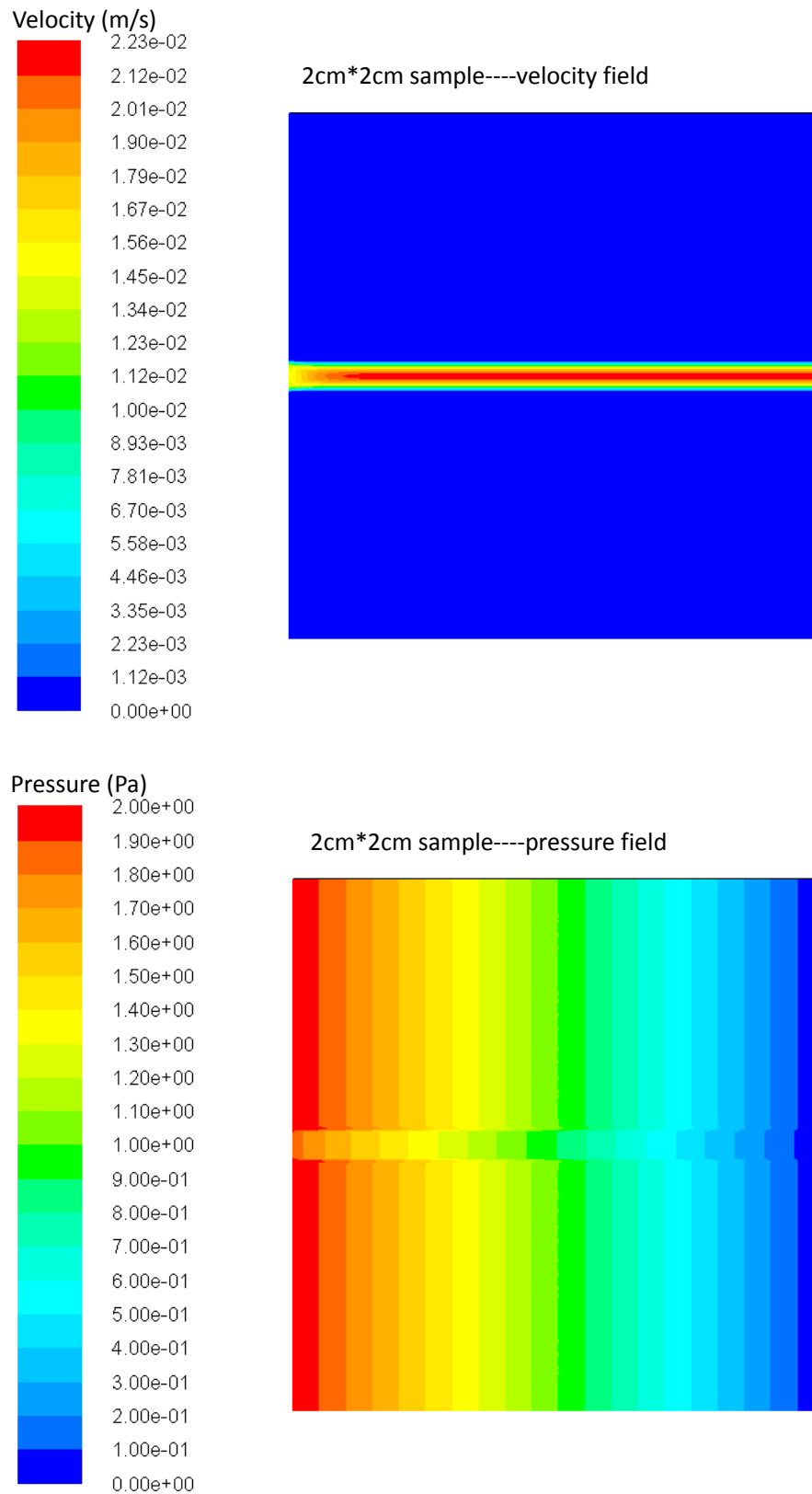


Figure 3-18 velocity field (top) and pressure field (bottom) of 2cm*2cm sample simulation

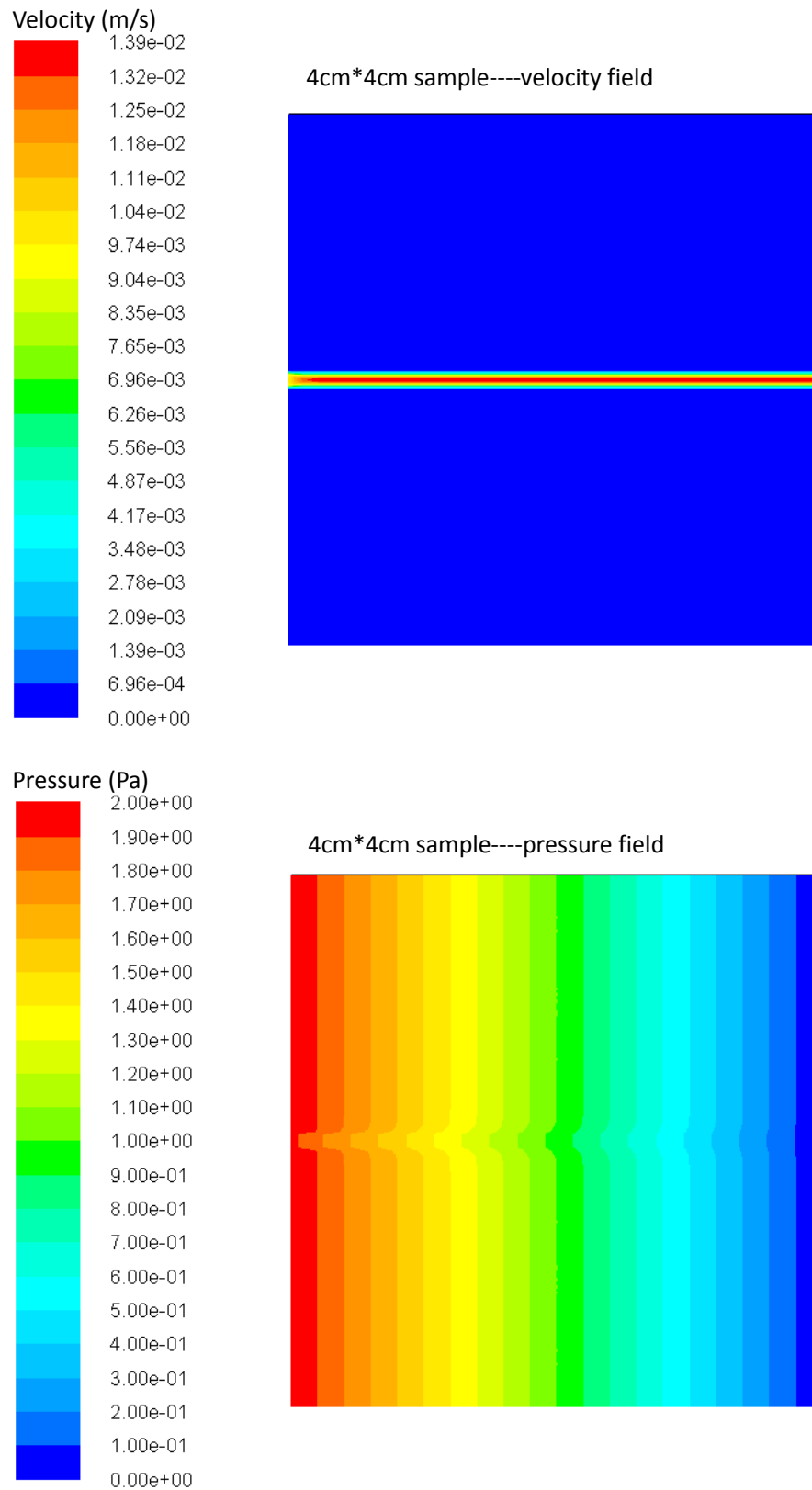


Figure 3-19 velocity field (top) and pressure field (bottom) of 4cm*4cm sample simulation

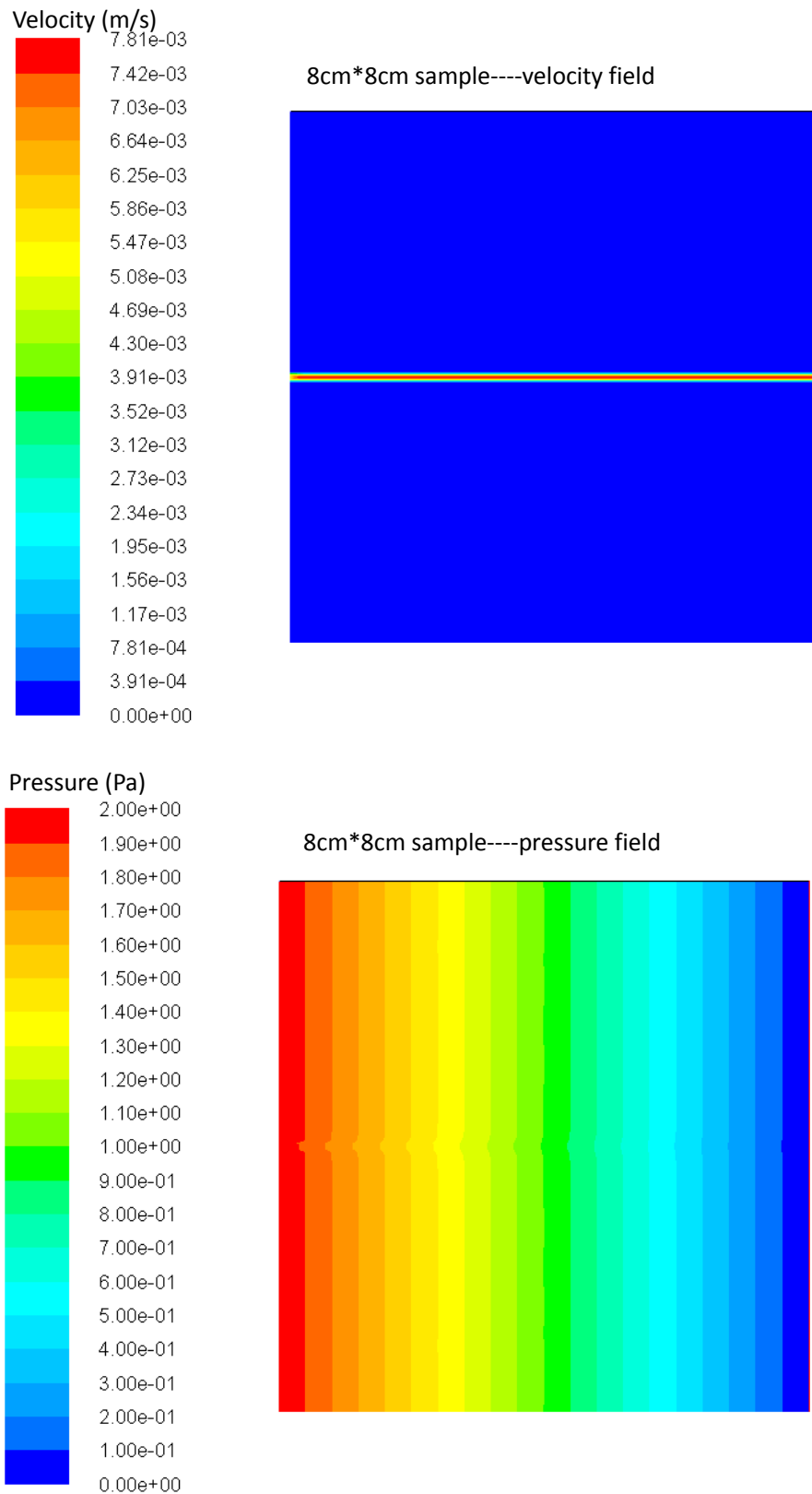


Figure 3-20 velocity field (top) and pressure field (bottom) of 8cm*8cm sample simulation

In this way, we obtain the permeability for different sizes of samples. The results are shown in Figure 3-21. Again, the permeability expression is $\kappa = \frac{Q}{A} \cdot \frac{\eta}{(\Delta P / \Delta x)}$, based on Darcy's law. In this set of simulations, we used the same width of fracture (1mm width) and the same pressure drop (2Pa) on both ends of each flow domain. In this simulation, the total pressure drop was only 2 Pa. Under these conditions, we found the zone under the entrance effect was around 60% for the 1cm*1cm domain, and 12% for the 2cm*2cm domain. The percentage was smaller and smaller as the size increased. When the size of the domain was larger than 2cm*2cm, as the size increased, the permeability decreased linearly. Again, this simulation result demonstrates that a simple flow domain and low pressure drop are favorable conditions for upscaling.

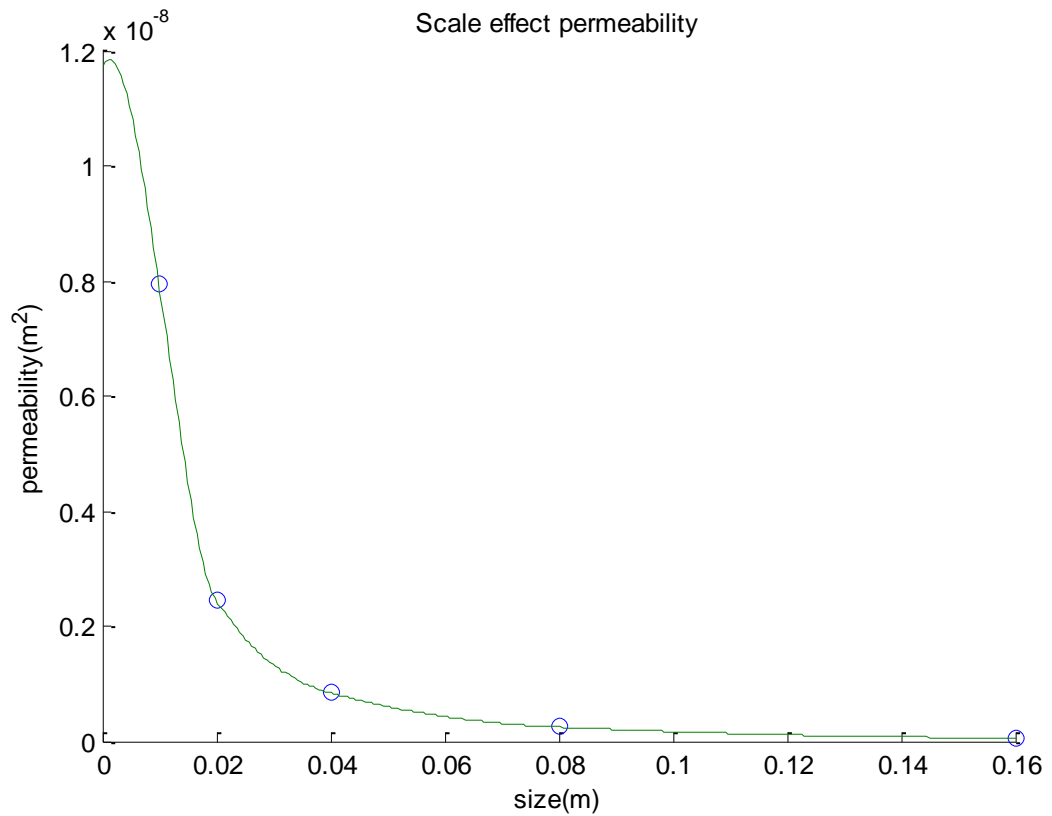


Figure 3-21 Calculated permeability results of samples with different sizes

3.6 Conclusion and discussion

Numerical simulation provides another way to obtain permeability.

Simulation results of fluid flow in synthetic media demonstrate:

- (1) If the flow domain is not much larger than the zone influenced by the entrance effect, the variables in Darcy's law are inter-dependent. If so, the obtained permeability, by experiment or simulation, could not be upscaled, even under homogenous conditions.

- (2) The size influenced by the entrance effect inside the flow domain simultaneously depends on: the geometry of the flow domain; fluid properties, such as viscosity and density; and in-situ parameters, such as applied pressure drop or inlet velocity. Generally, the entrance effect would be weak if a high viscosity fluid were slowly flowing through a simple geometry domain. If the entrance effect is negligible, upscaling could be applicable. If not, permeability is a case-by-case problem. Though permeability values could be obtained by experiment or numerical methods, compared with lab measurement, numerical methods provide a way to illustrate the velocity and pressure fields more directly, which is important for evaluating the entrance effect and considering upscaling.
- (3) The velocity field fluctuates when there is fluid flow in a periodic domain. The flow field is difficult to fully develop. The wide throat zones store fluid as reservoirs.
- (4) If upscaling is applicable under certain cases, we still need to make sure it is in a laminar flow regime by checking the Reynolds number.

The fluid we used for derivations and simulations is an incompressible fluid. If a compressible fluid were involved, the situations would be much more complicated. In this chapter, we have investigated the permeability problem

completely from a transport property perspective, without considering elastic effects. For example, if we set pressure values as boundary conditions at both ends of the flow domain, we only focused on the absolute pressure drop. In other words, if we used 300psi and 0psi at both ends as boundary conditions for one case, and used 400psi and 100psi at both ends for another case, their simulation results are the same. But real situations would be different from this.

Chapter 4 Conclusions and future work

4.1 Conclusions

The diffusivity tensor is found to be equal to the permeability tensor divided by a scalar which is the product of dynamic viscosity, connected formation porosity, and formation compressibility.

Applying the diffusion method to the microseismic data acquired in the Barnett Shale Formation, we obtained an initial permeability of 0.16 and 3.21 milliDarcy parallel and perpendicular to the assumed dominant direction of fracturing, with an increase to 12.1 milliDarcy in the dominant fracturing direction after hydraulic fracturing.

Numerical methods, as an alternative, could help us to simulate fluid flow in different types of domains and calculate the permeability. Compared with experimental results, numerical simulations could provide us not only the permeability results, but also the velocity and pressure fields inside the flow domains. With the help of numerical simulation results, we could analyze the upscaling problems. Generally, a high viscosity fluid slowly flows in a simple geometry domain is the favorable condition for upscaling. Besides, numerical simulations could provide the angular and scale dependent permeability results. Thus, there is still a lot of potential of numerical simulations to develop in reservoir modeling, upscaling topics.

4.2 Recommendation for future work

Microseismic event location is the first step of microseismic monitoring. It is the basis for analyzing diffusion procedures and building fracture networks. Whether using a picking-based or migration-based method, a velocity model is the key for the accuracy of microseismic event location. The structure of the subsurface medium is changing during the pumping stage and the velocity model should be updated during pumping. Thus, dynamic velocity modeling is an important research field in the future.

Hydraulic fracturing induces thousands of microseismic events. For the picking-based method, automatic and accurate arrival-picking are necessary, especially for weak signals. This is another research field in the future. The general relation between magnitude and the number of locatable events is shown in Figure 4-1.

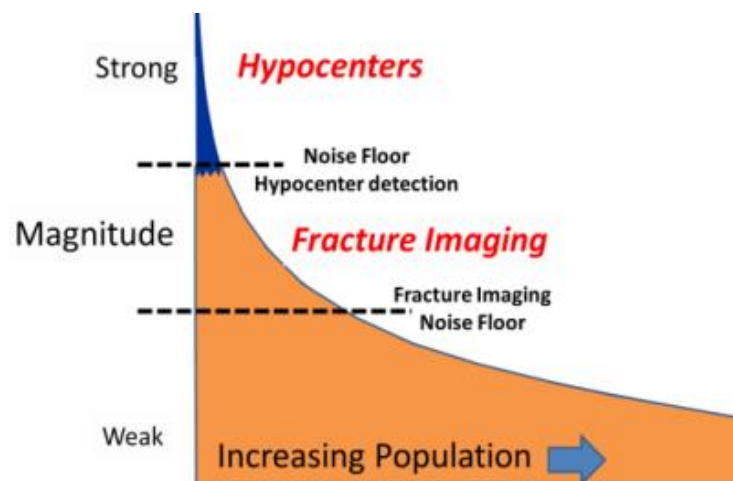


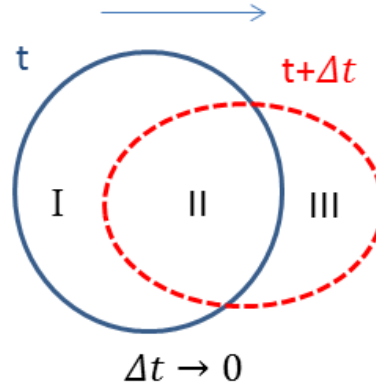
Figure 4-1 The relation between the magnitude and the number of locatable microseismic events.

If we could reduce the locatable threshold, such as picking from a noisy environment, the number of locatable microseismic events would increase a lot, which would much better improve diffusion characterization.

Moment tensor inversion tells us the mechanism of failure and orientation of a fracture. This could help us differentiate the events induced by fracture opening or diffusion. Microseismic event location results, moment tensor solutions, and magnitude analysis of each event would help us build fracture networks. Then, we could simulate fluid flow inside and estimate the time-lapse permeability result.

Appendix

For Lagrangian description, we focus on a system, which means the collection of particles of fixed mass or other identities. Here we show the derivation of the Reynold Transport Theorem which transforms Lagrangian description to Eulerian description (modified from [Munson, Young and Okiishi, 1990]).



Solid blue and red dashed circles show the same system at different times. The moving direction is from left to right, as shown on the top of the figure. The blue solid circle and red dashed circle represent the system at time t and $t + \Delta t$. At time t , the system contains Regions I and II. At time $t + \Delta t$, the system contains Regions II and III. Region II is included by the system at a different time and is a defined control volume. If we assume Δt is infinitely small, then Region II approximately equals the system.

Here we use N to represent any extensive property. So it could represent mass, momentum or energy. We use N_t and $N_{t+\Delta t}$ to represent the property of this

system at times t and $t + \Delta t$, respectively. Obviously,

$$N_t = (N_I)_t + (N_{II})_t \quad \text{and} \quad N_{t+\Delta t} = (N_{II})_{t+\Delta t} + (N_{III})_{t+\Delta t}.$$

Because Δt is infinite small, the derivative of the system is:

$$\left. \frac{dN}{dt} \right|_{\text{sys}} = \lim_{\Delta t \rightarrow 0} \frac{N_{t+\Delta t} - N_t}{\Delta t} = \frac{(N_{II})_{t+\Delta t} - (N_{II})_t}{\Delta t} + \int_{\text{c.s.}} \vec{N} \cdot d\vec{S},$$

where c.s. represents the control surface.

Thus, the general form of Reynolds Transport Theorem is:

$$\left. \frac{dN}{dt} \right|_{\text{sys}} = \left. \frac{\partial N}{\partial t} \right|_{\text{CV}} + \int_{\text{c.s.}} \rho n (\vec{V}_r \cdot \vec{\eta}) dA,$$

where \vec{V}_r is the velocity of fluid relative to the control volume, $\vec{\eta}$ is the unit normal vector of the control surface, and n equals the property per unit mass.

N could represent any extensive property, such as mass and momentum.

Here we give the mass and momentum conservation equation. The table below shows the meanings of N and n in each case.

	Mass conservation	Momentum conservation
N	$m(\text{mass})$	$m\vec{v}$
n	1	\vec{v}
General expression	$\left. \frac{dm}{dt} \right _{\text{sys}} = \left. \frac{\partial m}{\partial t} \right _{\text{cv}} + \int_{\text{cs}} \rho (\vec{v}_r \cdot \vec{\eta}) dA$	$\left. \frac{d(m\vec{v})}{dt} \right _{\text{sys}} = \left. \frac{\partial}{\partial t} \int \rho \vec{v} dV \right _{\text{cv}} + \int_{\text{cs}} (\rho \vec{v})(\vec{v}_r \cdot \vec{\eta}) dA$
Special case	$\frac{\partial \rho}{\partial t} + \nabla \cdot (\rho \vec{v}) = 0$	$\sum F_{\text{cv}} = \int_{\text{cv}} \frac{\partial}{\partial t} (\rho \vec{v}) dV + \int_{\text{cs}} (\rho \vec{v})(\vec{v} \cdot \vec{\eta}) dA$

Table A-1 Mass and momentum conservation expressions based on Reynolds Transport Theorem.

In the table, ‘special case’ is based on two assumptions. The first one is that the control volume is underformable, i.e., the control volume is not a function of time.

So,

$$\frac{\partial}{\partial t} \int_{cv} \rho dV = \int_{cv} \frac{\partial}{\partial t} \rho dV .$$

The second assumption is the flow is stationary, i.e., the velocity relative to the control volume equals the absolute velocity.

References

- Abaseyev, S. S., Ammerman, M., and Chesnokov, E. M., 2009, Automated detection and location of hydrofracking-induced microseismic event from 3C observations in an offsetting monitor well, 79th Annual International Meeting, SEG Expanded Abstracts, 1514-1518.
- Abercrombie, R. E., 1995, Earthquake source scaling relationships from – 1 to 5 ML using seismograms recorded at 2.5-km depth. *Journal of Geophysical Research: Solid Earth* (1978–2012), 100(B12), 24015-24036.
- Aki, K., and Richards, P. G., 2002, *Quantitative Seismology* (Vol. 1), University Science Books, Sausalito, CA.
- Baig, A., and Urbancic, T., 2010, Microseismic moment tensors: A path to understanding frac growth. *The Leading Edge*, 29(3), 320-324.
- Baysal, E., Kosloff, D. D., and Sherwood, J. W., 1983, Reverse time migration. *Geophysics*, 48(11), 1514-1524.
- Brune, J. N., 1970, Tectonic stress and the spectra of seismic shear waves from earthquakes. *Journal of Geophysical Research*, 75(26), 4997-5009.
- Brune, J. N., 1979, Implications of earthquake triggering and rupture propagation for earthquake prediction based on premonitory phenomena. *Journal of Geophysical Research: Solid Earth* (1978–2012), 84(B5), 2195-2198.
- Carman, P.C., 1961, L'écoulement des Gaz à Travers les Milieux Poreux, Bibliothèque des Sciences et Techniques Nucléaires, Presses Universitaires de France, Paris.
- Chesnokov, E. “Microseismics: Integrated, Advanced Geophysics” Class lecture, Microseismic, Natural Sciences and Mathematics, Houston, TX, August 27, 2012.
- Chesnokov, E., Bayuk, I. O., and Ammerman, M., 2010, Determination of shale stiffness tensor from standard logs. *Geophysical Prospecting*, 58(6), 1063-1082.
- Courant, R. (1943). Variational methods for the solution of problems of equilibrium and vibrations. *Bull. Amer. Math. Soc*, 49(1), 1-23.
- Darcy, H., 1856, Les Fontaines Publiques de la Ville de Dijon, Dalmont, Paris.

Earle, P. S., and Shearer, P. M., 1994, Characterization of global seismograms using an automatic-picking algorithm. *Bulletin of the Seismological Society of America*, 84(2), 366-376.

Eaton, D.W., 2009, Resolution of microseismic moment tensors: A synthetic modeling study: 79th Annual International Meeting, SEG Expanded Abstracts, 28,3569-3573.

Ernstoff, A. S., and Ellis, B. R., 2013, Clearing the waters of the fracking debate. *Michigan Journal of Sustainability*, 1, 109-129.

Gajewski, D., and Tessmer, E., 2005, Reverse modelling for seismic event characterization. *Geophysical Journal International*, 163(1), 276-284.

Grechka, V., Mazumdar, P., and Shapiro, S. A., 2010, Predicting permeability and gas production of hydraulically fractured tight sands from microseismic data. *Geophysics*, 75(1), B1-B10.

Gregory, K. B., Vidic, R. D., and Dzombak, D. A., 2011, Water management challenges associated with the production of shale gas by hydraulic fracturing. *Elements*, 7(3), 181-186.

Hu, S. Z., and Ni, G. J., 1989, Mathematical Methods for Physicist, Higher Education Press, Beijing, 195-197.

Jost, M. U., and Herrmann, R. B., 1989, A student's guide to and review of moment tensors. *Seismological Research Letters*, 60(2), 37-57.

Lambordi, M. E., 2014, Convex hull method for SRV estimation, Master's thesis, University of Houston.

Lay, T., and Wallace, T. C., 1995, *Modern Global Seismology* (Vol. 58). Academic press, Tucson, Arizona, 347-351.

Liao, Q., Kouri, D., Nanda, D., and Castagna, J., 2011, Automatic first break detection by spectral decomposition using minimum uncertainty wavelets, *SEG Expanded Abstracts*, 1627-1631.

Loux, T. A., and Filshill, A., 2013, Geosynthetic lining systems for shale gas drilling activities. usage, regulations, concerns, and challenges. *Geosynthetics*, 31(5), 34-41.

Metwally, Y., and Chesnokov, E. M., 2010, Measuring gas shale permeability tensor in the lab scale. *SEG Denver 2010 Annual Meeting* (2628-2633).

Montgomery, S. L., Jarvie, D. M., Bowker, K. A., and Pollastro, R. M., 2005, Mississippian Barnett Shale, Fort Worth basin, north-central Texas: Gas-shale play with multi-trillion cubic foot potential. *AAPG Bulletin*, 89(2), 155-175.

Munson, B. R., Young, D. F., and Okiishi, T. H., 1990, Fundamentals of Fluid Mechanics. John Wiley and Sons, New York.

National Research Council, 2012, *Induced Seismicity Potential in Energy Technologies*, The National Academies Press, Washington, DC.

Osakwe, E.O., 2013, Estimation of the source mechanisms of microseismic events from a Barnett shale play, Master's thesis, University of Houston.

Richardson, L. F., 1911, The approximate arithmetical solution by finite differences of physical problems involving differential equations, with an application to the stresses in a masonry dam. *Philosophical Transactions of the Royal Society of London. Series A, Containing Papers of a Mathematical or Physical Character*, Vol.210, 307-357.

Schaff, D. P., Bokelmann, G. H., Ellsworth, W. L., Zankerka, E., Waldhauser, F., and Beroza, G. C., 2004, Optimizing correlation techniques for improved earthquake location. *Bulletin of the Seismological Society of America*, 94(2), 705-721.

Schaff, D. P., and Waldhauser, F., 2005, Waveform cross-correlation-based differential travel-time measurements at the Northern California Seismic Network. *Bulletin of the Seismological Society of America*, 95(6), 2446-2461.

Schaff, D. P., 2008, Semiempirical statistics of correlation-detector performance. *Bulletin of the Seismological Society of America*, 98(3), 1495-1507.

Shapiro, S. A., Huenges, E., and Borm, G., 1997, Estimating the crust permeability from fluid-injection-induced seismic emission at the KTB site. *Geophysical Journal International*, 131(2), F15-F18.

Shapiro, S. A., Audigane, P., and Royer, J. J., 1999, Large-scale in situ permeability tensor of rocks from induced microseismicity. *Geophysical Journal International*, 137(1), 207-213.

Stein, S., and Wysession, M., 2009, *An Introduction to Seismology, Earthquakes, and Earth Structure*. John Wiley and Sons, New York.

Song, F., and Toksöz, M. N., 2011, Full-waveform based complete moment tensor inversion and source parameter estimation from downhole microseismic data for hydrofracture monitoring. *Geophysics*, 76(6), WC103-WC116.

Talwani, P., and Acree, S., 1984, Pore pressure diffusion and the mechanism of reservoir-induced seismicity. *Pure and Applied Geophysics*, 122(6), 947-965.

Ursell, T. S., 2007, The diffusion equation: A multi-dimensional tutorial, California Institute of Technology, Pasadena, *Tech.Rep.*

Vavryčuk, V., 2007, Ray velocity and ray attenuation in homogeneous anisotropic viscoelastic media. *Geophysics*, 72(6), D119-D127.

Vidale, J. E., 1986, Complex polarization analysis of particle motion. *Bulletin of the Seismological Society of America*, 76(5), 1393-1405.

Williams, C. L., Bodmann, B. G., and Kouri, D. J., 2014, Fourier and beyond: Invariance properties of a family of integral transforms. *arXiv preprint arXiv:1403.4168*.

